Title

On the response of polar cap dynamics to its solar wind and magnetotail drivers at high levels of geomagnetic activity

Author
Gao, Ye

Publication Date
2012

Peer reviewed|Thesis/dissertation

UNIVERSITY OF CALIFORNIA

Los Angeles

On the Response of Polar Cap Dynamics to Its Solar Wind and Magnetotail Drivers at High Levels of Geomagnetic Activity

A dissertation submitted in partial satisfaction

of the requirements of the degree

Doctor of Philosophy in Geophysics and Space Physics

by

Ye Gao

2012

Abstract of the Dissertation

On the Response of Polar Cap Dynamics to Its Solar Wind and Magnetotail Drivers at High Levels of Geomagnetic Activity

by

Ye Gao

Doctor of Philosophy in Geophysics and Space Physics

University of California, Los Angeles, 2012

Professor Raymond J. Walker, Chair

In this thesis, I investigate how polar cap dynamics, quantified by the northern polar cap (PCN) index, respond to solar wind direct driving and magnetotail energy unloading during intervals of strong solar wind driving. Using 53 one to two-day intervals with high cross polar cap potential subintervals, I find that, among 11 candidate coupling functions including the electric field of *Kan and Lee* (1979) and the universal coupling function of *Newell et al*. (2007), the PCN index correlates most closely with the electric field ($E_{\text{K-R}}$) of *Kivelson and Ridley* (2008), a form in which the electric field imposed on the ionosphere by low-latitude magnetopause reconnection saturates at high levels of geomagnetic activity. It is found that magnetotail activity, as represented by an unloading AL index (AL_U), makes a significant contribution to the PCN index. A linear model is constructed to relate the PCN index to its solar wind and magnetotail drivers. Based on this model, it is estimated that the portion of the PCN index directly driven by the solar wind electric field outweighs the contribution arising from energy release in the magnetotail by roughly a factor of 2. The solar wind dynamic pressure (p_{dyn}) does not play a key role in

controlling the PCN index. However, under intense solar wind driving, the number density (*n*) can influence the solar wind-magnetosphere coupling by changing the solar wind Alfvén conductance, which is incorporated in $E_{\text{K-R}}$. The validity of the linear model is verified by comparing its results with those obtained from a more general, non-linear model, termed additive model. It is found that, except in anomalous events during which the auroral oval expanded poleward to the latitude of the PCN index station and the index increased because of proximity to auroral zone currents, the linear model is a good approximation, since more than 70% of the variation in the PCN index is explained by the linear model. Thus, this linear model provides a useful tool to study the coupling between the solar wind, magnetosphere and ionosphere.

This model is applied day-by-day from 1 February 1998 to 31 December 2009 to investigate the driven and unloading contributions to the PCN index. I find that the relative contributions of driven and unloading components varies with solar cycle with a magnitude ±5%, with the driven-to-unloading ratio highest near solar minimum and lowest slightly after solar maximum, and the driven-to-unloading ratio peaks in summer and decreases in winter with a magnitude as large as ±15%.

Although the theory of *Kivelson and Ridley* (2008) is successful in predicting the polar cap dynamics from the solar wind input, there is a competing theory of *Siscoe et al.* (2002). The similarity and difference between these two theories are explored. It is found that, except for some trivial differences, the predictions of the two theories are practically the same in the saturation limit. In addition, the model predictions are compared to the measurements of AMIE, DMSP, the PC index, and SuperDARN. Given the great differences from different measurements, it is impossible to show that one theory outperforms the other.

The dissertation of Ye Gao is approved.

Margaret G. Kivelson

Robert L. McPherron

Qing Zhou

Raymond J. Walker, Committee Chair

University of California, Los Angeles

2012

Dedicated to my beloved parents …

Table of Contents

List of Figures

Acknowledgements

I am indebted to Professor Raymond J. Walker and Professor Margaret G. Kivelson for their supervision in this research. I am grateful to Professor Aaron J. Ridley, Professor Robert L. McPherron, Dr. Krishan K. Khurana and Dr. Tung-Shin Hsu for their help in data analysis. I would like to thank Professor Aaron J. Ridley for his technical support in obtaining the AMIE data, Dr. James M. Weygand for propagating the ACE data from Lagrange point 1 to bow shock, Dr. Harold U. Frey for generating aurora plots from IMAGE data, Dr. Oleg A. Troshichev for providing the polar cap index data, Dr. Marc R. Hairston for providing the DMSP data and Nathaniel A. Frissell for providing the SuperDARN data.

VITA

2007 – 2012	Graduate Student Researcher Department of Earth and Space Sciences, UCLA
2011	Master of Science in Statistics Department of Statistics, UCLA
2011	Master of Science in Geophysics and Space Physics Department of Earth and Space Sciences, UCLA
2011	Eugene B. Waggoner Scholarship Department of Earth and Space Sciences, UCLA
2007	Joan Palevsky Scholarship UCLA
2003 – 2007	Bachelor of Science in Geophysics and Space Physics University of Science and Technology of China

PUBLICATIONS

Gao, Y. (2012), Comparing the cross polar cap potentials measured by SuperDARN and AMIE during saturation intervals", *J. Geophys. Res.*, *J. Geophys. Res.*, *117*(A8), A08325, doi:10.1029/2012ja017690.

Gao, Y., M. G. Kivelson, A. J. Ridley, J. M. Weygand, and R. J. Walker (2012), Utilizing the polar cap index to explore strong driving of polar cap dynamics, *J. Geophys. Res.*, *117*(A7), A07213, doi:10.1029/2011ja017087.

Gao, Y. (2012), On anomalous departures from a linear relation between the polar cap index and its controlling factors in solar wind and magnetotail, *J. Geophys. Res.*, *117*(A6), A06201, doi:10.1029/2012ja017721.

Gao, Y., M. G. Kivelson, and R. J. Walker (2012), The linear dependence of polar cap index on its controlling factors in solar wind and magnetotail, *J. Geophys. Res.*, *117*(A5), A05213, doi:10.1029/2011ja017229.

Gao, Y., M. G. Kivelson, R. J. Walker, and J. M. Weygand (2012), Long-term variation of driven and unloading effects on polar cap dynamics, *J. Geophys. Res.*, *117*(A2), A02203, doi:10.1029/2011ja017149.

CHAPTER 1

Solar-Terrestrial Physics: An Introduction

Solar-terrestrial physics is principally concerned with the interaction of ionized particles with the electric and magnetic fields in the space environment. The ionized gases, called plasma, interact in complex ways, in which the electric and magnetic fields control the motion of the particles, with collisions and gravitational fields being less important [*Russell*, 1995]. It is often convenient to collectively treat the particles as a fluid, i.e. the magnetohydrodynamic (MHD) approximation [e.g. *Kivelson*, 1995]. In this thesis, I follow this approximation and investigate the interaction between the solar wind and earth's magnetic field at high levels of geomagnetic activity. Before proceeding to detailed analysis, relevant concepts in solar-terrestrial physics are introduced in this chapter.

1.1 Solar wind and measurements

The solar wind, a flow of ionized hydrogen with a small portion of ionized helium and magnetic field from the sun, results from the huge pressure difference between the solar corona and interplanetary space [*Hundhausen*, 1995]. It plays a key role in controlling disturbances in the earth's magnetic field, i.e., geomagnetic activity [e.g. *Clauer et al.*, 1981; *McPherron et al.*, 1988; *Horton et al.*, 1999]. By terrestrial standards, the solar wind is hot, tenuous, and fast-moving.

Embedded in this plasma is a weak magnetic field, i.e. interplanetary magnetic field (IMF), primarily oriented in a direction nearly parallel to the ecliptic plane, at approximately 45^o to the earth-sun line at 1 astronomical unit (AU) [*Hundhausen*, 1995].

Nowadays, measurements of solar wind are primarily made by spacecrafts, e.g. the Advanced Composition Explorer (ACE) spacecraft, orbiting the Lagrange point 1 (L1) which is a point of earth-sun gravitational equilibrium about 1.5 million kilometers from earth and 148.5 million kilometers from the Sun [*Mazur et al.*, 2000; *Emslie et al.*, 2004; *Gosling et al.*, 2005; *King and Papitashvili*, 2005]. ACE was launched on 25 August 1997 [*Stone et al.*, 1998]. From its location at L1, ACE has a prime view of the solar wind, and thus, provides near-real-time continuous observation of solar wind parameters and the IMF. The magnetic field vectors provided by the Magnetic Fields (MAG) instrument [*Smith et al.*, 1998] and plasma moments obtained from the Solar Wind Electron, Proton, and Alpha Monitor (SWEPAM) instrument [*McComas et al.*, 1998] are used in later chapters. The spacecraft has enough propellant on board to maintain an orbit at L1 until 2019.

1.2 Magnetosphere and low-latitude magnetopause reconnection

The Earth's magnetic field provides an effective obstacle to the solar wind plasma. As the solar wind impacts the earth's magnetic field, its dynamic pressure presses on the outer boundary of the magnetic field, confining it to a cavity called the magnetosphere, which has a long tail consisting of two anti-parallel lobes of magnetic flux that stretch in the anti-solar direction, i.e. the magnetotail [*Walker and Russell*, 1995]. The boundary of the magnetosphere, i.e. magnetopause, is roughly bullet shaped, about 15 R_E in front of the earth and it is roughly a

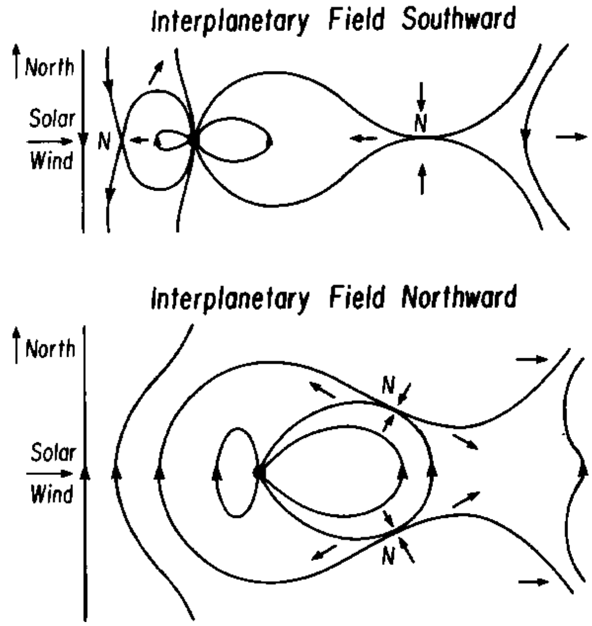

Figure 1.1 Topology of the magnetosphere for southward (upper panel) and northward (lower panel) interplanetary magnetic fields. Plasma flows are indicated by the arrows. From *Dungey* [1963].

cylinder with a radius approximately of 20 R_E in the magnetotail. The tail region stretches well past 200 R_E, and where it ends is not well known.

It is found that the magnetic field lines in a plasma with approximately opposed polarities can reconnect to different partners [e.g. *Parker*, 1957; *Sweet*, 1958; *Petschek*, 1964]. In other words, plasma originally on different flux tubes can be mixed on a single flux tube through reconnection. As envisioned by *Dungey* [1961], reconnection occurs at the magnetopause where interplanetary magnetic fields encounter geomagnetic fields (Figure 1.1). For simplicity, assume that the interplanetary magnetic field is directed predominantly southward. Then the magnetic field driven by the solar-wind will be approximately anti-parallel to the geomagnetic field at the sub-solar point. The low-latitude magnetopause reconnection occurs between fields of different origins. Then, instead of a purely geomagnetic field line with both ends attached to the earth and an interplanetary field line with both ends on the sun, an open field line with one end attached to the earth and the other end stretching out into interplanetary space is obtained. See the upper panel of Figure 1.1. When the IMF is northward-oriented, reconnection can occur between the interplanetary magnetic field and lobe field in the magnetotail, i.e., high-latitude magnetic

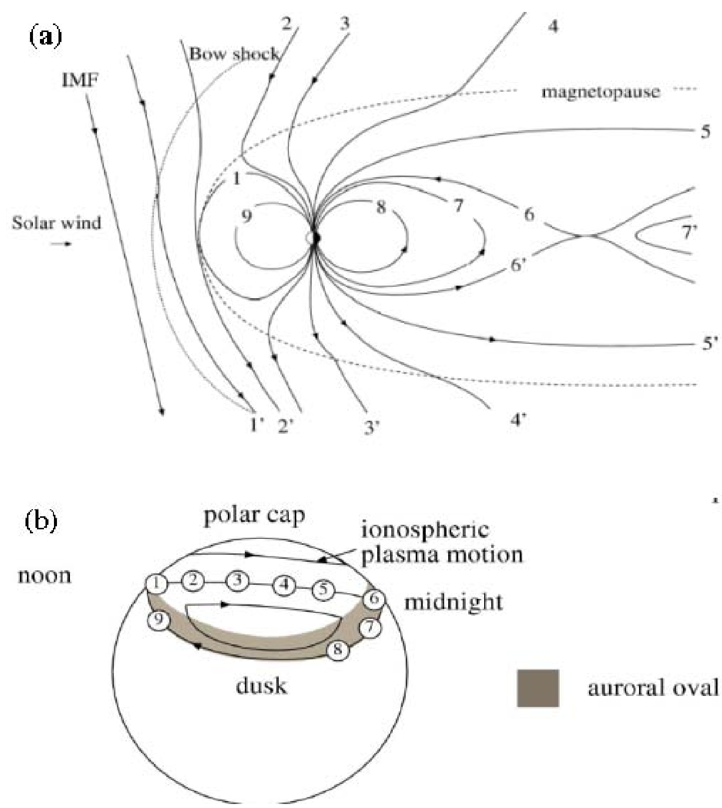

Figure 1.2 (a) Plasma convection within the magnetosphere driven by low-latitude magnetic reconnection. The numbered field lines show the succession of configurations a geomagnetic field line assumes after reconnection with an IMF field line at the front of the magnetosphere. Field lines 6 and 6’ reconnect at a second x-line in the tail, after which the field line returns to the dayside at lower latitude. (b) The positions of the feet of the numbered field lines in the northern high-latitude ionosphere and the corresponding high-latitude plasma flows, an anti-sunward flow in the polar cap, and a return flow at lower latitudes.

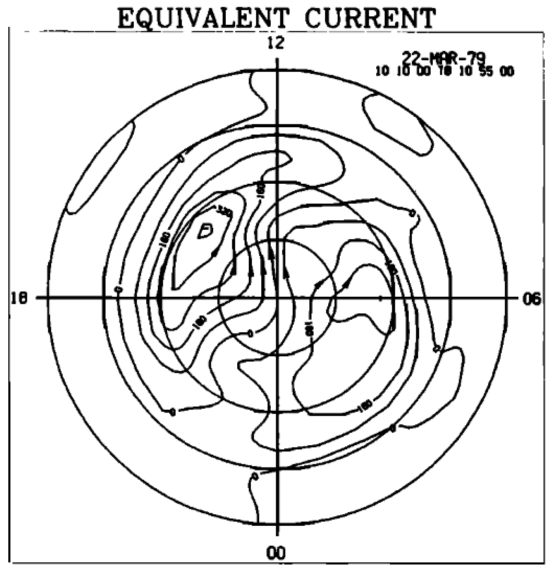

Figure 1.3 The two-cell DP-2 current system determined from magnetic disturbance. Closed contours show the flow lines for an equivalent ionospheric current that produces the observed ground magnetic perturbations. Reproduced by permission of American Geophysical Union from *Clauer and Kamide* [1985].

reconnection (lower panel of Figure 1.1). But, in this thesis, the latter process is not of relevance.

1.3 Polar cap: Convection and DP-2 currents

The region of open magnetic flux that connects the magnetic field of the earth to that of the solar wind is, by definition, the polar cap. The open field line is pulled anti-sunward by the solar wind, causing the plasma on the flux tube to sense an electric field. In a steady state, a magnetic field line is an equi-potential to a good approximation, and thus, the electric field must be sensed all along the open flux tube. At the ionospheric end, this electric field, pointing from dawn toward dusk, drives flows from noon toward midnight. Then, plasma flows back toward the dayside at somewhat lower latitudes on both the dawn and dusk sides (Figure 1.2) [e.g. *Hughes*, 1995]. This double-vortex flow pattern is roughly stationary in a sun-fixed coordinate system and termed "convection" due to its similarity to thermally driven flow cells, though it is in no sense thermally driven.

Associated with the plasma convection is a current system named the disturbance polar of the second type (DP-2) or convection electrojet (Figure 1.3), which produces ground magnetic disturbance. The currents, flowing at right angles to the ionospheric electric field, i.e. Hall currents, are produced by the drift of ionospheric charges in the presence of orthogonal electric and magnetic fields. In the weakly collisional ionosphere, electrons drift faster than ions, producing a current in a direction opposite to the plasma flow. The form of this convection pattern provided the initial insight into the coupling between solar wind and magnetosphere.

1.3.1 Cross polar cap potential: Measurements and saturation

The cross polar cap potential (Φ_{PC}) is defined as the potential drop across the open fields and measures the rate of magnetic flux transfer from the solar wind to the magnetosphere. It is widely regarded as an important parameter in characterizing the interaction between solar wind and magnetosphere.

Four techniques are commonly used to measure this parameter [e.g. *Gao*, 2012a]. Assimilative Mapping of Ionospheric Electrodynamics (AMIE) assimilates magnetic field data from ground magnetometers and electric field data from radars and satellites to map high-latitude electrostatic potentials, from which the difference of the potential extrema is used to estimate Φ_{PC} [*Richmond and Kamide*, 1988; *Richmond et al.*, 1988]; Defense Meteorological Satellite Program (DMSP) measures the cross-track ion drift velocity, and estimates Φ_{PC} by the difference of the potential extrema along the spacecraft trajectory [*Hairston et al.*, 1998]; the polar cap (PC) index is derived from the surface magnetic field perturbation [*Troshichev et al.*, 1988] and is empirically found to relate to Φ_{PC} through the formula of *Troshichev et al*. [1996], i.e.,

$$\Phi_{PC}\,[\text{kV}] \approx 19.35\text{PC} + 8.78; \qquad (1.1)$$

(See also *Ridley and Kihn* [2004] for a different empirical formula to convert from the PC index to Φ_{PC}.) Super Dual Auroral Radar Network (SuperDARN) measures the line-of-sight ionospheric convection velocities with a ground-based network of radars and then infers functional forms of the electrostatic potential and Φ_{PC} is obtained from the difference of the potential extrema [*Ruohoniemi and Baker*, 1998].

It is found that the cross polar cap potential varies approximately linearly with the solar wind electric field for nominal conditions, but asymptotes to a constant value of order 200 kV for large electric field. The saturation of cross polar cap potential is consistent with observations [*Shepherd et al*., 2002; *Nagatsuma*, 2002a; *Hairston et al.*, 2003; *Ober et al.*, 2003], and is found to occur in MHD simulations [e.g. *Raeder et al.*, 2001; *Siscoe et al.*, 2002; *Merkine et al.*, 2003]. Several models were proposed to explain the saturation of Φ_{PC} [*Siscoe et al.*, 2002; 2004; *Kivelson and Ridley*, 2008; *Borovsky et al.*, 2009]. However, its physical mechanism is still in debate. See *Borovsky et al.* [2009] for a comparison of several saturation models.

1.4 Geomagnetic substorm and DP-1 currents

A geomagnetic substorm is a brief disturbance (about an hour) in the Earth’s magnetosphere that causes energy to be released from the magnetotail and injected into the high-latitude ionosphere. A substorm is seen as a sudden brightening of auroral arcs. The magnetic field in the auroral zone can change by 1000 nT or more. In general, substorms occur roughly six times per day, though they are more intense and more frequent during a geomagnetic storm.

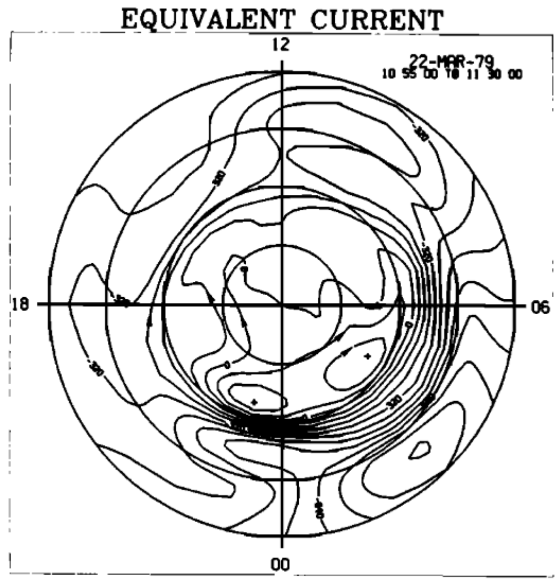

Figure 1.4 The single-cell DP-1 current system during the substorm expansion phase. Reproduced by permission of American Geophysical Union from *Clauer and Kamide* [1985].

Substorms are distinct from geomagnetic storms in that the latter take place over a period of several days and are observable from anywhere on Earth. Storms also inject a large number of ions into the outer radiation belt, and occurs once or twice a month during the maximum of the solar cycle and a few times a year during solar minimum. The source of the magnetic disturbances observed at the Earth's surface during geomagnetic storms is the ring current, whereas the sources of magnetic disturbances observed on the ground during a substorm are electric currents in the ionosphere at high latitudes.

The current system during a substorm is fundamentally different from the two-cell pattern previously described. The main characteristic of this current system is the sudden enhancement of the westward electrojet cross the midnight sector. According to *Akasofu et al.* [1965], a westward current begins to flow along the newly brightened auroral arc. They also believed that the pattern was primarily a single cell centered at midnight, with strong currents across the auroral bulge and weaker return currents at both higher and lower latitudes. This current system is referred to as disturbance polar of the first type (DP-1), also the substorm electrojet (Figure 1.4).

1.5 Coupling functions

The magnetospheric dynamo is primarily governed by its solar wind driver through low-latitude magnetopause reconnection [e.g. McPherron, 1995]. Due to its importance, the solar wind-magnetosphere coupling has attracted attention of many studies [*Dungey,* 1961; *Vasyliunas*, 1975; *Daughton et al.*, 2011]. One purpose of such studies is to predict the state of magnetosphere from solar wind input. For example, *Weimer* [1996; 2001; 2005] empirically modeled the high-latitude electric potential as a function of solar wind parameters by constructing a spherical harmonic expansion and fitting the coefficients to the DE-2 satellite data. *Kan and Lee* [1979] assumed an idealized reconnecting field line geometry and derived a electric field resulting from low-latitude magnetopause reconnection, whose consistency with polar cap magnetic field disturbance was later reported by *Troshichev et al*. [1988]. Besides, global MHD simulations are often used for such studies [e.g. *Raeder et al.*, 2001; *Siscoe et al.*, 2002; *Merkine et al.*, 2003]. To model the coupling process by using a coupling function of solar wind and magnetospheric parameters is appealing, since a coupling function is usually simple enough to help understand the underlying physics.

A coupling function is usually related to the rate of energy, momentum or magnetic flux transfer rate from the solar wind to the magnetosphere . The earliest coupling functions are dynamic pressure (p_{dyn}) [*Chapman and Ferraro*, 1931] and IMF B_Z [*Dungey*, 1961]. Soon, it was realized that p_{dyn} does not directly predict geomagnetic activity, and B_Z, though important in controlling magnetopause reconnection, does not correlate well with geomagnetic indices. The first non-trivial coupling function was the half-wave rectifier (vB_s) proposed by *Burton et al*. [1975], which correlates well with D_{st} and has been widely used in later studies [e.g. *Bargatze et al*., 1985]. Here, v is the solar wind bulk velocity, and B_s is related to IMF B_Z through

$$B_s = -B_Z \text{ for } B_Z < 0 \text{ and } B_s = 0, \text{ for } B_Z \geq 0. \quad (1.2)$$

In the following three decades, various coupling functions have been proposed [e.g. *Wygant et al*., 1983; *Reiff and Luhmann*, 1986; *Scurry and Russell*, 1991]. These functions can be summarized in the form

$$F_c = n^{\alpha} v^{\beta} B^{\gamma} G(\theta), \quad (1.3)$$

where n is the solar wind number density, B is the IMF magnitude, θ is the IMF clock angle measured clockwise from the GSM Z axis in a plane perpendicular to the earth-sun line, and α, β, γ are numbers. Here, $G(\theta)$ is frequently assumed to vary as

$$G(\theta) = \sin^{\delta}\theta/2, \quad (1.4)$$

where δ is a number [e.g. *Kan and Lee*, 1979]. The coupling functions often encountered in literature include the ε parameter of *Perrault and Akasofu* [1978], the merging electric field ($E_{\mathrm{K\text{-}L}}$) of *Kan and Lee* [1979], the universal coupling function (Φ_N) of *Newell et al*. [2007]. See Chapter 2 for their definitions as well as those less often encountered coupling functions.

1.6 Geomagnetic indices: State variables of magnetosphere

Geomagnetic indices are often used to quantify the state of the magnetosphere, and thus, provide useful tools to evaluate various coupling functions. Through the 20th century, various magnetic indices were defined in studies of solar-terrestrial physics. An index is a monotonic function of some important physical parameter related to the phenomenon causing the disturbance [*McPherron*, 1995]. In practice, an index is easily defined and derived with high time resolution, continuous coverage and, ideally, global scope. Following the above philosophy, commonly used indices include the disturbance storm time (D_{st}) index, the planetary K (K_p) index, the auroral electrojet (AE) index, and the polar cap (PC) index. The D_{st} index, constructed by averaging the horizontal component of the geomagnetic field from 4 mid-latitude and equatorial stations, measures the strength of the ring current. The K_p index, obtained from 13 mid-latitude stations, measures general planetary wide geomagnetic disturbances at mid-latitude. The AE index, computed from 12 auroral zone observatories, measures the strength of the auroral electrojets. The PC index was derived from a single station located in the polar cap to approximate the electric field of *Kan and Lee* [1979]. Since the PC index is measured from a single station, it is questionable whether this index can quantify the state of magnetosphere. The generality of the PC index is justified by its high correlation with many ionospheric parameters on a global scale, e.g. cross polar cap potential [*Troshichev et al.*, 1996; *Ridley and Kihn*, 2004], hemispheric Joule heating rate [*Chun et al.*, 1999; 2002], auroral power [*Liou et al.*, 2003], etc. For over a century, studies of solar-terrestrial physics have relied heavily on these indices.

1.6.1 Auroral electrojet (AE) index

The auroral electrojet index is used to quantify the strength of a substorm. This index was defined by *Davis and Sugiura* [1966] to obtain a measure of the strength of the auroral electrojets. The horizontal magnetic field disturbances of 12 observatories almost uniformly distributed in auroral zone in the Northern Hemisphere are selected to derive the AE index. Monthly mean values are first subtracted from each station's trace to give a base value of zero. The traces are then plotted with respect to a common baseline, and upper and lower envelopes are calculated.

The AU (auroral upper) index is defined at any instant of time as the maximum positive disturbance recorded by any station in the chain. Similarly, AL is defined as the minimum disturbance defined by the lower envelope. If the disturbances were caused by an infinite sheet current, then AU and AL would be proportional to the maximum overhead current density in the two electrojets. A single measure that approximates the total effect of both electrojets is defined as AE = AU – AL.

1.6.2 Polar cap (PC) index

The polar cap (PC) index, derived from surface magnetic field disturbances, is a model based index used to monitor the electric field resulting from low-latitude magnetopause reconnection. *Troshichev et al*. [1988] found that, by projecting the surface magnetic field perturbation to the direction perpendicular to the mean transpolar DP-2 current, the resulting quantity (ΔF_{PROJ}) varies approximately linearly with the merging electric field of *Kan and Lee* [1979] ($E_{\mathrm{K\text{-}L}}$), i.e.,

$$\Delta F_{\mathrm{PROJ}} \approx \alpha E_{\mathrm{K\text{-}L}} + \beta. \tag{1.5}$$

Thus, by defining

$$\mathrm{PC} = (\Delta F_{\mathrm{PROJ}} - \beta)/\alpha, \tag{1.6}$$

the resulting PC index directly approximates $E_{\mathrm{K\text{-}L}}$, i.e.,

$$\mathrm{PC} \approx E_{\mathrm{K\text{-}L}}. \tag{1.7}$$

The PC index is derived from one station located within the polar cap for each hemisphere: Qaanaaq at 86.5° magnetic latitude for the northern PC index (PCN), Vostok at –83.4° magnetic latitude for the southern PC index (PCS). See *Stauning* [2011] for a more detailed derivation of the PC index.

1.7 Outline of the thesis

In this thesis, I investigate how the polar cap dynamics, quantified by the PCN index, responds to its solar wind driver and magnetotail driver during intervals of strong geomagnetic activity. Further introduction and review of related work will be given in the corresponding chapters.

In Chapter 2, I examine 53 one to two-day intervals that include exceptionally large (10 mV/m) merging electric field and find that, among 11 candidate coupling functions including the merging electric field of *Kan and Lee* [1979], and universal coupling function of *Newell et al*. [2007], the PCN index correlates most closely with the electric field ($E_{\text{K-R}}$) of *Kivelson and Ridley* [2008]. Here, $E_{\text{K-R}}$ is a form in which the electric field imposed on the ionosphere by low-latitude magnetopause reconnection saturates at high levels of geomagnetic activity. I also find that the magnetotail processes, as represented by an unloading AL index, denoted as AL_U, make a significant contribution to the PCN index. A linear model is constructed to relate the polar cap index to its solar wind driver ($E_{\text{K-R}}$) and magnetotail driver (AL_U), i.e., $\text{PCN} \approx \beta_0 + \beta_1 zs(E_{\text{K-R}}) + \beta_2 zs(\text{AL}_\text{U})$, where β_0, β_1, and β_2 are constants estimated from regression, and $zs(\cdot)$ is a normalization function. The solar wind dynamic pressure (p_{dyn}) does not play a key role in controlling the PCN index. However, under intense solar wind driving, the number density (n) can influence the solar wind-magnetosphere coupling through solar wind Alfvén conductance, which is incorporated in $E_{\text{K-R}}$.

In Chapter 3, I examine the validity of the linear approximation between the PCN index and $E_{\text{K-R}}$, AL_U, as assumed in Chapter 2. The results of the linear model are compared to those obtained from a more flexible, non-linear model, $\text{PCN} \approx \alpha + f_1(E_{\text{K-R}}) + f_2(\text{AL}_\text{U})$, where α is a constant, and $f_1(\cdot)$, $f_2(\cdot)$ are arbitrary smooth functions. I find that the results of the two models are close to each other, which indicates that the linear assumption is, in general, valid. However, there are anomalous events during which the auroral oval expanded poleward to the latitude of Qaanaaq and the PCN index increased because of proximity to auroral zone currents. For such events, the linear model fails.

In Chapter 4, the linear model is applied to most of the days in solar cycle 23 to study the relative driven and unloading portion of the PCN index. A driven-to-unloading ratio (*DUR*) is defined based on the regression coefficients, i.e., $DUR = |\beta_1/\beta_2|$, and its long-term variation with solar cycle is investigated. I find that, near solar maximum, the relative driven contribution decreases. Besides, a seasonal variation of *DUR* is observed. Namely, *DUR* is enhanced in summer, and decreases in winter.

Although $E_{\text{K-R}}$ is successful in explaining the polar cap magnetic disturbance at high levels of geomagnetic activity by taking saturation into account, a competing saturation model by *Siscoe et al*. [2002] exists. In Chapter 5, these two models are compared and their predictions are compared with measurements (AMIE, DMSP, PC index, and SuperDARN). It is found that, in the saturation limit, these two models give almost identical predictions. Given the great uncertainties in measurements, it is impossible to prefer one model to the other.

Finally, the conclusions of this thesis are summarized in Chapter 6. Finally, possible future works are discussed.

CHAPTER 2

A Linear Model for Solar Wind-Magnetosphere Coupling

2.1 Introduction

The earth's magnetosphere dynamo is primarily governed by two types of processes. They have been categorized as driven processes and unloading processes [*McPherron and Baker*, 1993]. A driven process is one for which the output, often measured by a geomagnetic index, is proportional to the solar wind input with at most a small time delay. The DP-2 current system is powered by the direct projection of the solar wind electric field onto the conducting ionosphere [*Iijima and Nagata*, 1972; *Kokubun*, 1972]. In contrast, an unloading process is one in which the magnetosphere accumulates energy without a corresponding output until, after a substantial time delay, energy is unloaded, often abruptly. As envisioned by *Akasofu* [1979b], the unloading process is internal to the magnetosphere, and hence, its wave form bears little resemblance to the input. The DP-1 current system is powered by processes internal to the plasma sheet [McPherron and Baker, 1993]. Measured by the AL index, it has been shown that magnetospheric activity is controlled by both driven processes and unloading processes [*Bargatze et al.*, 1985]. The polar cap is typically open to the solar wind, so it is believed to respond primarily to the direct driving of solar wind [*Troshichev et al.*, 1988; 1996]. In previous studies [e.g. *Troshichev et al.*, 1988;

1996], direct coupling between the solar wind and polar cap was established by correlating the PC index with the merging electric field of *Kan and Lee* [1979].

The PC index, therefore, has been interpreted as a way of quantifying the portion of magnetospheric activity directly driven by the solar wind [1988]. The algorithm from which the index is calculated is based on a statistical analysis of the relationship between variations in merging electric field ($E_{\text{K-L}}$) [*Troshichev et al.*, 1988] and geomagnetic perturbations of the local magnetic field (ΔF_{PROJ}) at a high-latitude station on the Earth's surface. The merging electric field is related to the solar wind parameters through

$$E_{\text{K-L}} = vB_{YZ}\sin^2\theta/2, \tag{2.1}$$

where v is the magnitude of the solar wind velocity,

$$B_{YZ} = (B_Y^2+B_Z^2)^{1/2} \tag{2.2}$$

in the GSM coordinate system, and θ is the IMF clock angle measured from the GSM Z axis in a plane perpendicular to the earth-sun line.

Two near-pole magnetic observatories have been used for derivations of the PC index: Qaanaaq in Greenland at 86.5° magnetic latitude for the northern PC index (PCN), and Vostok in Antarctica at –83.4° magnetic latitude for the southern PC index (PCS) [*Troshichev et al.*, 2006]. The surface magnetic field perturbations are caused by the ionospheric Hall currents. Thus, the perturbations are expected to be approximately perpendicular to the transpolar DP-2 currents. ΔF_{PROJ} is defined as the perturbation in this direction, i.e.,

$$\Delta F_{\text{PROJ}} = \Delta H\sin\gamma + \Delta D\cos\gamma, \tag{2.3}$$

where ΔH and ΔD are deviations in the ground horizontal (H and D) magnetic field components from a pre-established quiet level, and

$$\gamma = \lambda \pm D_E + \varphi + \mathrm{UT} \cdot 15^o. \tag{2.4}$$

For PCN, the reference is the internal field level, whereas, for PCS, the reference is the quiet level, which is the sum of the internal field and a quiet day curve (QDC) [*Janzhura and Troshichev*, 2008]. In equation (2.4), D_E is the station's declination angle with "+" for the Southern Hemisphere and "–" for the Northern Hemisphere, λ is its geographical longitude, and φ, is the UT-dependent angle between the average DP-2 transpolar current and the noon-midnight meridian [*Stauning*, 2011]. *Troshichev et al.* [1988] showed that ΔF_{PROJ} varies approximately linearly with the merging electric field, i.e.,

$$\Delta F_{PROJ} \approx \alpha E_{K\text{-}L} + \beta. \tag{2.5}$$

The PC index is defined as

$$\mathrm{PC} = (\Delta F_{PROJ} - \beta) / \alpha\eta, \tag{2.6}$$

where η = 1mV/m is a normalization coefficient introduced to make the PC index dimensionless. Thus, in principle,

$$\mathrm{PC} \approx E_{K\text{-}L}. \tag{2.7}$$

Stauning [2011] discussed the derivation of the PC index in more detail.

Since its definition, various statistical analyses have demonstrated that the PC index can be regarded as an instantaneous estimator of diverse ionospheric phenomena. For example, *Troshichev et al.* [1996] related the PC index to the cross polar cap potential (Φ_{PC}) measured by EXOS-D and obtained a linear relationship,

$$\Phi_{PC}\,[\mathrm{kV}] \approx 19.35\mathrm{PC} + 8.78. \tag{2.8}$$

Ridley and Kihn [2004] took seasonal effects into account and proposed a different formula to convert from the PC index to the cross polar cap potential measured by AMIE,

$$\Phi_{PC}\,[\mathrm{kV}] \approx 29.28 - 3.31\sin(T+1.49) + 17.81\mathrm{PC}, \tag{2.9}$$

where T is the month of the year normalized to 2π, i.e.,

$$T = (\text{month} - 1) \times 2\pi/12. \tag{2.10}$$

For example, January = 0, July = π, December = $11 \times 2\pi/12$. *Troshichev et al.* [2000]related the cross polar cap electric field measured by DMSP to the PC index using a second order polynomial. *Fiori et al.* [2009] confirmed the relationship proposed by *Troshichev et al.* [2000] by obtaining a similar result between the ionospheric plasma convection velocity and the PC index. *Liou et al.* [2003] examined the statistical relationship between auroral power and the polar cap index and found a reasonably large correlation coefficient ($\rho \approx 0.7$). *Chun et al.* [1999; 2002] have shown that the PC index can serve as a proxy for the hemispheric Joule heating production rate and claimed that it is possible to predict the Joule heating pattern from the PC index. Since the algorithm used to derive the PC index has evolved dramatically, discrepancies in results from different studies may be attributed in part to the use of different forms of the PC index.

Despite the general success in describing how the solar wind affects the polar ionosphere using the PC index, few studies have paid attention to times of intense geomagnetic activity. However, the saturation of cross polar cap potential at such times has been extensively discussed [*Russell et al.*, 2000; *Nagatsuma*, 2002a; *Shepherd et al.*, 2002; *Siscoe et al.*, 2002; 2004; *Kivelson and Ridley*, 2008]. In exploring the physical mechanism of the saturation of the cross polar cap potential, *Kivelson and Ridley* [2008] took into consideration the partial reflection of the merging electric field ($E_{\text{K-L}}$)at the top of the ionosphere and proposed that the electric field observed in the ionosphere ($E_{\text{K-R}}$) would differ from that directly imposed from the solar wind, i.e.,

$$E_{\text{K-R}} = E_{\text{K-L}}\, 2\Sigma_A/(\Sigma_P+\Sigma_A), \tag{2.11}$$

where $2\Sigma_A/(\Sigma_P+\Sigma_A)$ is the transmission coefficient. In equation (2.11), Σ_P is the ionospheric Pedersen conductance, and Σ_A is the solar wind Alfvén conductance. Here

$$\Sigma_A = 1/\mu_0 v_A, \tag{2.12}$$

where v_A is the solar wind Alfvén velocity,

$$v_A = B \,/\, (\mu_0 \rho_{sw})^{1/2}, \tag{2.13}$$

ρ_{sw} is the solar wind mass density, and $\mu_0 = 4\pi\times10^{-7}$ H/m is the permeability of free space. Under typical solar wind conditions, e.g. $E_{K\text{-}L} < 5$ mV/m, $\Sigma_A \approx 16$ S, which is slightly larger than but close to Σ_P. Thus,

$$E_{K\text{-}R} \approx 1.2\, E_{K\text{-}L}. \tag{2.14}$$

Nevertheless, under intense solar wind driving, e.g. $E_{K\text{-}L} > 10$mV/m, Σ_A decreases to such an extent that $\Sigma_A < \Sigma_P$, and thus,

$$E_{K\text{-}R} < E_{K\text{-}L}. \tag{2.15}$$

It has been argued that $E_{K\text{-}R}$ serves as a better indicator of the electric field in the ionosphere caused by the low-latitude magnetopause reconnection than does $E_{K\text{-}L}$, especially when $E_{K\text{-}L}$ is unusually large. Consequently, it is of interest to consider which of the two forms of the electric field correlates more closely with the driving convection in the polar cap by investigating the behavior of the PC index during exceptionally active intervals.

Different mechanisms have been proposed to explain the saturation of cross polar cap potential [e.g. *Borovsky et al.*, 2009]. For example, *Siscoe et al.* [2002; 2004], who adopted and developed the model by *Hill et al.* [1976], argued that the saturation of cross polar cap potential results from a feedback in which the magnetic field generated by the Region-1 current becomes comparable to and opposes the earth's dipole field at the magnetopause where reconnection occurs. By significantly weakening the field that is reconnecting, the Region-1 current ultimately limits how fast reconnection occurs, resulting in the saturation of cross polar cap potential. Although the physical mechanism proposed by *Siscoe et al.* [2002; 2004] is fundamentally different from that of *Kivelson and Ridley* [2008], the predicted electric fields from the two models are similar. In Chapters 2, 3 and 4, $E_{\text{K-R}}$ is used as representative of the electric field imposed on the polar ionosphere by low-latitude magnetopause reconnection that takes saturation into account. See *Borovsky et al.* [2009] for a review of many saturation models. The saturation model of *Kivelson and Ridley* [2008] is compared to that of *Siscoe et al*. [2002] in Chapter 5.

Unlike the PC index, the auroral electrojet (AE) index is meant to estimate the release of energy stored in the magnetotail during substorms. Although it is often assumed that the PC index is not significantly affected by substorm dynamics in the magnetotail, previous studies have shown that the correlation between the PC and the AE indices is high. *Vennerstrøm et al.* [1991] showed that the PC index correlates well with the AE and AL indices, with the correlation coefficient being equal to 0.8-0.9 in winter and 0.6-0.8 in summer. *Huang* [2005] examined the relationship between the PC index and substorm activity and found that the PC index is enhanced after substorm onset. Thus, the PC index, due to its great simplicity, provides an excellent tool for quantifying the influence on the polar cap dynamics of both the solar wind driver and the magnetospheric unloading process.

The solar wind dynamic pressure (p_{dyn}) has also been found to influence the PC index [*Lukianova*, 2003]. *Lukianova* [2003] examined the relationship between $E_{\text{K-L}}$, p_{dyn}, and the PC and AE indices in detail and concluded that the PC index directly responds to an enhancement in p_{dyn} and the influence of p_{dyn} pulses can be as large as the influence of southward IMF.

Troshichev et al. [2007] carried out a superposed epoch analysis of 62 pressure jumps between 1998 and 2002 and concluded that the solar wind pressure growth rate (i.e., the jump in power, dp_{dyn}/dt) appears to be the second most important factor after $E_{\mathrm{K\text{-}L}}$ in controlling variations of the PC index (see also *Stauning and Troshichev* [2008]). *Stauning et al.* [2008] examined the relationship between the PC index and the dynamic pressure for typical conditions and found little correlation between the PC index and the steady state solar wind dynamic pressure. *Huang* [2005] performed both case study and statistical analysis on the role of solar wind dynamic pressure pulse on the PC index under many solar wind conditions and concluded that, on average, the solar wind dynamic pressure is less important than either the solar wind electric field or substorm activity.

In this chapter, I investigate the influence of the solar wind and magnetotail activity on polar cap dynamics by studying the relationship between the PCN index and various solar wind-magnetosphere coupling functions as well as geomagnetic indices. I focus on intervals of intense geomagnetic activity for which the coupling functions are likely to be different. I apply regression analysis to 53 one to two-day intervals from 1998 to 2006 with subintervals during which the cross polar cap potential predicted by equation (2.8) exceeds 150 kV. It is found that, (1) among the 11 candidate coupling functions, the PCN index correlates best with $E_{\mathrm{K\text{-}R}}$; (2) the PCN index is influenced by both external and internal flows, i.e. by the solar wind as characterized by the electric field of *Kivelson and Ridley* [2008] ($E_{\mathrm{K\text{-}R}}$) and by magnetotail activity as represented by an unloading AL index ($\mathrm{AL_U}$); (3) the dayside input, or equivalently, the electric field of the solar wind contributes more than the nightside input or, equivalently, the energy release in substorms; (4) if the effect of varying solar wind density is attributed to the modified electric field, $E_{\mathrm{K\text{-}R}}$, the residual PCN index does not respond directly to p_{dyn} or jumps in

p_{dyn}; (5) the auroral oval may, on occasion, expand poleward to as far north as Qaanaaq (86.5^o magnetic latitude), in which case the PCN index records the effects of currents flowing on nearby closed field lines and may become unusually large.

Table 2.1 One to Two-Day Intervals Between 1998 and 2006 with Subintervals during Which Equation (2.16) is met. Reproduced by permission of American Geophysical Union from *Gao et al.* [2012c].

4 May 1998	27 March 2001	14 October 2003
29 May 1998	31 March 2001	24 October 2003
26-27August 1998	4 April 2001	31 October 2003
24-25 September 1998	8 April 2001	4 November 2003
8 November 1998	11-12 April 2001	20 November 2003
18 February 1999	18 April 2001	6 January 2004
22 September 1999	28 April 2001	22 January 2004
21-22 October 1999	17 August 2001	25-26 July 2004
27 January 2000	3 October 2001	7-8 November 2004
12 February 2000	21 October 2001	7 January 2005
6-7 April 2000	30 December 2001	17 January 2005
23 -24 May 2000	17 April 2002	21 January 2005
8 June 2000	19-20 April 2002	8 May 2005
13 July 2000	23 May 2002	15 May 2005
16 July 2000	7 September 2002	24 August 2005
12 August 2000	21 November 2002	15 September 2005
17-18 September 2000	29-30 May 2003	14-15 December 2006
5 October 2000	18 August 2003	

2.2 Analysis

In this chapter, I concentrate on geomagnetically-active times when the PCN index exceeds a baseline value. The cases are extreme cases that include intervals during which the cross polar cap potential predicted from the PCN index using equation (2.8) exceeds 150 kV, i.e.,

$$\Phi_{PC} \approx 19.35\ PC + 8.78 > 150\ \mathrm{kV} \tag{2.16}$$

and typically $E_{K\text{-}L}$ > 10 mV/m and PCN > 5. Using this criterion, I select 53 one to two-day intervals between 1998 and 2006 (shown in Table 2.1).

2.2.1 The electric field of *Kivelson and Ridley* [2008], $E_{K\text{-}R}$

According to *Kivelson and Ridley* [2008], when the impedance of the solar wind across open polar cap field lines dominates the impedance of the ionosphere, Alfvén waves incident from the solar wind are partially reflected, reducing the strength of the signal in the polar cap. Thus the ratio of the cross polar cap electric field to the merging electric field imposed by the solar wind is $2\Sigma_A/(\Sigma_A+\Sigma_P)$, i.e.,

$$E_{K\text{-}R} = E_{K\text{-}L} 2\Sigma_A/(\Sigma_A + \Sigma_P). \tag{2.17}$$

This form has the interesting property of depending on both solar wind and ionospheric properties. In addition, if the density variation from solar wind to ionosphere along a field line is taken into account, Σ_A is computed from

$$\Sigma_A = (\rho_{pc}/\rho_{sw})^{1/4}\ (1/\mu_0 v_A), \tag{2.18}$$

where ρ_{pc}, depending on ρ_{sw}, is the mass density in the low-altitude polar cap (e.g. $2R_E$) at the top of the ionosphere. Probable values of $(\rho_{pc}/\rho_{sw})^{1/4}$, insensitive to solar wind conditions, are likely to differ from 1 by no more than a factor of 2. As the values of ρ_{pc} are not routinely measured [*Kitamura et al.*, 2011], one should use $\Sigma_A = 1/\mu_0 v_A$ with the understanding that this introduces errors of a few tens of percent in the calculations. (For details, please refer to the appendix of *Kivelson and Ridley* [2008]) Σ_P is the ionospheric Pedersen conductance chosen to be 10 S [*Kivelson and Ridley*, 2008]. I also run the analyses using values of 5 S and 15 S for Σ_P and find that the conclusion remains unchanged from those reached when Σ_P is 10 S.

Table 2.2 Solar Wind-Magnetosphere Coupling Functions With Definition and Reference In Chronological Order[1]. Reproduced by permission of American Geophysical Union from *Gao et al.* [2012c].

Coupling Function	**Reference**
$E_B = vB_s$	*Burton et al.* [1975]
$\varepsilon_{P\text{-}A} = vB^2\sin^4\theta/2$	*Perrault and Akasofu* [1978]
$E_{K\text{-}L} = vB_{YZ}\sin^2\theta/2$	*Kan and Lee* [1979]
$\varepsilon_V = n^{1/6}v^{5/3}B_{YZ}\sin^2\theta/2$	*Vasyliunas et al.* [1982]
$\Phi_P = n^{-1/2}B^2\sin^3\theta/2$	*Pudovkin et al.* [1982]
$E_W = vB_{YZ}\sin^4\theta/2$	*Wygant et al.* [1983]
$p_{T\text{-}A} = n^{1/2}vB_{YZ}\sin\theta/2$	*Troshichev and Andrezen* [1985]
$\varepsilon_{S\text{-}R} = n^{1/6}v^{4/3}B_{YZ}\sin^4\theta/2$	*Scurry and Russell* [1991]
$\varepsilon_{T\text{-}L} = n^{1/2}v^2B_{YZ}\sin^6\theta/2$	*Temerin and Li* [2006]
$\Phi_N = v^{4/3}B_{YZ}^{2/3}\sin^{8/3}\theta/2$	*Newell et al.* [2007]
$E_{K\text{-}R} = E_{K\text{-}L}2\Sigma_A/(\Sigma_A + \Sigma_P)$	*Kivelson and Ridley* [2008]

[1] Here, E represents an electric field coupling function, Φ indicates a magnetic flux transfer function, ε indicates an energy transfer function, and p stands for a momentum transfer function. In these formulas, B is the IMF magnitude, and B_{YZ} is defined in equation (2.2) in GSM coordinates.

Table 2.3 Correlation Coefficients Linking the PCN Index with Various Coupling Functions Purported to Quantify the Strength of Solar Wind-Magnetosphere Interaction[2]. Reproduced by permission of American Geophysical Union from *Gao et al.* [2012c].

	PCN	E_B	$\varepsilon_{P\text{-}A}$	$E_{K\text{-}L}$	ε_V	E_P	E_W	$p_{T\text{-}A}$	$\varepsilon_{S\text{-}R}$	$\varepsilon_{T\text{-}L}$	Φ_N	$E_{K\text{-}R}$
PCN	1.00	0.70	0.78	0.71	0.77	0.46	0.71	0.84	0.82	0.80	0.78	0.87
E_B		1.00	0.88	0.97	0.95	0.90	1.00	0.84	0.91	0.92	0.86	0.79
$\varepsilon_{P\text{-}A}$			1.00	0.90	0.91	0.73	0.90	0.86	0.89	0.86	0.99	0.87
$E_{K\text{-}L}$				1.00	0.99	0.90	0.99	0.89	0.90	0.88	0.88	0.82
ε_V					1.00	0.83	0.97	0.95	0.95	0.92	0.90	0.88
E_P						1.00	0.90	0.63	0.67	0.67	0.90	0.51
E_W							1.00	0.87	0.92	0.91	0.87	0.81
$p_{T\text{-}A}$								1.00	0.97	0.92	0.85	0.95
$\varepsilon_{S\text{-}R}$									1.00	0.99	0.87	0.93
$\varepsilon_{T\text{-}L}$										1.00	0.84	0.90
Φ_N											1.00	0.90
$E_{K\text{-}R}$												1.00

I first compare the correlation between the PCN index and $E_{K\text{-}R}$ with correlations between the PCN index and the previously-proposed coupling functions between the solar wind and the earth's magnetosphere shown in Table 2.2. Table 2.3 shows the correlation coefficients among the PCN index and those coupling functions during an event on 20 November 2003. The PCN index correlates best with $E_{K\text{-}R}$, with correlation coefficient 0.87.

[2] The solar wind are propagated to $X_{GSM} = 17\ R_E$ using the technique of *Weimer et al.* [2003] and *Weimer* [2004].

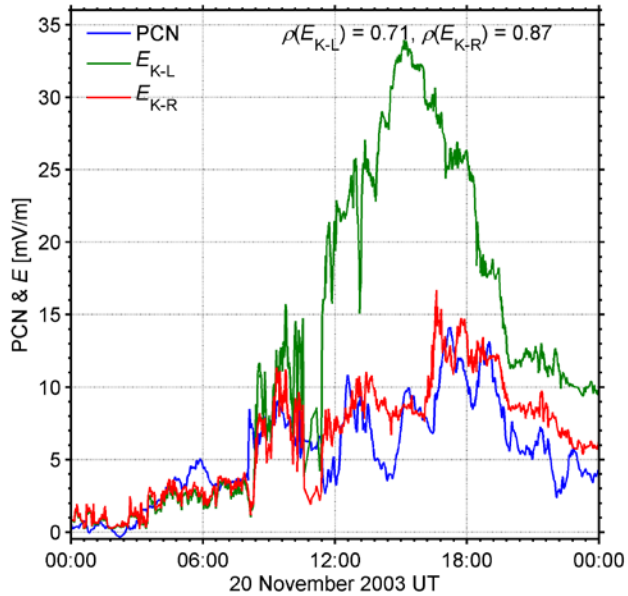

Figure 2.1 The PCN index, merging electric field of *Kan and Lee* [1979] (E_{K-L}) and the electric field of *Kivelson and Ridley* [2008] (E_{K-R}) on 20 November 2003. Here, E_{K-L} and E_{K-R} are calculated from the propagated solar wind data without additional time shift. The blue line is the measured PCN index. The green line is E_{K-L} in mV/m. The red line is E_{K-R} in mV/m evaluated for Σ_P = 10 S. Reproduced by permission of American Geophysical Union from *Gao et al.* [2012c].

In Figure 2.1, the time series of the PCN index (blue), the merging electric field of *Kan and Lee* [1979] (green) and the electric field of *Kivelson and Ridley* [2008] (red) are plotted. For values of $E_{K-L} < 5$ mV/m, there was little difference between E_{K-L} and E_{K-R}, but for larger values of E_{K-L} and especially between 12:00 UT and 18:00 UT, E_{K-L} and E_{K-R} differed considerably. The PCN index obviously followed E_{K-R} more closely.

I also compare correlations obtained from regression analyses with the PCN index as the dependent variable and both E_{K-L} and E_{K-R} as independent variables, i.e.,

$$\mathrm{PCN} = \beta_{0,K-L} + \beta_{1,K-L}E_{K-L} + \varepsilon_{K-L}, \tag{2.19}$$

and

$$\mathrm{PCN} = \beta_{0,\mathrm{K\text{-}R}} + \beta_{1,\mathrm{K\text{-}R}} E_{\mathrm{K\text{-}R}} + \varepsilon_{\mathrm{K\text{-}R}}, \tag{2.20}$$

where $\beta_{0,\mathrm{K\text{-}L}}$, $\beta_{1,\mathrm{K\text{-}L}}$, $\beta_{0,\mathrm{K\text{-}R}}$, and $\beta_{1,\mathrm{K\text{-}R}}$ are regression coefficients, and $\varepsilon_{\mathrm{K\text{-}L}}$ and $\varepsilon_{\mathrm{K\text{-}R}}$ are assumed to be Gaussian noise. Recall that the *Weimer et al.* [2003] and *Weimer* [2004] technique is used to propagate the solar wind from ACE to $X_{\mathrm{GSM}} = 17\ R_{\mathrm{E}}$. *Ashour-Abdalla et al.* [2008] compared properties of the solar wind propagated from $L1$ with properties directly observed by a near-earth satellite (e.g. Geotail). They found general consistency between the propagated solar wind and observed solar wind, although they differed in some cases. Differences are more frequently observed during active times. See also *Ridley* [2000]. Therefore, I add time shifts for each individual event to obtain the maximum cross-correlations between the PCN index and $E_{\mathrm{K\text{-}L}}$ and between the PCN index and $E_{\mathrm{K\text{-}R}}$ respectively. The added time shifts are typically between 0 and 20 minutes with peak occurrence close to 12 minutes. Given the great complexity of establishing time delays between solar wind quantities and the PCN index, a cross-correlation analysis provides only an approximation to the precise time delay, but the uncertainty does not mask the correlations that are studied.

In order to compare the degree to which the PCN index can be predicted from $E_{\mathrm{K\text{-}L}}$ and $E_{\mathrm{K\text{-}R}}$ through a linear model, two statistics are calculated: prediction efficiency (R^2) and error variance (σ^2). R^2, also termed coefficient of determination, is defined as

$$R^2 = 1 - SS_{\mathrm{Res}}/SS_{\mathrm{Total}}. \tag{2.21}$$

Here, SS_{Res}, the residual sum of squares, is defined in terms of the deviations of measurements from a linear model as

$$SS_{\mathrm{Res}} = \|\, \boldsymbol{y} - \hat{\boldsymbol{y}} \,\|^2, \tag{2.22}$$

where $\boldsymbol{y}$ is the vector of observations, $\hat{\boldsymbol{y}}$ is the vector of least-square fits, and $\|\boldsymbol{x}\|$ represents the Euclidean norm of a vector $\boldsymbol{x}$. Similarly, SS_{Total}, the total sum of squares, is defined as

$$SS_{\text{Total}} = \| \boldsymbol{y} - \bar{y}\mathbf{1} \|^2, \tag{2.23}$$

where $\bar{y}$ is the sample mean, and $\mathbf{1}$ is given by $\mathbf{1} = (1, \ldots, 1)^{\mathrm{T}}$. R^2, which takes values between 0 and 1, i.e.,

$$R^2 \in [0, 1], \tag{2.24}$$

represents the proportion of variation in the dependent variable that is explained by the model. For example, a value such as $R^2 = 0.7$ can be interpreted as meaning: "Approximately 70% of the variation in the dependent variable can be explained by the assumed independent variables. The remaining 30% must be explained by unknown variables or inherent variability" [*Myers*, 2000]. In a linear regression analysis, which is the model that is employed here, R^2 is the square of the correlation coefficient (ρ). Although statistically only R^2 of the variation can be attributed to the independent variables tested, in this study, $R^2 \geq 0.5$ is taken to indicate adequacy of fit. The criterion is a weak one, but the majority of the cases (33 of 53) satisfy the stronger criterion $R^2 \geq 0.6$, and 21 of the 53 cases satisfy the criterion $R^2 \geq 0.7$.

The error variance is estimated from the variance of the residuals [*Myers*, 2000], i.e.,

$$\sigma^2 \approx SS_{\text{Res}} / (n - p), \tag{2.25}$$

where n is the number of observations, and p is the number of parameters. For example, for equation (2.41) later used in this paper, $p = 3$. For the event of 20 November 2003, the results are shown in Figure 2.2.

Because the magnitudes of the independent variables can be quite different, it is helpful to normalize them so they all have similar ranges. The weighting of the normalized independent

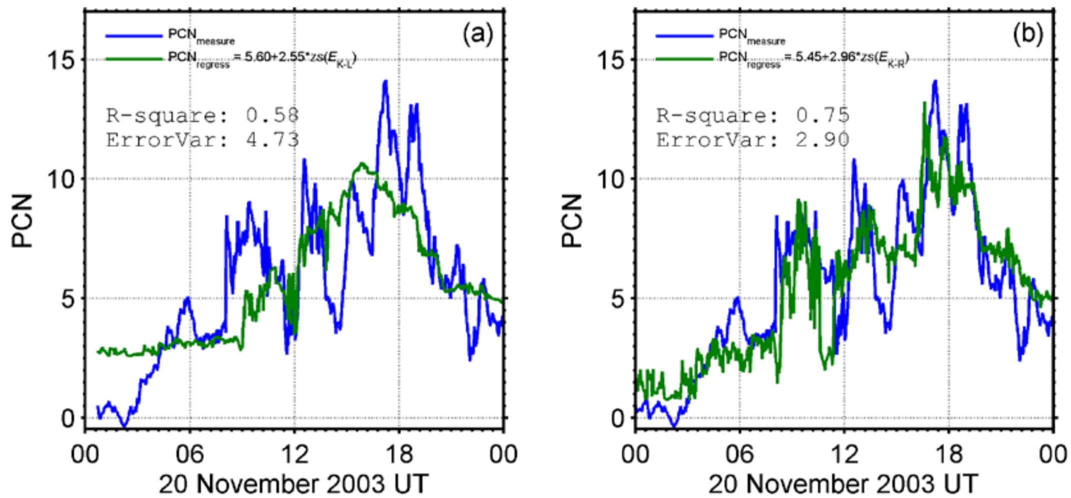

Figure 2.2 Comparison between the measured PCN index and the predicted PCN index based on solar wind parameters for the storm of 20 November 2003. The blue line is the measured PCN index. The green line is the predicted PCN index based on a linear regression from (a) the solar wind merging electric field ($E_{\text{K-L}}$); (b) the electric field of *Kivelson and Ridley* [2008] ($E_{\text{K-R}}$). Additional time shifts have been added to the propagated solar wind data to achieve the highest correlation between the PCN index and $E_{\text{K-L}}$ and between the PCN index and $E_{\text{K-R}}$ respectively. R^2 and error variance are calculated to estimate the goodness of fit. Reproduced by permission of American Geophysical Union from *Gao et al.* [2012c].

variable can then represent its importance. The normalization is achieved through replacement of the variable X with mean μ_X and standard deviation σ_X by its z-score, which is specified as,

$$zs(X) = (X - \mu_X) / \sigma_X . \tag{2.26}$$

The normalized quantity has expectation 0 and standard deviation 1. For example, in Figure 2.2 (a), the relation between the PCN index and $zs(E_{\text{K-L}})$ is summarized as

$$\text{PCN} = 5.60 + 2.55zs(E_{\text{K-L}}) + \varepsilon_{\text{K-L}}. \tag{2.27}$$

For a normalized independent variable, the regression coefficient indicates the weight of this factor. Thus, if multiple independent variables contribute to the PCN index, a direct comparison

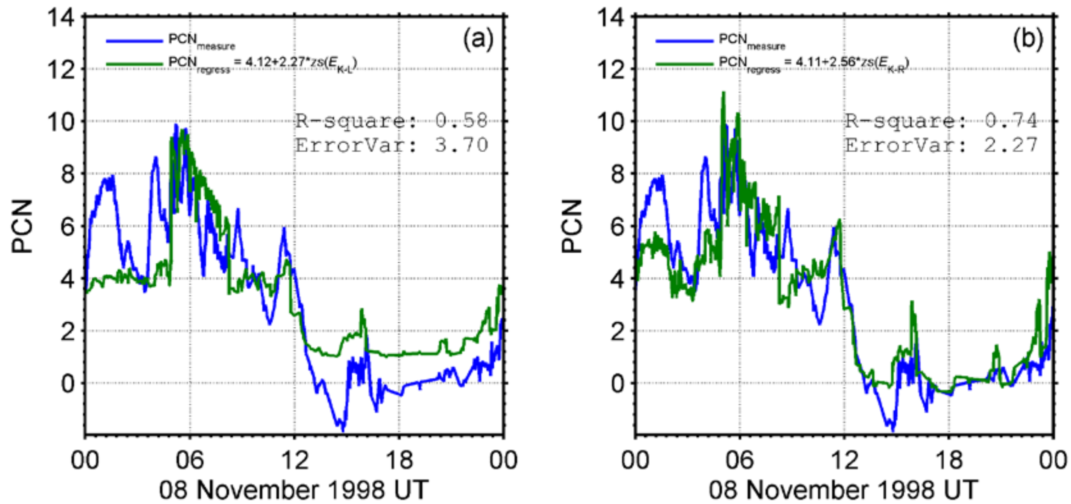

Figure 2.3 As in Figure 2.2 for a different event on 8 November 1998. Reproduced by permission of American Geophysical Union from *Gao et al.* [2012c].

of regression coefficients linking the PCN index and the corresponding z-score representations reveals the relative importance among all the independent variables. In Figure 2.2 (b), such a relation between the PCN index and $E_{\text{K-R}}$ yields

$$\text{PCN} = 5.45 + 2.96zs(E_{\text{K-R}}) + \varepsilon_{\text{K-R}}. \tag{2.28}$$

R^2 and error variance have been calculated for both $E_{\text{K-L}}$ and $E_{\text{K-R}}$. The PCN inferred from $E_{\text{K-R}}$ corresponds more closely to the measured PCN index (Figure 2.2 (b)) than does the PCN index predicted from $E_{\text{K-L}}$ (Figure 2.2 (a)). A direct comparison of the regression coefficient between the PCN index and $E_{\text{K-R}}$ (2.96) with that between the PCN index and $E_{\text{K-L}}$ (2.55) supports the stronger predictability of the PCN index from $E_{\text{K-R}}$, which is further confirmed by R^2 and error variance. R^2 is significantly higher for $E_{\text{K-R}}$ (0.75) than for $E_{\text{K-L}}$ (0.58), while the error variance for $E_{\text{K-R}}$ (2.90) is significantly lower than for $E_{\text{K-L}}$ (4.73).

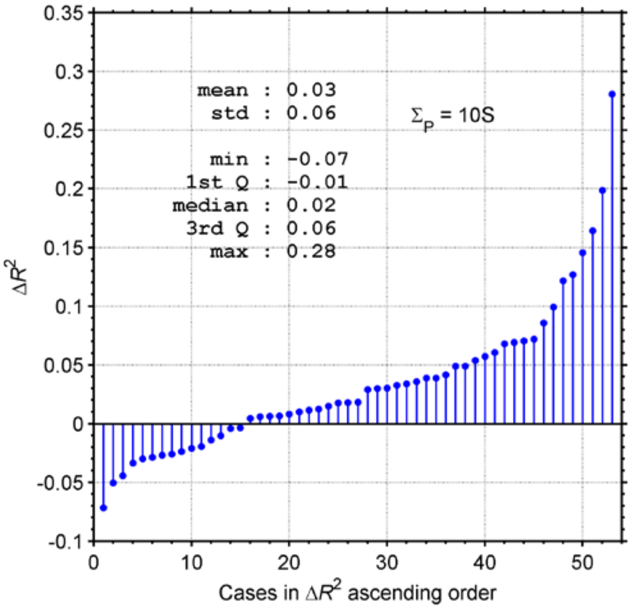

Figure 2.4 The difference of R^2 (i.e. ΔR^2 defined in equation (2.29)) when $E_{\text{K-R}}$ is evaluated for Σ_P = 10 S for all the 53 cases. The summary statistics are: mean, 0.03; standard deviation, 0.06; minimum, –0.07; 1st quartile, –0.01; median, 0.02; 3rd quartile, 0.06; maximum, 0.28. Cases are arranged in such an order that ΔR^2 increases from left to right. Positive values indicate that by switching from $E_{\text{K-L}}$ to $E_{\text{K-R}}$, the consistency between the measured PCN index and the predicted PCN index is improved. Negative values mean otherwise. Reproduced by permission of American Geophysical Union from *Gao et al.* [2012c].

Figure 2.3 shows another event on 8 November 1998, and again the estimates of the quality of the prediction favor $E_{\text{K-R}}$. When $E_{\text{K-L}}$ is significantly different from $E_{\text{K-R}}$, the PCN indices predicted from $E_{\text{K-L}}$ and $E_{\text{K-R}}$ differ considerably. However, most of the time, the difference between the $E_{\text{K-L}}$ and $E_{\text{K-R}}$ is not significant, because for typical solar wind properties, the factor multiplying $E_{\text{K-L}}$ in equation (2.11) is close to 1. Consequently, most of the time, there is an insignificant improvement in changing the basis of prediction from $E_{\text{K-L}}$ to $E_{\text{K-R}}$.

For clarity, I explicitly define ΔR^2 as,

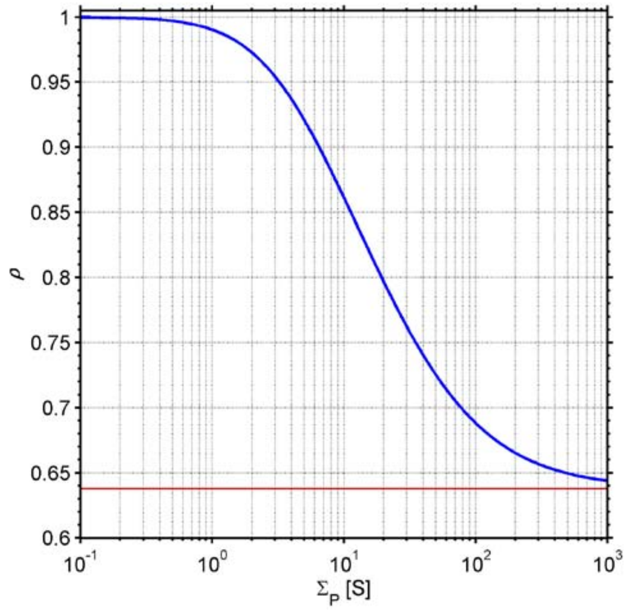

Figure 2.5 The correlation coefficient between $E_{K\text{-}L}$ and $E_{K\text{-}R}$ (i.e. ρ defined in equation (2.31)) on 20 November 2003 when $E_{K\text{-}R}$ is evaluated with different values of Σ_P. The red line represents the limit of ρ as Σ_P approaches ∞. The X axis is logarithmic. Reproduced by permission of American Geophysical Union from *Gao et al.* [2012c].

$$\Delta R^2 = R^2 \text{ of equation (2.20)} - R^2 \text{ of equation (2.19)}. \quad (2.29)$$

Figure 2.4 displays ΔR^2 for 53 cases in ΔR^2 ascending order. Positive values of ΔR^2 indicate improvement by switching from $E_{K\text{-}L}$ to $E_{K\text{-}R}$ as independent variable, while negative values mean poorer predictions. R^2 increases by using $E_{K\text{-}R}$ as an independent variable with a few exceptions. Furthermore, the typical negative values are small compared to most of the positive values.

2.2.2 The influence of Pedersen conductance, Σ_P

In equation (2.11), Σ_P is an important parameter in determining $E_{K\text{-}R}$, but it cannot be precisely estimated. Thus, it is necessary to test the sensitivity of the results to the assumed value of Σ_P (10

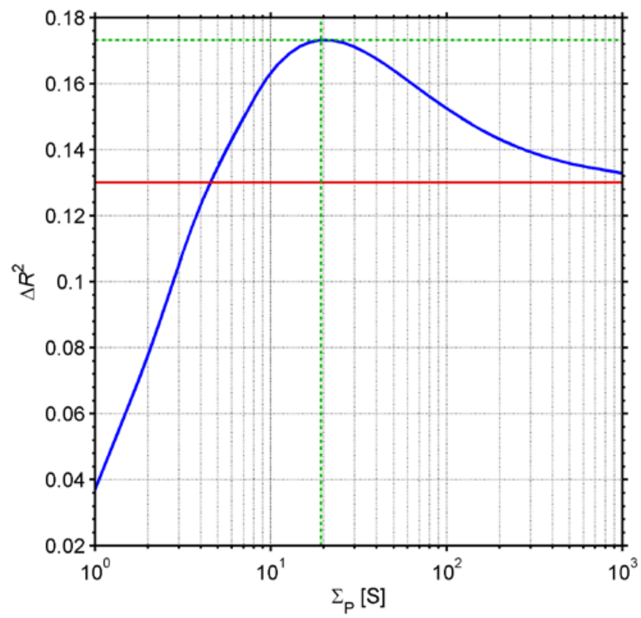

Figure 2.6 Change of R^2 (i.e. ΔR^2 defined in equation (2.29)) on 20 November 2003 when $E_{K\text{-}R}$ is evaluated with different values of Σ_P. The blue line represents ΔR^2 as a function of Σ_P. The red line represents the asymptotic value for infinite conductance, i.e. $\Delta R^2(\infty)$. The green line gives the maximum value of ΔR^2 and the corresponding Σ_P of 20 S. The X axis is logarithmic. Reproduced by permission of American Geophysical Union from *Gao et al.* [2012c].

S). If Σ_P is allowed to take values continuously from 0 to∞, then $E_{K\text{-}R}$ becomes a function of Σ_P, i.e.,

$$E_{K\text{-}R} = E_{K\text{-}R}(\Sigma_P), \text{ where } \Sigma_P \in [0, \infty). \tag{2.30}$$

I first notice that the similarity between $E_{K\text{-}L}$ and $E_{K\text{-}R}$, as measured by their correlation coefficient (ρ), i.e.,

$$\rho(\Sigma_P) = \rho(E_{K\text{-}L}, E_{K\text{-}R}(\Sigma_P)), \tag{2.31}$$

decreases as Σ_P increases. This can be partly verified by examining the values of ρ at $\Sigma_P = 0$ and when Σ_P approaches ∞. At $\Sigma_P = 0$, since $E_{K\text{-}R}(0) = 2E_{K\text{-}L}$, $\rho(0) = 1$. When Σ_P is very large, i.e. Σ_P

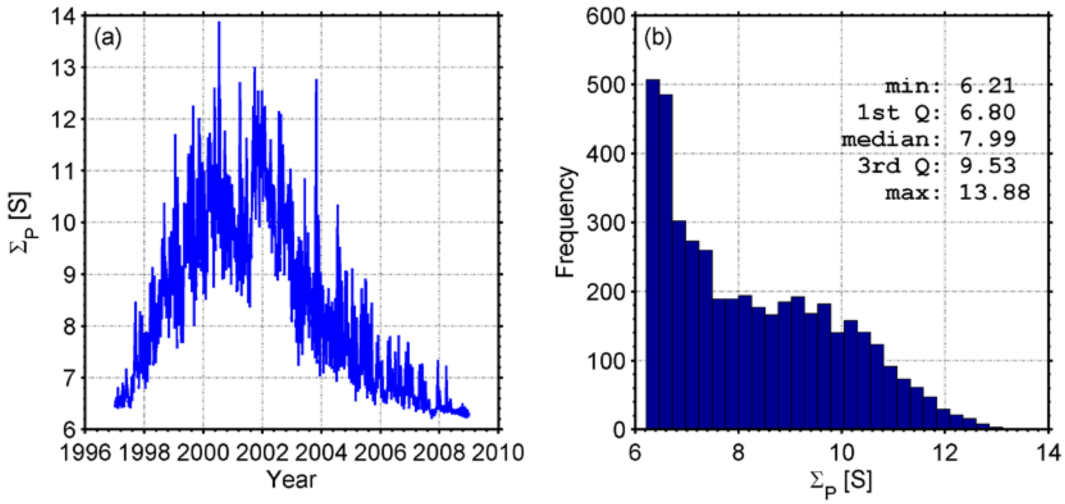

Figure 2.7 Ionospheric Pedersen conductance, Σ_P, computed by using equation (2.33) with C_0 = 0.77. (a) Time series of Σ_P from 1 January 1997 to 31 December 2009. (b) The histogram of Σ_P from 1 January 1997 to 31 December 2009 with summary statistics: minimum, 6.21; first quartile, 6.80; median, 7.99; third quartile, 9.53; maximum, 13.88. Reproduced by permission of American Geophysical Union from *Gao et al.* [2012c].

$\gg \Sigma_A$, since $E_{K\text{-}R} \approx E_{K\text{-}L} 2\Sigma_A/\Sigma_P$, which, apart from constant coefficient $2/\Sigma_P$, is equivalent to $E_{K\text{-}L}\Sigma_A$, the coefficient becomes

$$\rho \approx \rho(E_{K\text{-}L}, E_{K\text{-}L}\Sigma_A), \text{ when } \Sigma_P \gg \Sigma_A. \tag{2.32}$$

This value of ρ is expected to be smaller than 1. An example of ρ varying as a function of Σ_P on 20 November 2003 is shown in Figure 2.5. In the range of probable conductance near 10 S, the correlation coefficient between $E_{K\text{-}L}$ and $E_{K\text{-}R}$ is 0.92, 0.86, and 0.72 when Σ_P is 5 S, 10 S, and 15 S respectively.

Unlike $\rho(\Sigma_P)$, ΔR^2 (equation (2.29)), also taken as a function of Σ_P, i.e. $\Delta R^2(\Sigma_P)$, need not change monotonically with Σ_P. An example, again for the case of 20 November 2003, is shown in Figure 2.6. The blue line represents ΔR^2 as a function of Σ_P. The green line identifies the

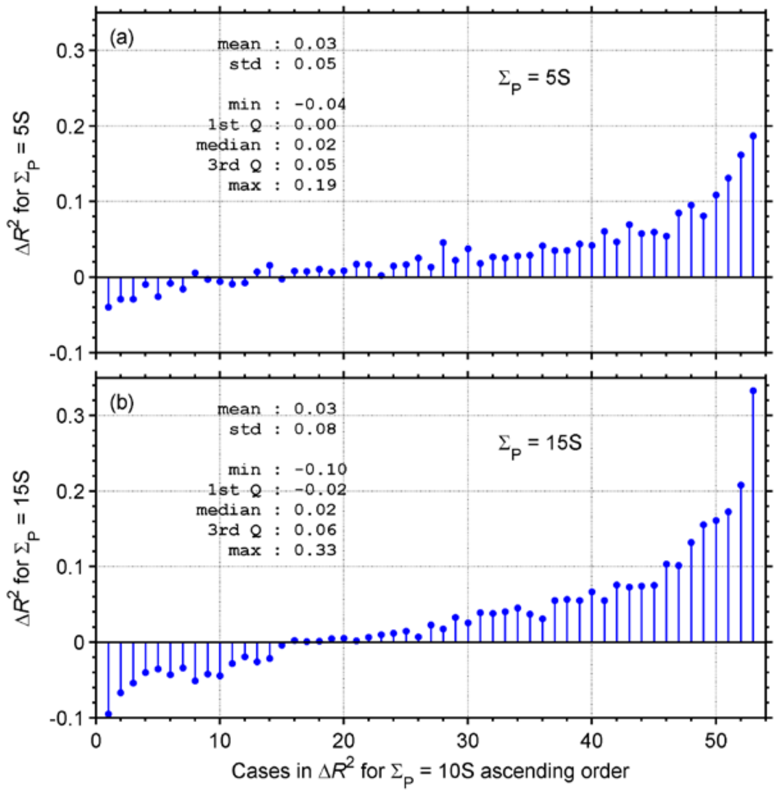

Figure 2.8 As for Figure 2.4 for Σ_P = 5 S (top) and 15 S (bottom). The change of R^2 (equation (2.29)) for Σ_P = 5 S is summarized as: minimum, –0.04; 1st quartile, 0.00; median, 0.02; 3rd quartile, 0.05; maximum, 0.19. For Σ_P = 15 S, the change of R^2 is summarized as: minimum, -0.10; 1st quartile, –0.02; median, 0.02; 3rd quartile, 0.06; maximum, 0.33. In both panels, cases are in the same order as that of Figure 2.4. Reproduced by permission of American Geophysical Union from *Gao et al.* [2012c].

maximum ΔR^2, which is 0.175 for Σ_P of 20 S. Although not shown, $\Delta R^2(0) = 0$. As Σ_P approaches ∞, ΔR^2 represents the change of R^2 by switching from $E_{K\text{-}L}$ to $E_{K\text{-}L}\Sigma_A$, which is shown with the red line. As can be seen from Figure 2.6, ΔR^2 varies over a fairly large range for $\Sigma_P \in [0, \infty)$. However, in reality, Σ_P varies over a small range compared to $[0, \infty)$. Thus, in the following analysis, I concentrate on a subset of $[0, \infty)$ containing only reasonable values of Σ_P.

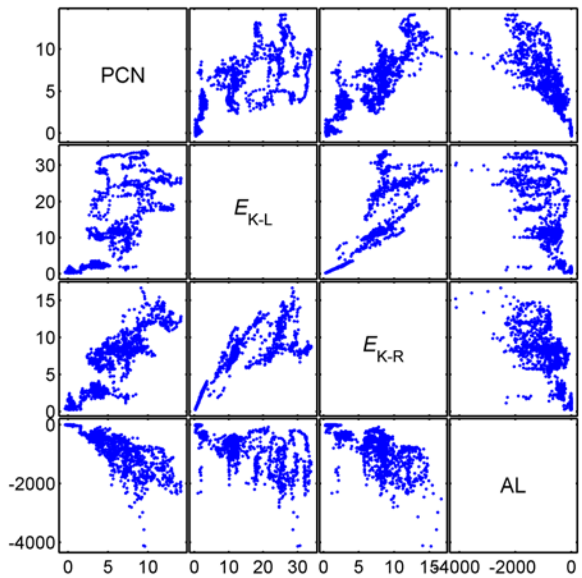

Figure 2.9 Scatter plot matrix between the measured PCN index, $E_{K\text{-}L}$, $E_{K\text{-}R}$, and the AL index on 20 November 2003. The PCN index is the ordinate of all the plots in 1st row and the abscissa of all the plots in 1st column, etc. Reproduced by permission of American Geophysical Union from *Gao et al.* [2012c].

In order to estimate the range of interest, I use the formula of *Robinson and Vondrak* [1984] which expresses the Pedersen conductance caused by solar illumination as

$$\Sigma_P = C_0 (F_{10.7})^{1/2}, \tag{2.33}$$

where $F_{10.7}$ represents the strength of 10.7cm solar radio flux at Earth and, as recommended by *Ober et al.* [2003],

$$C_0 = 0.77. \tag{2.34}$$

The resulting time series of Σ_P with 1-day resolution from 1 January 1997 to 31 December 2009 is shown in Figure 2.7 (a). The corresponding histogram is displayed in Figure 2.7 (b). From Figure 2.7, all of the values lay between 5 S and 15 S, i.e. $\Sigma_P \in [5\text{ S}, 15\text{ S}]$. By assuming $\Sigma_P = 5$ S

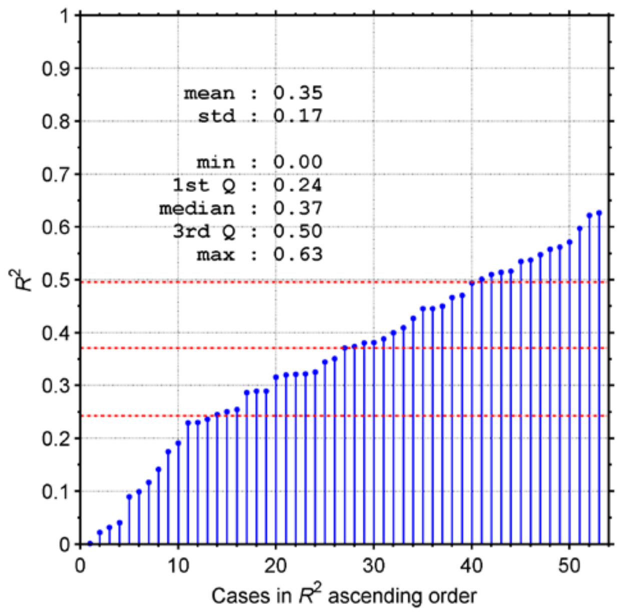

Figure 2.10 The driven component of AL for the 53 cases estimated through the R^2 of regression between AL and $E_{\text{K-R}}$, i.e. R^2 of equation (2.38), in R^2 ascending order. The summary statistics are: minimum, 0.00; 1st quartile, 0.24; median, 0.37; 3rd quartile, 0.50; maximum, 0.63. The mean is 0.35. The red dashed lines are 1st quartile, median and 3rd quartile from bottom to top. Reproduced by permission of American Geophysical Union from *Gao et al.* [2012c].

and 15 S, the changes of R^2 by switching from $E_{\text{K-L}}$ to $E_{\text{K-R}}$ as solar wind driver are shown in Figure 2.8 top and bottom respectively. The cases are arranged in the same order as that of Figure 2.4. Compared with Figure 2.4, one can see that if R^2 increases by switching from $E_{\text{K-L}}$ to $E_{\text{K-R}}$ for $\Sigma_P = 10$ S, then it is likely that R^2 increases for $\Sigma_P \in [5\text{ S}, 15\text{ S}]$, although the change of ΔR^2 is usually larger for large Σ_P. Thus, $E_{\text{K-R}}$ seems to serve as a potentially better indicator of the solar wind influence on the ionospheric processes than $E_{\text{K-L}}$, and results are plausible for a reasonable range of realistic values of Σ_P. Furthermore, as suggested by *Kivelson and Ridley* [2008], I take 10 S as a reasonable estimation of Σ_P in this thesis as the predictions appear to be little affected by the specific value used in the analysis.

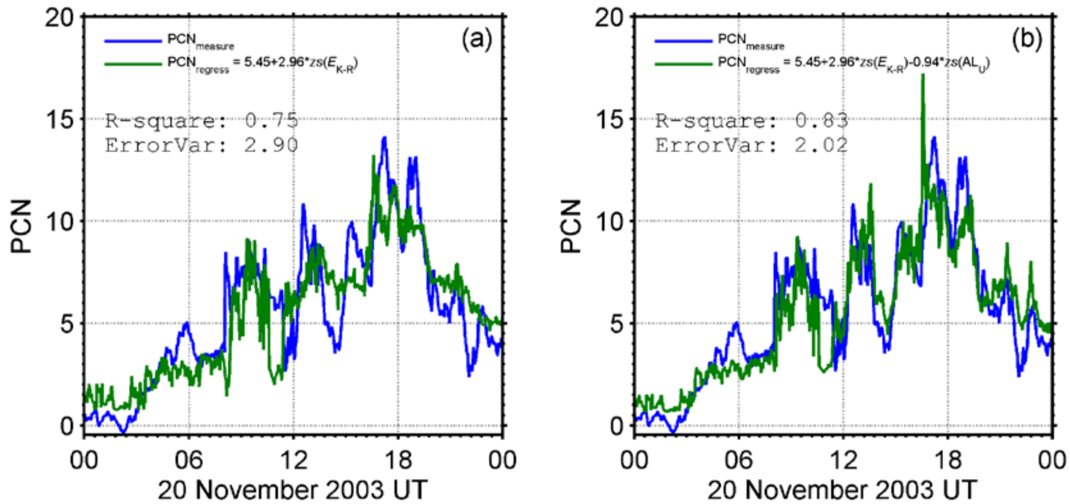

Figure 2.11. The same day as that plotted in Figure 2.2 (20 November 2003) (a) without dependence on the AL_U index, (b) with dependence on the AL_U index. The blue lines are the measured PCN index and the green lines are the predicted PCN index. Additional time shift has been added to the propagated solar wind data to achieve the highest correlation between the PCN index and $E_{K\text{-}R}$. Reproduced by permission of American Geophysical Union from *Gao et al.* [2012c].

2.2.3 Internal driving of the polar cap dynamics

The PCN index is a measure of the magnetic field perturbation at Qaanaaq caused by ionospheric plasma flows [*Troshichev et al.*, 1988], and plasma flows can be initialized by external driving, e.g. low-latitude magnetopause reconnection or viscous interactions between the solar wind and magnetosphere at the low-latitude boundary layer [e.g., *Axford*, 1964], and internal driving, e.g. magnetotail energy release, such as substorms. Here, I pay primary attention to dayside reconnection and substorm activity, while treating other sources as unexplained errors. According to the principle of superposition, I linearly combine these sources and get

$$\delta B = \delta B_D + \delta B_U + \delta B_O, \tag{2.35}$$

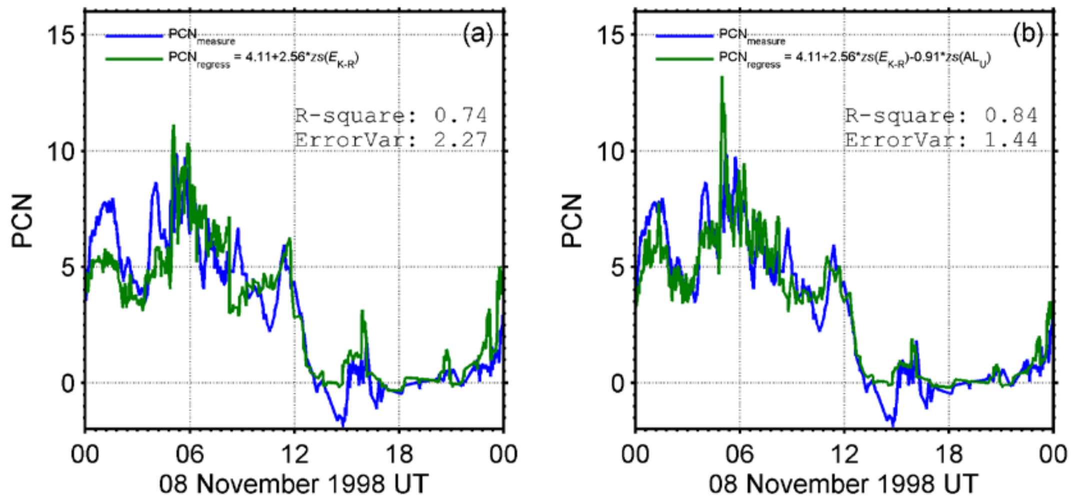

Figure 2.12. As in Figure 2.11 for a different event on 8 November 1998 (also in Figure 2.3). Reproduced by permission of American Geophysical Union from *Gao et al.* [2012c].

where δB_{D} is the magnetic field perturbation at Qaanaaq directly driven by dayside reconnection, δB_{U} is the magnetic field perturbation at Qaanaaq arising from the energy unloading in the magnetotail, and δB_{O} represents the other contributions to the magnetic field perturbations at Qaanaaq. Here, δB_{O} is attributed to unexplained error. So the equation is reduced to

$$\delta B \approx \delta B_{\mathrm{D}} + \delta B_{\mathrm{U}} \,. \tag{2.36}$$

While this greatly simplifies the analysis, it leaves opportunities for improvement in future studies that can consider other sources that can be precisely identified and reasonably modeled. I use $E_{\mathrm{K\text{-}R}}$ to represent the driving of the solar wind. Thus, as a first order approximation, a linear dependence between δB_{D} and $E_{\mathrm{K\text{-}R}}$ is assumed, i.e.,

$$\delta B_{\mathrm{D}} \propto E_{\mathrm{K\text{-}R}}. \tag{2.37}$$

Following *McPherron and Baker* [1993], I use the AL index to represent the contribution of nightside energy release. Figure 2.9 shows scatter plots among the PCN index, $E_{\mathrm{K\text{-}L}}$, $E_{\mathrm{K\text{-}R}}$ and

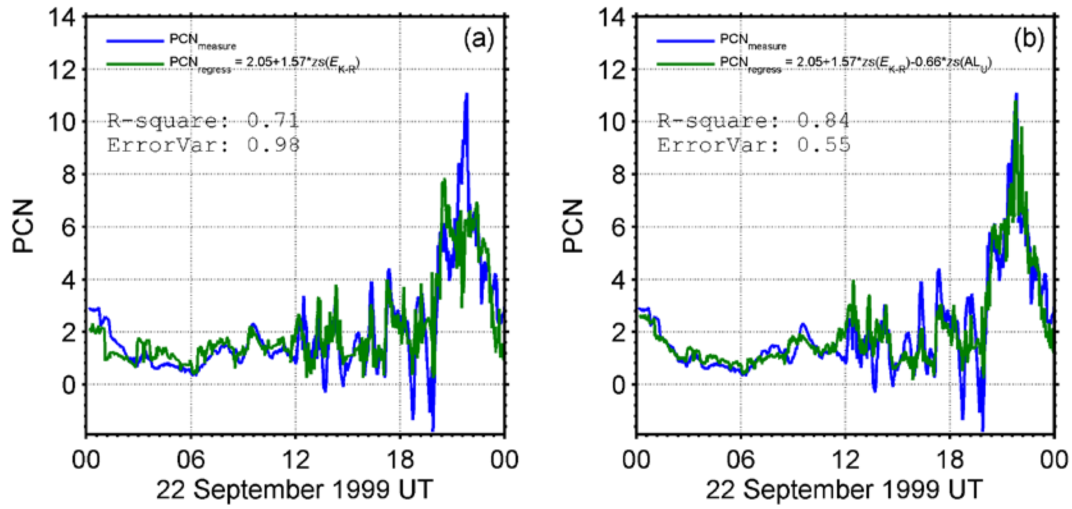

Figure 2.13. As in Figure 2.11 for a different event on 22 September 1999. Reproduced by permission of American Geophysical Union from *Gao et al.* [2012c].

the AL index on 20 November 2003 in a matrix form. For example, the 1st row 2nd column is a scatter plot of $E_{K\text{-}L}$ and the PCN index. The better correlation between the PCN index and $E_{K\text{-}R}$ than between the PCN index and $E_{K\text{-}L}$ is evident in row 1 that shows smaller scatter in column 3 than in column 2. This is further confirmed by the better consistency between the original and the flipped scatter plots, i.e. the PCN index versus $E_{K\text{-}R}$, (row 1, column 3) and $E_{K\text{-}R}$ versus the PCN index (row 3, column 1) than the pair between the PCN index and $E_{K\text{-}L}$. Similarly, a better correlation between $E_{K\text{-}R}$ and AL than between $E_{K\text{-}L}$ and AL can be found by comparing row 4 columns 3 and 2. A good correlation between the PCN index and AL (row 4 column 1) is consistent with the choice of AL index as an independent variable when predicting the PCN index from nightside processes.

As the intention is to identify the effects of activity initiated on the nightside of the magnetosphere, it is desirable to remove the portion of AL that responds directly to the solar

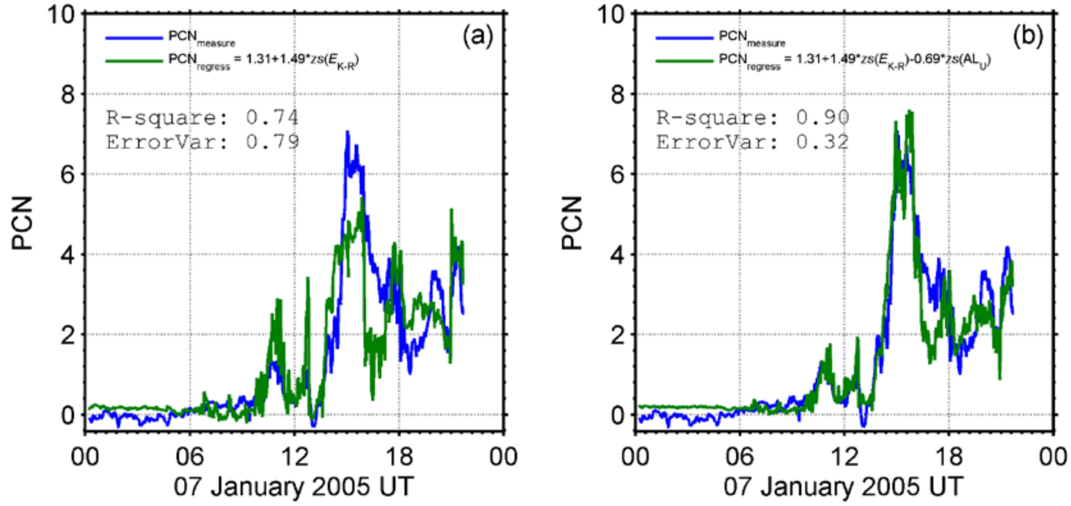

Figure 2.14. As in Figure 2.11 for a different event on 7 January 2005. Reproduced by permission of American Geophysical Union from *Gao et al.* [2012c].

wind input. For this reason, I introduce an unloading AL index, AL_U, defined as follows. I run a regression analysis with AL as the dependent variable and $E_{K\text{-}R}$ as the independent variable for the events to obtain the directly driven portion of AL, which I define as

$$AL_D = \alpha_0 + \alpha_1 E_{K\text{-}R}, \tag{2.38}$$

where α_0 and α_1 are regression coefficients. The driven portion of AL is estimated through the R^2 of equation (2.38) and is shown in Figure 2.10. On average AL_D contributes 35% of AL for the 53 cases. Then I subtract AL_D from AL to get AL_U, a quantity that is dominated by magnetotail activity [*Akasofu*, 1979a; *McPherron and Baker*, 1993]. Here

$$AL_U = AL - AL_D, \tag{2.39}$$

and, similar to $E_{K\text{-}R}$, a first order approximation is assumed, i.e.,

$$\delta B_U \propto AL_U. \tag{2.40}$$

A linear regression model that includes both the influence of direct solar wind driving and the influence of nightside energy release on the PCN index can be expressed in terms of the z-score of the two variables in the form

$$\mathrm{PCN} = \beta_0 + \beta_1 zs(E_{\mathrm{K\text{-}R}}) + \beta_2\, zs(\mathrm{AL_U}) + \varepsilon, \tag{2.41}$$

where β_0, β_1 and β_2 are regression coefficients, and ε is assumed to be Gaussian noise. Note that, in equation (2.41), I use only the portion of the AL index that remains after the effects of $E_{\mathrm{K\text{-}R}}$ are removed.

Usually, regression is used to investigate the association of the independent variables and the dependent variable. In the framework of a magnetospheric convection model, the associations between $E_{\mathrm{K\text{-}R}}$ and the PCN index and between $\mathrm{AL_U}$ and the PCN index imply causation ($E_{\mathrm{K\text{-}R}}$ drives ionospheric flows that partially control the PCN index and $\mathrm{AL_U}$ drives flows that partially control the PCN index). For the purpose of establishing the relative importance of the two controlling factors, it is essential to make $E_{\mathrm{K\text{-}R}}$ and $\mathrm{AL_U}$ dimensionless by replacing them with their corresponding z-scores (equation (2.26)) as I have done. Figure 2.11 shows the effect of the AL index on the prediction of the PCN index for the day plotted in Figure 2.2 (20 November 2003). Figure 2.11 (a) compares the measured PCN index with the predicted PCN index using $E_{\mathrm{K\text{-}R}}$ to represent the contributions directly driven by the solar wind. In Figure 2.11 (b), I use the formulation of equation (2.41) including both $E_{\mathrm{K\text{-}R}}$ and $\mathrm{AL_U}$ as independent variables and find that it improves the consistency between observation and regression, especially at high levels of geomagnetic activity. The addition of a dependence on $\mathrm{AL_U}$ increases R^2 from 0.75 to 0.83 and reduces the error variance from 2.90 to 2.02. Figure 2.12, Figure 2.13 and Figure 2.14 apply the same type of analysis to another three cases on 8 November 1998, 22 September 1999 and 7 January 2005. In all cases, it is apparent from the plots that by including a

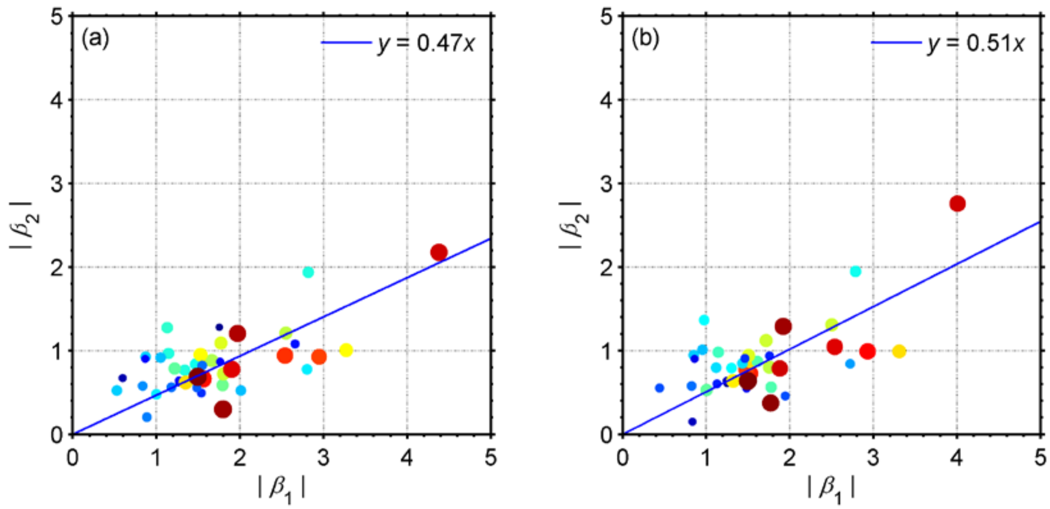

Figure 2.15. (a) Scatter plot of regression coefficient of AL_U versus regression coefficient of $E_{K\text{-}R}$ for the events with $R^2 \geq 0.5$. The points are both sized and colored according to their R^2 values. The blue line through the origin is an orthogonal least-square fit to the points. (b) As in Figure 2.15 (a) except that an extra 10 minutes time delay is added to $E_{K\text{-}R}$ when computing AL_U by using equation (2.38). Reproduced by permission of American Geophysical Union from *Gao et al.* [2012c].

dependence on AL_U, the predictions are improved, especially for PCN > 5. In the additional three cases illustrated, the R^2 increases (0.74 to 0.84, 0.71 to 0.84, and 0.74 to 0.90) and the error variance decreases (2.27 to 1.44, 0.98 to 0.55, and 0.79 to 0.32) significantly when AL_U is added as an independent variable.

Although nightside processes contribute to the PCN index, effects directly driven by dayside reconnection are more important. Since both $E_{K\text{-}R}$ and AL_U are normalized by representing them in terms of their z-scores, a direct comparison of the regression coefficients can reveal their relative contributions to the PCN index. Figure 2.15 (a) shows a scatter plot between the regression coefficients of $E_{K\text{-}R}$ and AL_U for the events with $R^2 \geq 0.5$. The points

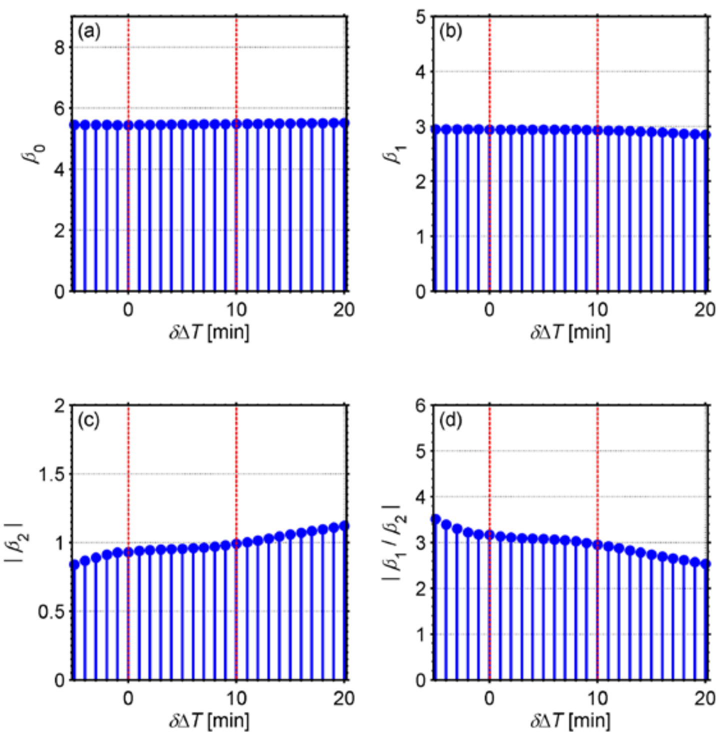

Figure 2.16. Variations of (a) β_0, (b) β_1, (c) β_2, and (d) $|\beta_1 / \beta_2|$ with $\delta\Delta T$ for the case of 20 November 2003. The red dashed lines label $\delta\Delta T = 0$ and 10 minutes in each panel. Reproduced by permission of American Geophysical Union from *Gao et al.* [2012c].

have been sized and colored according to their R^2 values. If the two input parameters contributed equally to the fit, the points would lie close to the line $y = x$. An orthogonal least squares fit through the origin whose slope reveals the relative magnitudes of β_1 and β_2, i.e. $|\beta_2 / \beta_1|$, gives

$$y = 0.47x, \tag{2.42}$$

indicating that, on average,

$$|\beta_1| \approx 2\,|\beta_2|. \tag{2.43}$$

In other words, the directly driven dayside contribution dominates the PCN index by roughly 2:1. This ratio has been confirmed by applying the same analysis to the PCS index.

As stated in section 2.3.1, in equation (2.41), $E_{\text{K-R}}$ is calculated by using the propagated solar wind data with extra time shifts to achieve maximum correlation between $E_{\text{K-R}}$ and the PCN index. In addition, I use the same $E_{\text{K-R}}$ in equation (2.38) to derive AL_{U}. In principle, time delays between AL and $E_{\text{K-R}}$ should also be taken into account. *Bargatze et al.* [1985] studied the temporal relationship between the solar wind and magnetospheric activity by constructing a linear prediction filter between vB_s [*Burton et al.*, 1975] and the AL index, where v is the solar wind bulk velocity and B_s is related to IMF B_Z through

$$B_s = -B_Z \text{ for } B_Z < 0, \text{ and } B_s = 0 \text{ for } B_Z \geq 0. \tag{2.44}$$

Using IMP 8 solar wind data propagated to $X_{\text{GSM}} = 15R_E$, they found that the filters were composed of two response pulses peaking at time lags 20 and 60 minutes, and interpreted the 20 minutes pulse as magnetospheric activity directly driven by the solar wind and the 60 minutes pulse as the response of magnetospheric activity to energy unloading in the magnetotail. Following the analysis of *Bargatze et al.* [1985], in order to remove the directly driven component from the AL index, a time delay close to 20 minutes needs to be added to the propagated solar wind data. Recall that, for each case, I add a time lag, typically 12 minutes, to the solar wind data to achieve the highest correlation between the PCN index and $E_{\text{K-R}}$. Thus, an additional time delay close to 8 minutes should be added to $E_{\text{K-R}}$ in equation (2.38). However, with this additional time delay, denoted as $\delta\Delta T$, the results are close to those without it. For example, Figure 2.16 shows the variations of regression coefficients β_0, β_1, and β_2 for the case of 20 November 2003 with $\delta\Delta T$ varying from –5 to 20 minutes. From Figure 2.16, β_0 and β_1 are close to constant for different values of $\delta\Delta T$. β_2 changes from –0.93 to –0.99 when $\delta\Delta T$ varies from 0 to 10 minutes, and to -1.12 when $\delta\Delta T$ is 20 minutes. Consequently, the values of the ratio $|\beta_1/\beta_2|$ are 3.16, 2.96, and 2.54 for $\delta\Delta T$ being 0, 10 and 20 minutes respectively. Thus, although

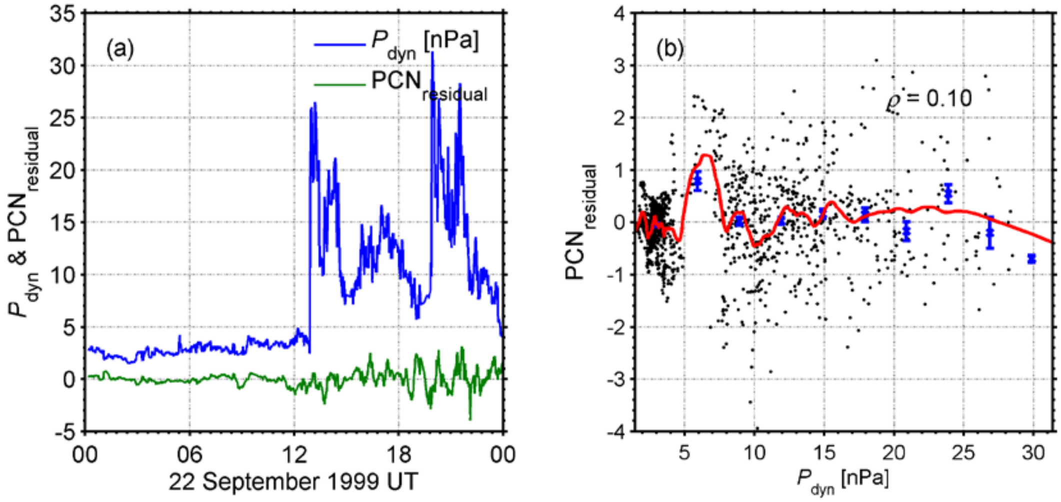

Figure 2.17. (a) A time series plot of the solar wind dynamic pressure p_{dyn} (blue) and the difference of the measured PCN index and the predicted PCN index, i.e. ε in equation (2.41) ($\mathrm{PCN}_{\mathrm{residual}}$ in figure), (green) on 22 September 1999 (also in Figure 2.13). (b) Scatter plot between ε and p_{dyn}. The blue crosses indicate the medians in each 2.5 nPa bins. The error bars indicate the errors of the medians. The red line is a running mean of the scatter plot. The correlation coefficient between p_{dyn} and the residual PCN index for this case is 0.10. Reproduced by permission of American Geophysical Union from *Gao et al.* [2012c].

β_0, β_1 and β_2 vary with $\delta\Delta T$, they change little when $\delta\Delta T$ is close to 10 minutes. In Figure 2.15 (b), I show a scatter plot between β_1 and β_2 with an additional time delay of 10 minutes added to $E_{\mathrm{K\text{-}R}}$ when computing $\mathrm{AL_U}$. It is clear that the sizes and colors of the points in Figure 2.15 (b) are similar to those in Figure 2.15 (a), which indicates that the change of R^2 values are small. In fact, if I define the changes of R^2 as

$$\delta R^2 = R^2 \text{ with additional 10 minutes delay} - R^2 \text{ without delay}, \tag{2.45}$$

then, for the data set, δR^2 is summarized as: minimum, –0.07; 1st quartile, –0.03; median, –0.02; 3rd quartile, –0.06; maximum, 0.04. Thus, by adding additional 10 minutes delay to $E_{\mathrm{K\text{-}R}}$ to compute $\mathrm{AL_U}$, the consistency between the measured PCN index and that predicted from equation (2.41) becomes, on average, slightly worse by 0.02 in terms of R^2. Furthermore, the slope of the fitted line (0.51) is close to that obtained when no extra time delay is added to $E_{\text{K-R}}$ in equation (2.38) (0.47). Thus, the dayside contribution to the PCN index still outweighs the nightside contribution by roughly a factor of 2. In other words, with a time delay close to 10 minutes added to $E_{\text{K-R}}$ in deriving AL_U, the conclusion remains the same. Although the exact timing between AL and $E_{\text{K-R}}$ is very important for understanding the details of magnetospheric convection, the conclusions from the analysis are not sensitive to this parameter. Thus, in the analysis that follows, I do not introduce an additional time delay in correlating $E_{\text{K-R}}$ with AL. However, this important issue should be addressed in future studies.

2.2.4 Solar wind dynamic pressure driving of the polar cap dynamics

It has been argued that the PC index responds linearly to a solar wind dynamic pressure pulse, since the change of p_{dyn} alters the magnetopause currents which couple with the ionospheric currents through the Region-1 field-aligned currents and thus change the PC index [*Stauning and Troshichev*, 2008]. This conclusion has been reached from both case studies [*Lukianova*, 2003] and statistical analysis [*Troshichev et al.*, 2007; *Stauning and Troshichev*, 2008]. *Stauning et al.* [2008] studied the dynamic pressure effect for more typical solar wind conditions and found that the PC index responded little to the stationary solar wind dynamic pressure. *Huang* [2005] argued that, on average, p_{dyn} is a less important contributor to the PC index than the solar wind electric field and substorm activity.

Here, I use a model selection approach to test the influence of solar wind dynamic pressure on the PCN index with the 53 cases. All the cases are with subintervals during which

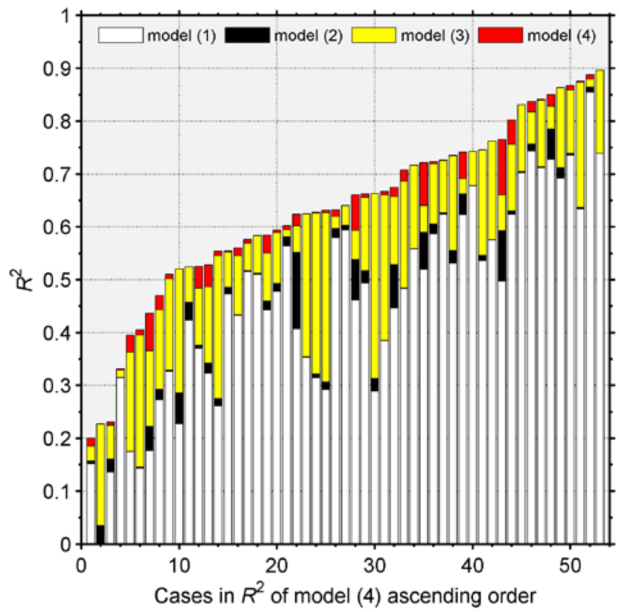

Figure 2.18. R^2 calculated for model (1), (2), (3) and (4). The construction of the plot is described in the text. White bars indicate the values of R^2 for model (1). The visible portions of the black bars are the changes of R^2 resulting from switching from model (1) to model (2). The portions of the yellow and red bars that are visible in the plot show the changes of R^2 obtained by switching from model (2) to model (3) and from model (3) to model (4) respectively. The cases are arranged in such an order that R^2 of model (4) increases from left to right. Reproduced by permission of American Geophysical Union from *Gao et al.* [2012c].

p_{dyn} changed drastically (e.g. Figure 2.17 (a)). I propose four models as potential candidates to relate the PCN index to solar wind parameters and geomagnetic activity,

model (1): PCN = $\beta_0 + \beta_1 E_{K\text{-}R} + \varepsilon_1$;

model (2): PCN = $\beta_0 + \beta_1 E_{K\text{-}R} + \beta_2 p_{dyn} + \varepsilon_2$;

model (3): PCN = $\beta_0 + \beta_1 E_{K\text{-}R} + \beta_2 \mathrm{AL_U} + \varepsilon_3$;

model (4): PCN = $\beta_0 + \beta_1 E_{K\text{-}R} + \beta_2 p_{dyn} + \beta_3 \mathrm{AL_U}^* + \varepsilon_4$.

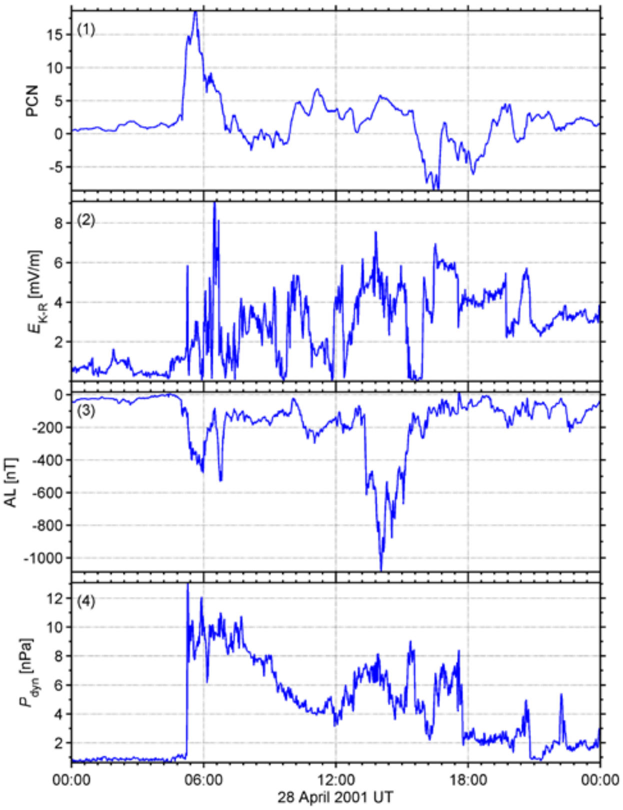

Figure 2.19. The event of 28 April 2001. Plotted are (1) the PCN index; (2) $E_{K\text{-}R}$; (3) the AL index; (4) the solar wind dynamic pressure, p_{dyn}. At around 05:30 UT, p_{dyn} jumped from 2 nPa to 14 nPa. Almost at the same time, the PCN index increased from 2.05 to 13.76. Reproduced by permission of American Geophysical Union from *Gao et al.* [2012c].

In model (3), AL_U is calculated from equations (2.38) and (2.39), while in model (4) AL_U^* is calculated from AL after removing the part that is linearly dependent on both $E_{K\text{-}R}$ and p_{dyn}, i.e.,

$$AL_D^* = \alpha_0 + \alpha_1 E_{K\text{-}R} + \alpha_2 p_{dyn}. \qquad (2.46)$$

Figure 2.18 shows the changes of R^2 when progressing from model (1) to model (4). The figure is created from a bar plot in which I plot R^2 of model (4) in red, thereafter superposing bars of model (3) in yellow, model (2) in black, and model (1) in white. In Figure 2.18, the white bars give the R^2 of model (1) for all the 53 cases. The tops of the black bars that are visible above the white bars are the changes of R^2 resulting from switching from model (1) to model (2). Similarly, the parts of the yellow bars that can be seen above the black bars are the additional changes of R^2 resulting from use of model (3) while the parts of the red bars that appear above the yellow bars are the additional changes from use of model (4). The cases are arranged in such an order that R^2 of model (4) increases from left to right. Referring to the visible portions of the different bars, the white bars are the longest, indicating that $E_{\text{K-R}}$ is the most important factor controlling the PCN index. The second longest are the yellow bars, suggesting that AL_U is also a very important factor. The black bars and the red bars represent the effect of p_{dyn} on the PCN index and are generally much shorter than the white bars and yellow bars, suggesting that p_{dyn} contributes little to the control of the PCN index other than through the density variations already accounted for through $E_{\text{K-R}}$ and that it is far less important than $E_{\text{K-R}}$ and AL_U. Thus, I prefer model (3).

The statistical study of dynamic pressure control of the PCN index shown above can be supplemented by examination of the role of p_{dyn} on a case by case basis. An example on 22 September 1999 is shown in Figure 2.17. In Figure 2.17 (a), the time series of solar wind dynamic pressure and the residual PCN index, i.e. ε in equation (2.41), are plotted versus time. In this case, in which the effect of changing density has been taken into account through its effect on $E_{\text{K-R}}$, there were two jumps of p_{dyn}. At about 13:00 UT, p_{dyn} jumped from 5 nPa to 25 nPa. At around 20:00 UT, p_{dyn} increased from less than 10 nPa to over 30 nPa. The residual PCN index did not respond to the changes of the solar wind dynamic pressure. Figure 2.17 (b) shows a scatter plot between p_{dyn} and the residual PCN index. The correlation coefficient is only 0.10, and no pattern is identified.

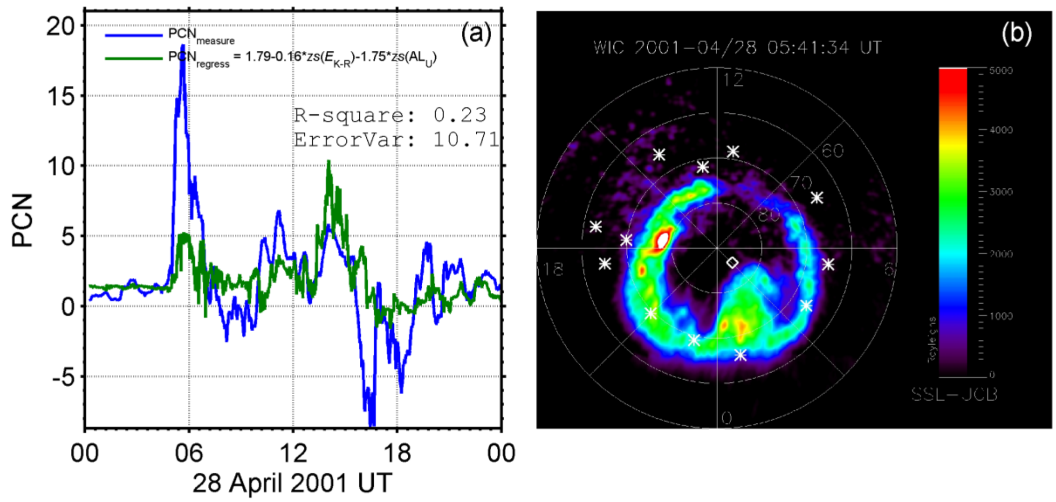

Figure 2.20. The event of 28 April 2001. (a) The measured PCN index (blue) and the predicted PCN index (green); (b) The FUV electron auroral oval from WIC/IMAGE at the time 05:41:34 UT on 28 April 2001. The vertical white line indicates the noon-midnight meridian, while the horizontal white line is the dawn-dusk meridian. The white concentric circles, centered at the magnetic north pole, are magnetic latitudes separated by 10^{o}. The white crosses locate the AE stations. The diamond near the center shows the location of Qaanaaq. Reproduced by permission of American Geophysical Union from *Gao et al.* [2012c].

The data set does include one case in which the PCN index increases concurrently with a jump in p_{dyn} but the model fails to predict the jump. I argue that in this particular case the jump in the PCN index arises because of an unusual excursion of the auroral oval. The event is shown in Figure 2.19. On 28 April 2001, when p_{dyn} jumped from 0.92 nPa to 13.08 nPa at 05:17 UT, the PCN index increased from 2.05 to 13.76 in the following 20 minutes. The model fails to predict the jump of the PCN index (Figure 2.20 (a)). In seeking an explanation of the model's failure, I emphasize first that the PCN index is intended to measure magnetic perturbations on polar cap flux tubes open to the solar wind. A detailed analysis of the aurora using FUV electron data from the Wide-band Imaging Camera (WIC) on the IMAGE satellite [*Mende et al.*, 2000] shows that

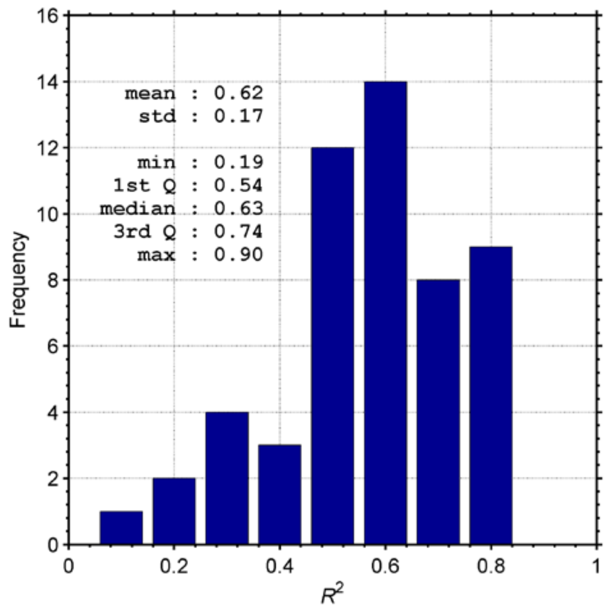

Figure 2.21. Sample distribution of R^2 with $E_{\mathrm{K\text{-}R}}$ and $\mathrm{AL_U}$ as independent variables and the PCN index as dependent variable (equation (2.41)) with summary statistics (mean, 0.62; standard deviation, 0.17; minimum, 0.19; 1st quartile, 0.54; median, 0.63; 3rd quartile, 0.74; maximum, 0.90). Reproduced by permission of American Geophysical Union from *Gao et al*. [2012c].

during the time interval from 05:20 UT to 05:40 UT, the auroral oval expanded unusually far poleward to Qaanaaq shown in Figure 2.20 (b), the auroral electrojet moved to unusually high latitudes and it seems that the PCN index recorded perturbations arising from the auroral electrojet. Because of the extreme excursion of the auroral oval, the Qaanaaq station was no longer a polar cap station measuring dominantly the magnetic perturbations on open field lines. Thus, the jump of the PCN index was dominated by local perturbations that overwhelmed any signal directly imposed from the solar wind. I, therefore, attribute the anomalous coincidence between p_{dyn} and the PCN index to the unusual excursion of the aurora during this particular event and argue that it does not imply control of the PCN index by p_{dyn}.

No clear signature of direct driving of the PCN index by p_{dyn} has been found. I have also tested dp_{dyn}/dt, calculated from differences of consecutive measurements with 1-minute resolution, as an independent variable, but still found no evidence of dynamic pressure control of the PCN index. The fact that correlation between the PCN index and p_{dyn} has been found in previous studies [e.g. *Troshichev et al.*, 2007] can be understood by the following argument. Both $E_{\mathrm{K\text{-}R}}$ and p_{dyn} depend on the solar wind number density (n), i.e.,

$$\Sigma_A \propto n^{1/2} \text{ and } p_{\mathrm{dyn}} \propto n, \tag{2.47}$$

and changes of n result in changes in the PCN index but this effect has been accounted for by the Alfvén conductance incorporated in $E_{\mathrm{K\text{-}R}}$.

2.2.5 Caveats

Figure 2.21 shows the sample distribution of R^2 for $E_{\mathrm{K\text{-}R}}$ and $\mathrm{AL_U}$ as independent variables and the PCN index as dependent variable. Among the cases, I find general consistency between the measured PCN index and the predicted PCN index obtained from the regression analysis with R^2 typically greater than 0.5, but caveats remain. There are various factors that may cause the model to fail to work such as: (1) The PCN index may take on a negative value, but the mechanisms linked to the input parameters that I consider should not produce a negative value of the index. It has been widely accepted that a negative PCN index is caused by locally sunward ionospheric plasma flow resulting from high-latitude magnetopause reconnection [*Nagatsuma*, 2002b]. In the analysis, I consider indices expected to drive large scale anti-sunward convection at high latitudes. Therefore, when there is an interval with negative PCN indices, the value predicted by regression analysis will miss it. For example, in Figure 2.20 (a), the PCN index becomes negative from 15:00 UT to 19:00 UT on 28 April 2001. If I had omitted the data from this time interval, the consistency would have improved. (2) The ionospheric Pedersen conductance Σ_P is crucial to the calculation of $E_{\text{K-R}}$. However, Σ_P can only be roughly estimated. Here, I use a crude value of 10 S. Although I find that the conclusion holds when using the values 5 S and 15 S for Σ_P, in a more complete study, it would be worthwhile to improve the estimate of the ionospheric conductance. (3) I use the propagated solar wind data. The propagation technique is crucial to the solar wind data quality. During a time interval when the propagation fails to work, any prediction is likely to fail. (4) If the auroral oval expands far poleward to Qaanaaq, the station used may approach the boundary of the polar cap (e.g. Figure 2.20 (b)) or even cross it. During such intervals, the electrojet may move far from stations used to evaluate the AL index, and the AL index may no longer be a good indicator of the nightside processes. In addition, the PCN index will be compromised as a measure of magnetic field perturbations on open field lines. Thus such intervals must be removed from any data set used to interpret the processes nominally measured by the PCN index and by the AL index. Unfortunately, owing to limited observations of the aurora, I am able to test only 1 case in which a significant disagreement with the model could be seen to arise because of an anomalous excursion of the auroral electrojet.

2.3 Discussion and conclusions

In this chapter, I investigate the polar cap dynamics influenced by solar wind input and geomagnetic activity by studying the relationship between the PCN index and solar wind parameters and geomagnetic indices. First, I select one to two-day intervals within which cross polar cap potential predicted from the PCN index by using equation (2.8) exceeds 150 kV. I identify 53 cases from 1998 to 2006 for further study. Then I examine the correlation between the PCN index and various solar wind-magnetosphere coupling functions. I find that $E_{\text{K-R}}$, a form representative of the electric field imposed on the ionosphere by low-latitude magnetopause reconnection that takes saturation into account, serves as a potentially better indicator of the dayside contribution to the polar cap than any previously proposed coupling function between the solar wind and magnetosphere including $E_{\text{K-L}}$ during intervals of high geomagnetic activity. An important parameter in determining $E_{\text{K-R}}$ is the ionospheric Pedersen conductance which can only be poorly estimated. I fix Σ_P at 10 S. To test the sensitivity of the conclusion to different values of Σ_P, I perform the same analysis when Σ_P varies within a reasonable range from 5 S to 15 S. I find that, for a given case, if the PCN index correlates with $E_{\text{K-R}}$ better than with $E_{\text{K-L}}$ for $\Sigma_P = 10$ S, then the same conclusion is achieved for $\Sigma_P \in [5\text{ S}, 15\text{ S}]$, although the improvements, measured by the increase of R^2, by switching from $E_{\text{K-L}}$ to $E_{\text{K-R}}$ is usually larger when Σ_P takes on a larger value.

Taking AL_U (equation (2.39)) as an indicator of the effects of nightside geomagnetic activity not directly driven by the solar wind electric field, I demonstrate that the PCN index is responsive to that source as well as the solar wind source. The consistency of the measured PCN index and the PCN index predicted from the regression analysis is found to be improved significantly by introducing contributions from AL_U, the part of AL not directly driven. I find that the directly driven part of AL, i.e. AL_D, can explain, on average, 35% of the variation of the AL index, leaving the rest, 65%, controlled by magnetotail activity. Although generally the contribution to the PCN index from AL_U is less important than the contribution from $E_{\text{K-R}}$ in the sense that the regression coefficient of AL_U is smaller than that of $E_{\text{K-R}}$ by a factor of two, they are comparable in magnitude.

I also explore the relationship between the PCN index and the solar wind dynamic pressure. I do not find a clear signature of a direct response of the PCN index to p_{dyn} or jumps in

p_{dyn}, if the effect of changing density is modeled by $E_{\mathrm{K\text{-}R}}$. One case shows a coincidence between jumps of the PCN index and p_{dyn}, but I argue that during this interval the station used for determination of the PCN index was not located well within the polar cap because the auroral oval expanded exceptionally far poleward.

Eventually, I arrive at the model relating the PCN index to solar wind driving ($E_{\mathrm{K\text{-}R}}$) and magnetotail energy unloading ($\mathrm{AL_U}$), i.e. equation (2.41), which is rewritten here for emphasis,

$$\mathrm{PCN} = \beta_0 + \beta_1 zs(E_{\mathrm{K\text{-}R}}) + \beta_2 zs(\mathrm{AL_U}) + \varepsilon. \tag{2.48}$$

Since the PCN index is measured from only one station for each hemisphere, it cannot give information on the entire polar cap. Nevertheless, the generality of the PCN index is justified by its high correlation to other ionospheric quantities, e.g. cross polar cap potential, Joule heating rate, etc. Thus, similar conclusions are expected if the polar cap dynamics are measured more globally.

CHAPTER 3

Linearity between PCN, $\boldsymbol{E}_{\mathbf{K\text{-}R}}$, and $\mathbf{AL_U}$

3.1 Introduction

In Chapter 2, I constructed a linear model to relate polar cap dynamics, quantified by the PCN index, to its solar wind driver ($E_{\text{K-R}}$) and magnetotail driver (AL_U), i.e.,

$$\text{PCN} \approx \beta_0 + \beta_1 zs(E_{\text{K-R}}) + \beta_2 zs(\text{AL}_\text{U}). \tag{3.1}$$

In this chapter, I investigate whether the linear assumption is valid by comparing the results of the linear model to those of a more general, non-linear model to describe the relationship between the PCN index and $E_{\text{K-R}}$, AL_U. The approach is based on using a non-linear relation called the additive model, which assumes that

$$\text{PCN} \approx \alpha + f_1(E_{\text{K-R}}) + f_2(\text{AL}_\text{U}), \tag{3.2}$$

where $f_1(\cdot)$ and $f_2(\cdot)$ are arbitrary smooth functions. I ask whether a non-linear form of the relationship among the quantities of interest is substantially more successful in predicting the PCN index than the linear model. The objective is to determine the potential optimum predictor of the effect of solar wind parameters on polar cap dynamics, as represented by the PCN index.

The additive (non-linear) analysis is applied to the events used in Chapter 2, and I compare the results with those obtained by the linear regression analysis. I find that (1) the additive model outperforms the linear model in all cases; (2) the improvements by switching from the linear model to the additive model are relatively small, which confirms the validity of the linear assumption; (3) the predicted PCN index values from the additive model are very similar to those obtained from the linear model; (4) the results from both models are adequate.

3.2 Analysis

The goal is to model the dependence of the PCN index on a set of potentially important predictors for at least three reasons. The first is to describe the dependence of the PCN index on the predictors. The second is to access the relative contributions of the predictors in controlling the PCN index. The third is to predict the PCN index to, say, identify unusual activity. In Chapter 2, I identified two important predictors: the electric field of *Kivelson and Ridley* [2008] ($E_{\text{K-R}}$), taken as representative of the polar cap electric field imposed by low-latitude magnetopause reconnection, a form in which saturation is taken into account; and the unloading AL index (AL_U). The standard tool used is the multiple linear regression model given in equation (3.1). In equation (3.1), the solar wind data are propagated to $X_{\text{GSM}} = 17\ R_\text{E}$ by using the technique of *Weimer et al.* [2008] and *Weimer* [2004]. For each individual event, an extra time shift (ΔT) is added to the solar wind data to achieve the highest cross-correlation between $E_{\text{K-R}}$ and the PCN index.

The linear model, equation (3.1), makes a strong assumption about the dependence of the PCN index on $E_{\text{K-R}}$ and AL_U, namely that the dependence is linear in each of the predictors. If this assumption holds, even roughly, then the linear regression model is useful and convenient, because it provides a simple description of the data, summarizes the relative contribution of each predictor with a single coefficient, and provides a simple method for predicting new observations.

Nevertheless, when fitting a linear regression model, no assertion is made that the model is correct. Rather it is widely accepted that the model is a good first order approximation to the true solution, and that the important predictors can be uncovered. It is, however, legitimate to question the validity of the linear assumption. One way to test the validity is to employ a more general, non-linear model to perform the analysis and compare the results with those obtained from the linear analysis.

3.2.1 Additive model

An important feature of the linear regression model (e.g. equation (3.1)) is the additive nature among the predictors. Once I fit the linear model I can examine the predictor effects separately in the absence of interactions. There are many ways to generalize a linear regression model. Of these, the additive model [*Hastie and Tibshirani*, 1990; *Stone*, 1985] is particularly appealing as it retains this important feature of the linear model: it is additive in the predictor effects. Therefore, for the test of non-linearity, I use the additive model, which is

$$\mathrm{PCN} = \alpha + f_1(E_{\mathrm{K\text{-}R}}) + f_2(\mathrm{AL_U}) + \varepsilon_{\mathrm{A}}, \tag{3.3}$$

where α is the intercept, $f_1(E_{\mathrm{K\text{-}R}})$ and $f_2(\mathrm{AL_U})$ are arbitrary univariate (depending on only one variable) smooth functions of $E_{\mathrm{K\text{-}R}}$ and $\mathrm{AL_U}$ respectively and ε_{A} is assumed to be Gaussian noise. If $f_1(E_{\mathrm{K\text{-}R}})$ and α are redefined as

$$f_1^*(E_{\mathrm{K\text{-}R}}) = f_1(E_{\mathrm{K\text{-}R}}) + c, \text{ and } \alpha^* = \alpha - c, \tag{3.4}$$

where c is an constant, equation (3.3) remains unchanged. Thus, to uniquely determine the values of $f_1(E_{\mathrm{K\text{-}R}})$ and $f_2(\mathrm{AL_U})$, two constraints are imposed on equation (3.3) [*Hastie and Tibshirani*, 1986; 1990; *Stone*, 1985], i.e.,

$$\mathrm{E}(f_1(E_{\mathrm{K\text{-}R}})) = 0, \text{ and } \mathrm{E}(f_2(\mathrm{AL_U})) = 0, \tag{3.5}$$

where $\mathrm{E}(X)$ stands for the expectation of X which is estimated from the sample mean.

3.2.2 Backfitting algorithm

The additive model is fitted by the "backfitting algorithm" [*Hastie and Tibshirani*, 1990]. Notice that the conditional expectations of equation (3.3) require that

$$f_1(E_{\text{K-R}}) = \mathrm{E}(f_1(E_{\text{K-R}}) \mid E_{\text{K-R}}) = \mathrm{E}(\text{PCN} - \alpha - f_2(\text{AL}_\text{U}) \mid E_{\text{K-R}}), \tag{3.6}$$

$$f_2(\text{AL}_\text{U}) = \mathrm{E}(f_2(\text{AL}_\text{U}) \mid \text{AL}_\text{U}) = \mathrm{E}(\text{PCN} - \alpha - f_1(E_{\text{K-R}}) \mid \text{AL}_\text{U}), \tag{3.7}$$

where $\mathrm{E}(Y|X=x)$ represents the expectation of Y conditional on $X = x$. Define PCN – $\alpha - f_2(\text{AL}_\text{U})$ and PCN – $\alpha - f_1(E_{\text{K-R}})$ as the partial residuals of $E_{\text{K-R}}$ and AL_U respectively, i.e.,

$$pr(E_{\text{K-R}}) = \text{PCN} - \alpha - f_2(\text{AL}_\text{U}), \tag{3.8}$$

$$pr(\text{AL}_\text{U}) = \text{PCN} - \alpha - f_1(E_{\text{K-R}}). \tag{3.9}$$

Starting with an initial guess, $f_2^{(0)}(\text{AL}_\text{U})$ which usually takes a linear form, the additive model can be fit by iteratively smoothing the partial residuals, i.e.,

$$f_1^{(t+1)}(E_{\text{K-R}}) = S(\text{PCN} - \alpha - f_2^{(t)}(\text{AL}_\text{U})), \tag{3.10}$$

$$f_2^{(t+1)}(\text{AL}_\text{U}) = S(\text{PCN} - \alpha - f_1^{(t+1)}(E_{\text{K-R}})), \tag{3.11}$$

where t records the iteration step, i.e. $t = 0, 1, \cdots$, and S is a smoothing operator taken as LOESS [*Cleveland*, 1979]. Iterations are terminated when

$$f_1^{(t+1)}(E_{\text{K-R}}) \approx f_1^{(t)}(E_{\text{K-R}}) \text{ and } f_2^{(t+1)}(\text{AL}_\text{U}) \approx f_2^{(t)}(\text{AL}_\text{U}). \tag{3.12}$$

Hastie and Tibshirani [1990] provide further details of the backfitting algorithm, e.g. derivation, convergence, rate of convergence, uniqueness of solutions.

3.2.3 Locally weighted scatterplot smoothing

An effective approach to extracting a non-linear representation of scattered data that relates to familiar methods such as least-square regression is referred to as the LOESS (LOcally wEighted Scatterplot Smoothing) method [*Cleveland*, 1979]. The method provides a rigorous approach to obtain a fit to scattered data, or "smoothing" it, by joining the centroids of local straight line fits to portions of the data. In smoothing data values, for each point x_0, k nearest points, denoted by $N(x_0)$, are identified. The distance of the furthest point in the set $N(x_0)$ from x_0,

$$\Delta(x_0) = \max_{x_i \in N(x_0)} |x_0 - x_i|, \tag{3.13}$$

is computed. Weights w_i are assigned to each point in $N(x_0)$, using the tri-cube weight function $W(|x_0 - x_i| / \Delta(x_0))$, where

$$W(u) = [(1 - u^3)^3]_+ \tag{3.14}$$

Here

$$[x]_+ = x, \text{ if } x > 0, \text{ otherwise } [x]_+ = 0. \tag{3.15}$$

The predicted value at x_0 is fitted from the (local) weighted least-square fit confined to $N(x_0)$ using the weights computed above. The locally weighted scatterplot smoothing (LOESS) method can be used to obtain the partial residuals. Thus, the model becomes

$$\mathrm{PCN} = \alpha + lo(E_{\mathrm{K\text{-}R}}, k_1) + lo(\mathrm{AL_U}, k_2) + \varepsilon_{\mathrm{A}}, \tag{3.16}$$

where *lo* stands for LOESS. Here k_1 and k_2, the numbers of nearest neighbors, determine the smoothness of the additive bases, $lo(E_{\mathrm{K\text{-}R}}, k_1)$ and $lo(\mathrm{AL_U}, k_2)$, respectively and ε_{A} is assumed to be Gaussian noise. Diverse choices of k_1 and k_2 are discussed in *Hastie and Tibshirani* [1990] in detail and will not be pursued here. A popular choice is to fix [*Hastie and Tibshirani*, 1990]

$$k_1 = k_2 = 0.5n \tag{3.17}$$

to guarantee enough smoothness, where n is the number of observations. This strategy is adopted in this study and k_1, k_2 will be omitted in later discussions. The computational details are summarized in the following backfitting algorithm.

***Algorithm* 1** (The backfitting algorithm).

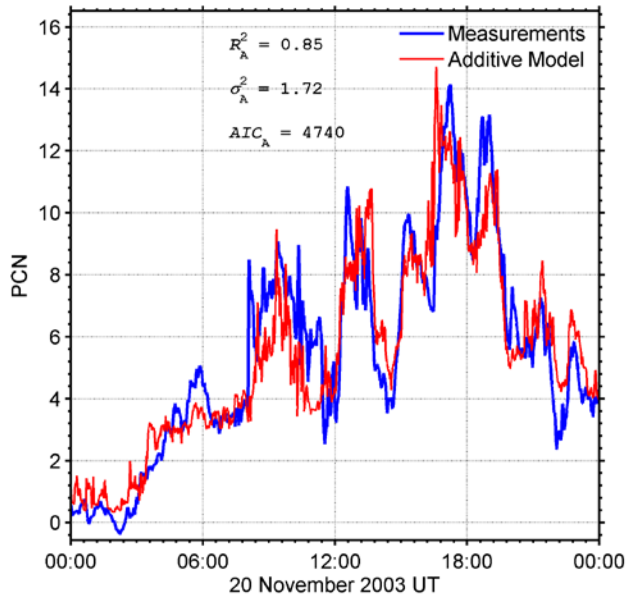

Figure 3.1. Comparison between the measured PCN index (blue line) and the predicted PCN index from an additive model (red line) based on solar wind parameters for the storm of 20 November 2003. R_A^2, σ_A^2 are computed to estimate goodness of fit and AIC_A is used to estimate the model optimality. Reproduced by permission of American Geophysical Union from *Gao et al.* [2012a].

1. Initialize α, $f_1^{(0)}(E_{\text{K-R}})$, and $f_2^{(0)}(\text{AL}_\text{U})$ from the results of linear regression, i.e., $\alpha = \beta_0$, $f_1^{(0)}(E_{\text{K-R}}) = \beta_1 zs(E_{\text{K-R}})$, and $f_2^{(0)}(\text{AL}_\text{U}) = \beta_2 zs(\text{AL}_\text{U})$

2. For $t = 0, 1, \ldots,$:

   i. Compute $f_1^{(t+1)}(E_{\text{K-R}}) = \text{LOESS}(\text{PCN} - \alpha - f_2^{(t)}(\text{AL}_\text{U}), 0.5n)$;

   ii. Compute $f_2^{(t+1)}(\text{AL}_\text{U}) = \text{LOESS}(\text{PCN} - \alpha - f_1^{(t+1)}(E_{\text{K-R}}), 0.5n)$;

   iii. If $\| f_1^{(t+1)}(E_{\text{K-R}}) - f_1^{(t)}(E_{\text{K-R}}) \| < \delta$ and $\| f_2^{(t+1)}(\text{AL}_\text{U}) - f_2^{(t)}(\text{AL}_\text{U}) \| < \delta$, stop; otherwise, repeat i and ii. Here $\|\boldsymbol{x}\|$ stands for the Euclidean norm of a vector $\boldsymbol{x}$, and δ is a pre-defined small number.

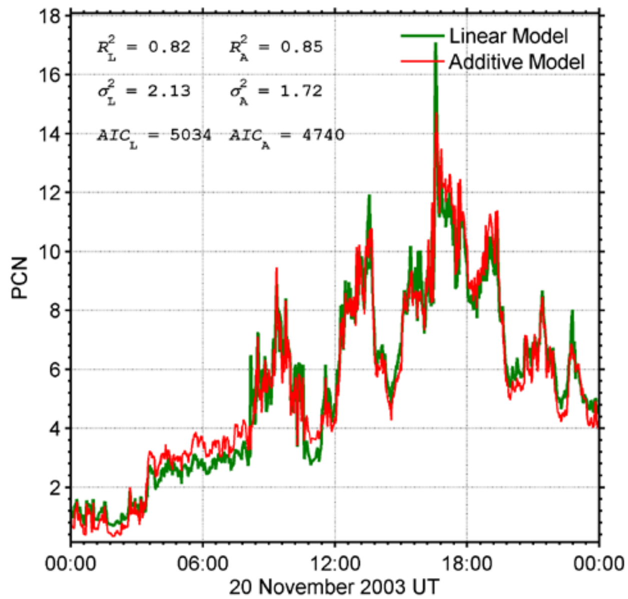

Figure 3.2. Comparison between linear model (green line) and additive model (red line) for the case of 20 November 2003. The change of R^2, error variance and *AIC* can be used to assess the performance of different models. Reproduced by permission of American Geophysical Union from *Gao et al.* [2012a].

In steps i and ii, the notation LOESS(x, k) is adopted in order to emphasize that smoothing of x is achieved by using the LOESS technique with k nearest neighbors. Ideally, $lo(E_{\text{K-R}})$ and $lo(\text{AL}_\text{U})$ in equation (3.16) are obtained from

$$lo(E_{\text{K-R}}) = f_1^{(\infty)}(E_{\text{K-R}}) \text{ and } lo(\text{AL}_\text{U}) = f_2^{(\infty)}(\text{AL}_\text{U}). \tag{3.18}$$

For finite iterations, if the stopping criterion is satisfied after T steps, then

$$lo(E_{\text{K-R}}) \approx f_1^{(T)}(E_{\text{K-R}}) \text{ and } lo(\text{AL}_\text{U}) \approx f_2^{(T)}(\text{AL}_\text{U}). \tag{3.19}$$

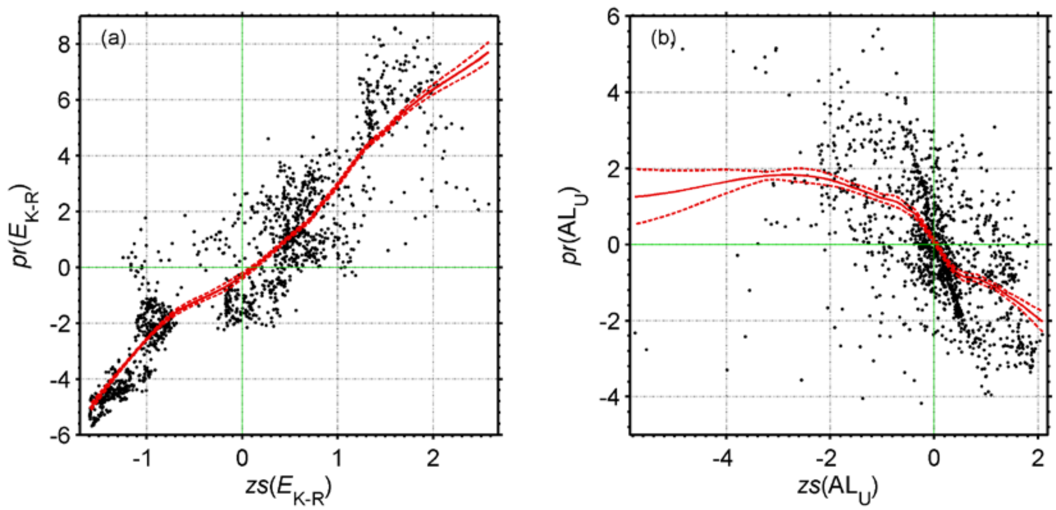

Figure 3.3. Relation of partial residuals $pr(E_{K\text{-}R})$, $pr(AL_U)$ and linear bases $zs(E_{K\text{-}R})$, $zs(AL_U)$ for the case on 20 November 2003. The scatters are between the partial residuals and their corresponding z-scores, i.e. $pr(E_{K\text{-}R})$ versus $zs(E_{K\text{-}R})$, and $pr(AL_U)$ versus $zs(AL_U)$. The red solid lines are the functional relation between $lo(E_{K\text{-}R})$ and $zs(E_{K\text{-}R})$ (left) and between $lo(AL_U)$ and $zs(AL_U)$ (right). The red dashed lines give the corresponding 95% pointwise confidence intervals. The green lines label $zs(E_{K\text{-}R}) = 0$ and $pr(E_{K\text{-}R}) = 0$ (left) and $zs(AL_U) = 0$ and $pr(AL_U) = 0$ (right). Reproduced by permission of American Geophysical Union from *Gao et al.* [2012a].

3.3 Inference

An event on 20 November 2003, shown in Figure 3.1, can help us better understand the approach. In Figure 3.1, the blue line is the measured PCN index and the red line is the predicted PCN index based on the non-linear additive model. The consistency between measurements and predictions is apparent.

In order to quantify the performances of the linear model and the additive model, three statistics, coefficient of determination (R^2), error variance (σ^2) and Akaike's information criterion (*AIC*) [*Akaike*, 1974] are computed to estimate the goodness of fit and model optimality. A

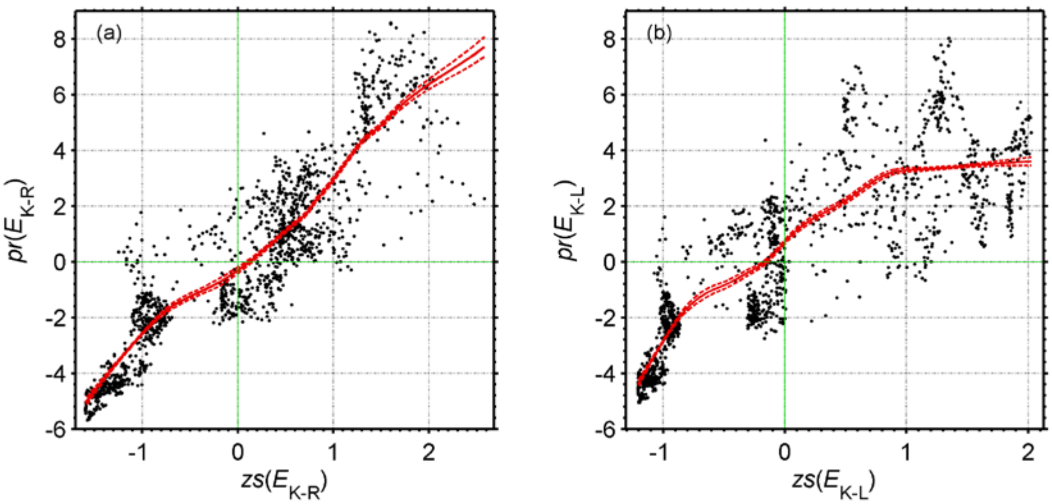

Figure 3.4. (a) Partial residual of $E_{K\text{-}R}$ versus its linear basis; (b) partial residual of $E_{K\text{-}L}$ versus its linear basis on 20 November 2003. The format is the same as Figure 3.3. Reproduced by permission of American Geophysical Union from *Gao et al.* [2012a].

detailed discussion on the definitions and properties of the above statistics in the framework of the additive model is given in the appendix.

For the event of 20 November 2003, the PCN indices predicted by the additive model and by the linear model are shown in Figure 3.2. The additive model slightly outperforms the linear model with increased R^2 (from 0.82 to 0.85), decreased error variance (from 2.13 to 1.72) and reduced *AIC* (from 5034 to 4740). The fitted values from the two models are extremely similar. Figure 3.3 compares the estimated partial residuals of the additive model with the linear bases. The black dots indicate the scatters between the partial residuals and the linear bases, i.e. $pr(E_{K\text{-}R})$ versus $zs(E_{K\text{-}R})$ and $pr(AL_U)$ versus $zs(AL_U)$. The red solid lines, calculated by smoothing the scatters, are $lo(E_{K\text{-}R})$ and $lo(AL_U)$ as functions of $zs(E_{K\text{-}R})$ and of $zs(AL_U)$, respectively. The red dashed lines are the corresponding estimated 95% pointwise confidence intervals. The green

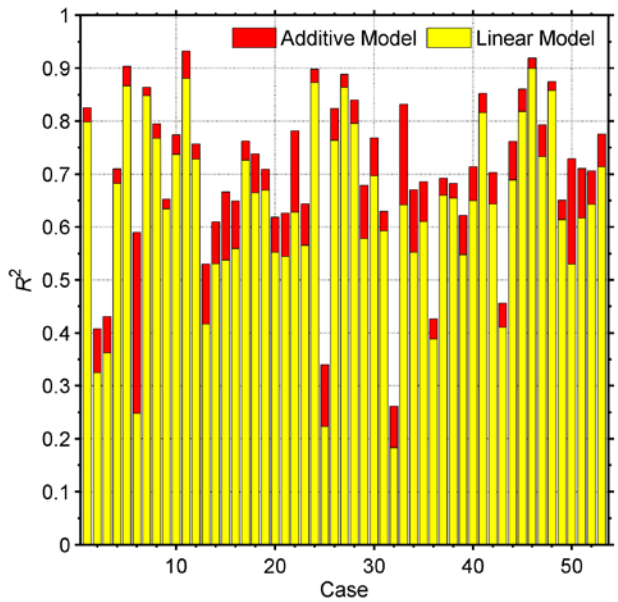

Figure 3.5. R^2 for the linear model and the additive model. The yellow bars indicate the R^2 values for the linear model (R_L^2) and the red bars plotted beneath the yellow bars (but extending to higher values of R^2) give the changes of R^2 by switching from linear model to additive model ($R_A^2 - R_L^2$). Reproduced by permission of American Geophysical Union from *Gao et al.* [2012a].

lines partition the region with $zs(E_{K\text{-}R}) = 0$ and $pr(E_{K\text{-}R}) = 0$ (left) and $zs(AL_U) = 0$ and $pr(AL_U) = 0$ (right). It is clear that $lo(E_{K\text{-}R})$ roughly bears a linear relationship with $zs(E_{K\text{-}R})$, but some nonlinearity between $lo(AL_U)$ and $zs(AL_U)$ develops for this event. Nevertheless, the part with significant deviation from linearity of AL_U lies in the strong geomagnetic activity limit where there are few observations. Thus, if a linear relationship between $lo(AL_U)$ and $zs(AL_U)$ is assumed, no significant error is introduced, which is confirmed by the close correspondence between the fitted values from the linear model and those from the additive model (Figure 3.2).

I also test the performance of $E_{K\text{-}L}$ as a regression basis in the additive model. Since no saturation mechanism is included in $E_{K\text{-}L}$, prominent nonlinearity between $lo(E_{K\text{-}L})$ and $zs(E_{K\text{-}L})$

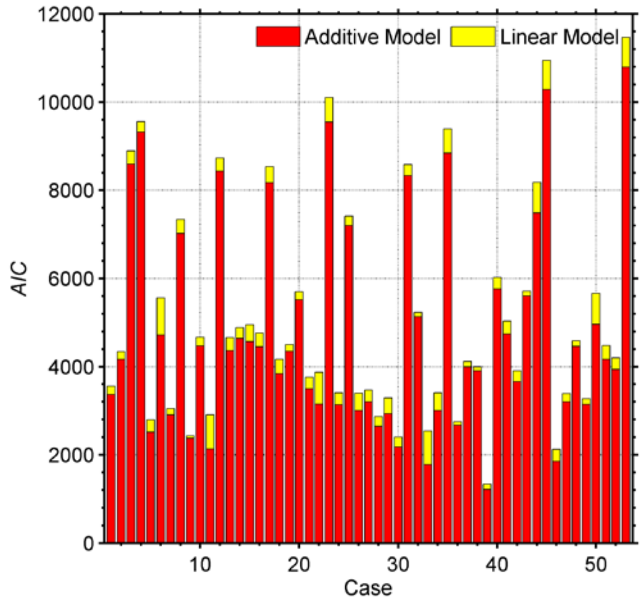

Figure 3.6. Akaike's information criterion (*AIC*) for the linear model and the additive model. The red bars are the *AIC*'s for additive analysis (AIC_A) for all the cases. The yellow bars (this time plotted below the red bars but extending above them) on top of the red bars indicate the increases of *AIC* from additive model to linear model (AIC_L – AIC_A). Reproduced by permission of American Geophysical Union from *Gao et al.* [2012a].

is expected under strong solar wind driving. For the case of 20 November 2003, this is confirmed in Figure 3.4. Figure 3.4 (a) displays the additive basis, $lo(E_{K\text{-}R})$, as an approximately linear function of the linear basis, $zs(E_{K\text{-}R})$, of $E_{K\text{-}R}$. Nevertheless, in Figure 3.4 (b), $lo(E_{K\text{-}L})$ levels off at large values of $zs(E_{K\text{-}L})$. The non-linear relationship between $lo(E_{K\text{-}L})$ and $zs(E_{K\text{-}L})$ is clear.

The same comparisons between the linear model and the additive model, using $E_{K\text{-}R}$ and AL_U as predictors, have been applied to all the cases. The results are summarized in Figure 3.5 and Figure 3.6, which show the change of R^2 and change of *AIC* from the linear model to the

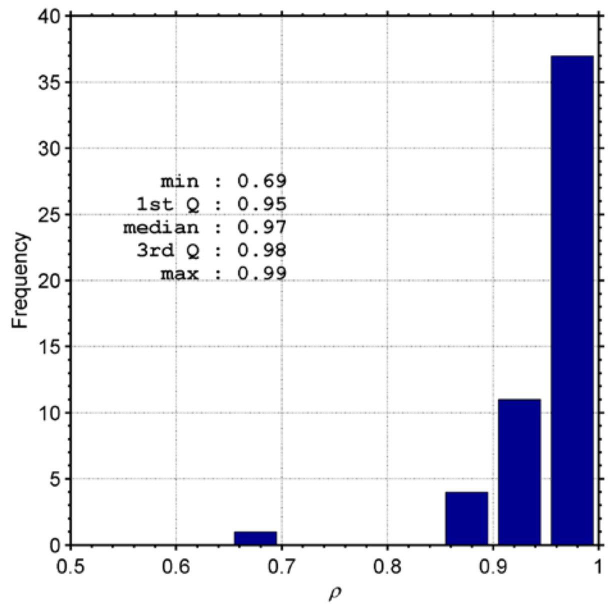

Figure 3.7. Histogram of correlation coefficients of fitted values to the linear model and the additive model. Reproduced by permission of American Geophysical Union from *Gao et al.* [2012a].

additive model. For all the cases, the additive model systematically outperforms the linear model with increased R^2 and decreased *AIC*. Nevertheless, the improvements are relatively small.

A more direct approach is to compare the fitted values of the linear model with those of the additive model by calculating their correlation coefficients whose distribution is shown in Figure 3.7. The correlation coefficients concentrate near 1 with only one exception on 18 February 1999. For this case, the prediction from the linear model fails with R^2 = 0.25 as is shown in Figure 3.8. The non-linearity between the additive bases and linear bases for this case is clear as shown in Figure 3.9. It also corresponds to the largest increase of R^2 from the linear model to the additive model in Figure 3.5. Moreover, significant difference between PCS and

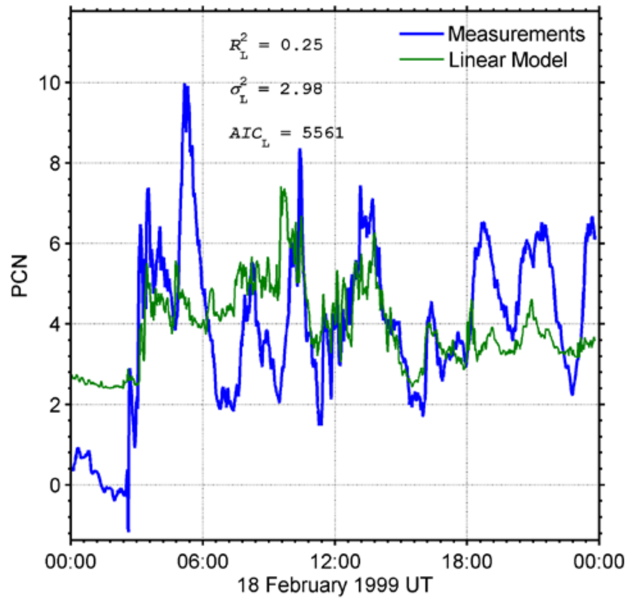

Figure 3.8. Comparison between measured PCN index (blue line) and predicted PCN index based on linear model (green line) on 18 February 1999. This is the only case during which the additive model gives inconsistent results with those obtained from the linear model. Reproduced by permission of American Geophysical Union from *Gao et al.* [2012a].

PCN are found between 06:00 UT and 12:00 UT (not shown here). A detailed discussion of this case can be found in *Gao* [2012a].

Furthermore, it is of great importance to compare the relative contributions to the PCN index from two predictors in the additive model and compare the result with that obtained from the linear model. Unlike the linear model for which the contribution of each predictor is summarized in a regression coefficient, the contribution of a predictor in an additive model, $E_{\text{K-R}}$ say, has to be calculated from its additive basis, i.e. $lo(E_{\text{K-R}})$. The standard deviation of $lo(\text{E}_{\text{K-R}})$ and that of $lo(\text{AL}_{\text{U}})$ summarize the contributions to PCN from $E_{\text{K-R}}$ and AL_{U} respectively, and thus, can be used to compare their relative importance in controlling the PCN index. Figure 3.10

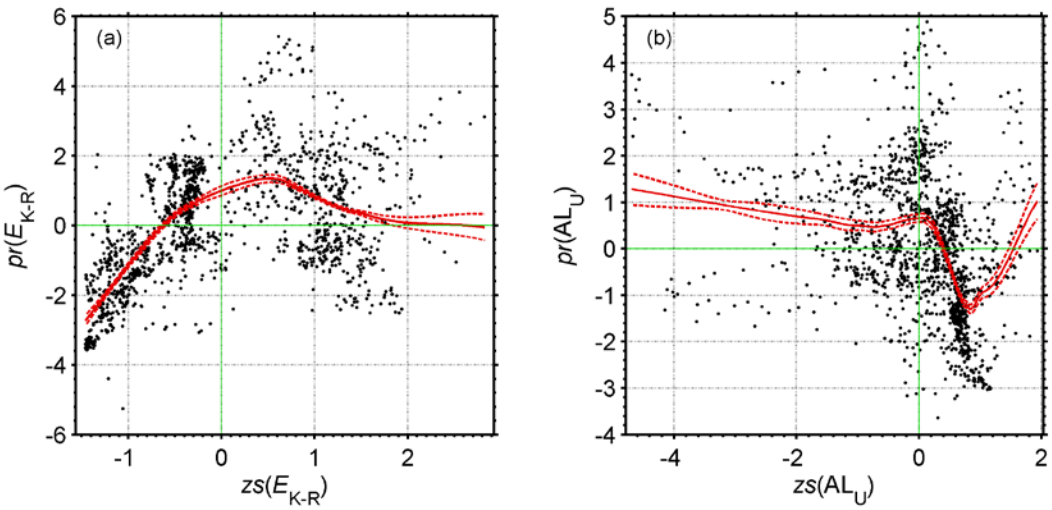

Figure 3.9. As for Figure 3.3 for the event on 18 February 1999. Reproduced by permission of American Geophysical Union from *Gao et al.* [2012a].

shows a scatter plot of the standard deviations of $lo(E_{\text{K-R}})$, denoted as $|\sigma_{lo(E_{\text{K-R}})}|$, and $lo(\text{AL}_\text{U})$, similarly written as $|\sigma_{lo(\text{AL}_\text{U})}|$, for those cases with $R_\text{A}^2 \geq 0.5$. The points are both colored and scaled according to their R_A^2 values. An orthogonal regression between $|\sigma_{lo(\text{AL}_\text{U})}|$ and $|\sigma_{lo(E_{\text{K-R}})}|$ forced to pass through origin is added as the blue line. The regression coefficient, 0.47, indicates that the contribution of $E_{\text{K-R}}$ to PCN is roughly twice as important as AL_U in an additive model. This is consistent with the result of chapter 2 based on the linear assumption between the PCN index and $E_{\text{K-R}}$, AL_U.

If the potential non-linearity between AL and $E_{\text{K-R}}$ is taken into account, an additive model can be used to derive the unloading AL, denoted as $\text{AL}_{\text{U,A}}$ here, i.e.

$$\text{AL}_{\text{U,A}} = \text{AL} - \text{AL}_{\text{D,A}}, \tag{3.20}$$

where

$$\text{AL}_{\text{D,A}} = \alpha_0 + lo(E_{\text{K-R}}, 0.5n). \tag{3.21}$$

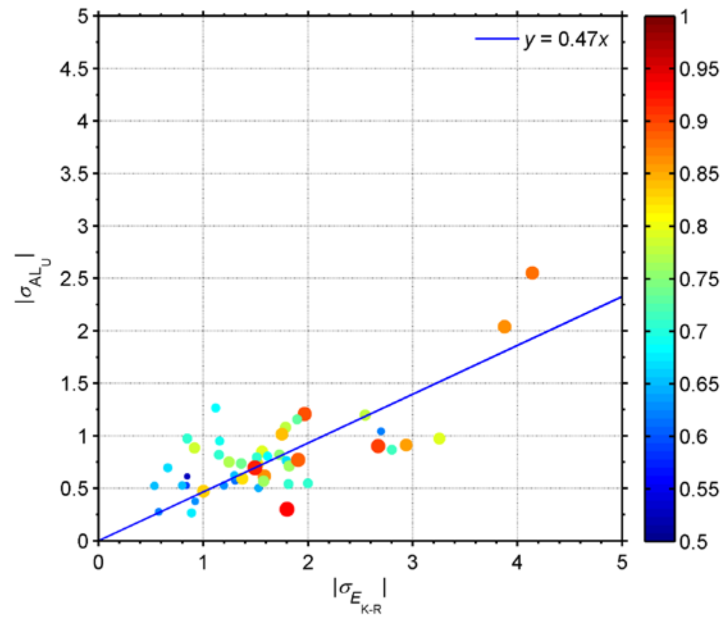

Figure 3.10. Scatter plot of standard deviations of $lo(\mathrm{AL_U})$ versus that of $lo(E_{\mathrm{K\text{-}R}})$ for those cases with $R_A^2 \geq 0.5$. The points are both colored and scaled according to the corresponding R_A^2. An orthogonal regression between $|\sigma_{lo(\mathrm{AL_U})}|$ and $|\sigma_{lo(E_{\mathrm{K\text{-}R}})}|$ in blue line was forced to pass through origin. Reproduced by permission of American Geophysical Union from *Gao et al.* [2012a].

Accordingly, the additive model, equation (3.16), is updated to

$$\mathrm{PCN} = \alpha' + lo(E_{\mathrm{K\text{-}R}}, 0.5n) + lo(\mathrm{AL_{U,A}}, 0.5n) + \varepsilon_A'. \quad (3.22)$$

I find that the results obtained by using equation (3.22) are quite similar to those obtained by using equation (3.16). Besides, it is more convenient to examine the differences between the additive model and the linear model, if the same variable, $\mathrm{AL_U}$, is used in the two models. For example, in Figure 3.3 (b), I compare the additive basis, $lo(\mathrm{AL_U})$, directly with the linear basis, $zs(\mathrm{AL_U})$. However, if, instead, $\mathrm{AL_{U,A}}$ is used, then I am only able to compare $lo(\mathrm{AL_{U,A}})$ with $zs(\mathrm{AL_{U,A}})$, which is not used in the linear model. Therefore, I report the results obtained by using equation (3.16).

3.4 Discussion and conclusions

In this Chapter, I study the response of polar cap dynamics as characterized by the PCN index to solar wind parameters and geomagnetic activity under strong solar wind driving by extending the linear regression analysis between the PCN index and $E_{K\text{-}R}$, AL_U to a more general, non-linear model, i.e. an additive model (equation (3.16)). Here, $E_{K\text{-}R}$ is used as a representative of the electric field imposed on the ionosphere by low-latitude magnetopause reconnection, modified to account for saturation. I compare the results with those obtained from the linear model by using the same cases as that used in Chapter 1. I find that although, in general, the additive model outperforms the linear model with increased R^2 and decreased *AIC*, the improvements obtained by switching from a linear model to an additive model are small. Thus, the validity of the linear assumption is confirmed. The fitted values from the two models are extremely similar to each other, with the distribution of the correlation coefficient between the linear fits and the additive fits concentrating near 1 with one exception, an event on 18 February 1999. This is an anomalous case that is discussed fully in *Gao* [2012a]. With one exception, the results from the two models are quite similar. They both show that $E_{K\text{-}R}$ is approximately twice as important as AL_U in controlling the PCN index. Although the additive model of the PCN index as a response to $E_{K\text{-}R}$ and AL_U is more flexible in the sense that it does not require that the PCN index vary linearly with the independent quantities, the linear model already provides a very good approximation. Furthermore, the linear model gives a simpler description of the data by summarizing the contribution of each predictor in a regression coefficient and is easier to be extended to more advanced analysis, e.g. robust regression. The usage of a linear model in this problem is highly encouraged.

Appendix A

In this appendix, I provide the definitions and properties of the statistics used in this chapter, i.e. prediction efficiency (R^2), error variance (σ^2) and Akaike's information criterion (AIC). For ease of discussion, I define $\boldsymbol{y}$ as the vector of observations and $\hat{\boldsymbol{y}}_+$ as the vector of additive fits. It is important to notice that to fit an additive model is equivalent to generating a mapping from $\boldsymbol{y}$ to $\hat{\boldsymbol{y}}_+$, i.e.,

$$\hat{\boldsymbol{y}}_+ = \mathbf{R}\boldsymbol{y}, \tag{3.23}$$

where $\mathbf{R}$ is the mapping matrix. Then, R^2, σ^2 and AIC can be computed from $\boldsymbol{y}$, $\hat{\boldsymbol{y}}_+$ and $\mathbf{R}$.

For an additive model, the coefficient of determination, i.e. R_A^2, is defined as [*Hastie and Tibshirani*, 1990; *Myers*, 2000]

$$R_A^2 = 1 - D(\boldsymbol{y}; \hat{\boldsymbol{y}}_+) / D(\boldsymbol{y}; \bar{y}\mathbf{1}). \tag{3.24}$$

In the above equation, $D(\boldsymbol{y}; \hat{\boldsymbol{y}}_+)$ is the deviance, calculated as

$$D(\boldsymbol{y}; \hat{\boldsymbol{y}}_+) = \| \boldsymbol{y} - \hat{\boldsymbol{y}}_+ \|^2, \tag{3.25}$$

where $\boldsymbol{y} - \hat{\boldsymbol{y}}_+$ is the model residual vector, $\|\boldsymbol{x}\|$ indicates the Euclidean norm of vector $\boldsymbol{x}$. $D(\boldsymbol{y}; \bar{y}\mathbf{1})$, the null deviance, is defined as

$$D(\boldsymbol{y}; \bar{y}\mathbf{1}) = \| \boldsymbol{y} - \bar{y}\mathbf{1} \|^2, \tag{3.26}$$

where $\bar{y}$ is the sample mean and $\mathbf{1} = (1, 1, \cdots, 1)^T$. R_A^2, varying between 0 and 1, can be interpreted as the fraction of variations explained by the model. The error variance for an additive model is calculated as

$$\sigma_A^2 = D(\boldsymbol{y}; \hat{\boldsymbol{y}}_+) / df_{err}. \tag{3.27}$$

Here df_{err}, the error degree of freedom, is computed from [*Hastie and Tibshirani*, 1990]

$$df_{err} = n - \mathrm{tr}(2\mathbf{R} - \mathbf{R}\mathbf{R}^T), \tag{3.28}$$

where n is the number of observations, $\mathbf{R}$ is the mapping matrix in equation (3.23) and tr($\mathbf{A}$) stands for the trace of matrix $\mathbf{A}$. R_L^2 and σ_L^2 for the linear model can be similarly defined by replacing $\hat{\boldsymbol{y}}_+$ with the least-square fits, $\hat{\boldsymbol{y}}_{LS}$, of a linear model, i.e.

$$R_L^2 = 1 - D(\boldsymbol{y}; \hat{\boldsymbol{y}}_{LS}) / D(\boldsymbol{y}; \bar{y}\mathbf{1}), \tag{3.29}$$

and df_{err} with $n - p$, i.e.,

$$\sigma_L^2 = D(\boldsymbol{y}; \hat{\boldsymbol{y}}_{LS}) / (n - p). \tag{3.30}$$

where p is the number of parameters, e.g. $p = 3$ for equation (3.3) [*Myers*, 2000].

Akaike's information criterion (AIC), in general, is defined as [*Akaike*, 1974]

$$AIC = -2 \ln L + 2\, p, \tag{3.31}$$

where L is the maximized value of the likelihood function for the estimated model and p is still the number of parameters in a model. Given a set of candidate models for the data, the preferred model is the one with the minimum AIC value, since AIC not only rewards goodness of fit, but also includes a penalty that is an increasing function of the number of estimated parameters. In practice, a convenient form arises from writing ln(L) as [*Burnham and Anderson*, 2002]

$$\ln(L) = C - (n / 2) \ln(D(\boldsymbol{y}; \hat{\boldsymbol{y}}) / n)\ , \tag{3.32}$$

where $\boldsymbol{y}$ is the vector of observations, $\hat{\boldsymbol{y}}$ is the vector of fitted values, and C is a constant independent of the model used. Thus, AIC becomes

$$AIC_L = n \ln (D(\boldsymbol{y}; \hat{\boldsymbol{y}}_{LS}) / n) + 2\, p - 2C \tag{3.33}$$

for a linear model, or

$$AIC_A = n \ln (D(\boldsymbol{y}; \hat{\boldsymbol{y}}_+) / n) + 2\, \mathrm{tr}(\mathbf{R}) - 2C \tag{3.34}$$

for an additive model. In the above equation, tr($\mathbf{R}$), an estimator of p, is the effective number of parameters of an additive model [*Hastie and Tibshirani*, 1990].

CHAPTER 4

Long-Term Variations of Driven and Unloading Contributions to the PCN Index

4.1 Introduction

In Chapter 2, I found that the polar cap dynamics, represented by the PCN index, responds to both the solar wind direct driving and the magnetotail energy unloading. If the solar wind driving is quantified by $E_{\text{K-R}}$, the electric field proposed by *Kivelson and Ridley* [2008], and the magnetotail energy unloading is described by AL_U, the unloading AL index, then, in general, the PCN index can be well predicted from $E_{\text{K-R}}$ and AL_U through

$$\text{PCN} = \beta_0 + \beta_1\, zs(E_{\text{K-R}}) + \beta_2\, zs(\text{AL}_\text{U}) + \varepsilon, \tag{4.1}$$

where β_0, β_1, and β_2 are constants estimated from regression between PCN and $E_{\text{K-R}}$, AL_U, *zs* stands for z-score, and ε is assumed to be Gaussian noise. The relative importance of $E_{\text{K-R}}$ and AL_U in determining PCN is measured by the relative magnitudes of β_1, β_2.

In this chapter, I investigate the driven and unloading contributions to the PCN index by extending the analysis in Chapter 2 to encompass solar cycle 23. In Section 4.2, I apply regression analysis day-by-day from 1 February 1998 to 31 December 2009. I find that (1) the relative contributions of driven and unloading components varies within solar cycle 23 with a

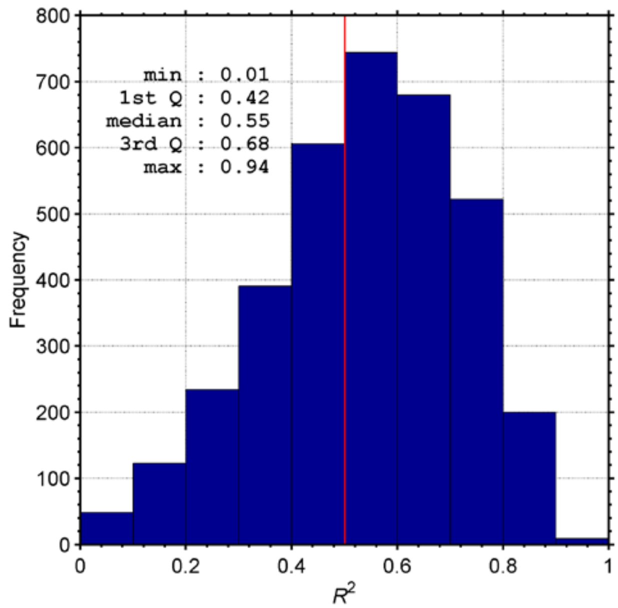

Figure 4.1. Distribution of R^2 when applying equation (4.1) to cases between 1 February 1998 and 31 December 2009. R^2 = 0.5, shown as the red vertical line, has been used as a criterion to select events for further analysis. 2155 out of 3557 cases satisfy this criterion. Reproduced by permission of American Geophysical Union from *Gao et al.* [2012b].

magnitude ±5%, with the driven-to-unloading ratio highest near solar minimum and lowest slightly after solar maximum; (2) the driven-to-unloading ratio peaks in summer and decreases in winter; and (3) the magnitude of the annual variation can be as large as ±15%. In Section 4.3, I summarize the results and discuss the physical mechanisms that can be responsible for the solar cycle variation and annual variation.

4.2 Analysis

In this chapter, I apply the regression analysis day by day from 1 February 1998 to 31 December 2009. This includes most of solar cycle 23. Here, the contributions from $E_{K\text{-}R}$ and AL_U relative to the variations of the PCN index are of interest. The model is equation (4.1). The consistency

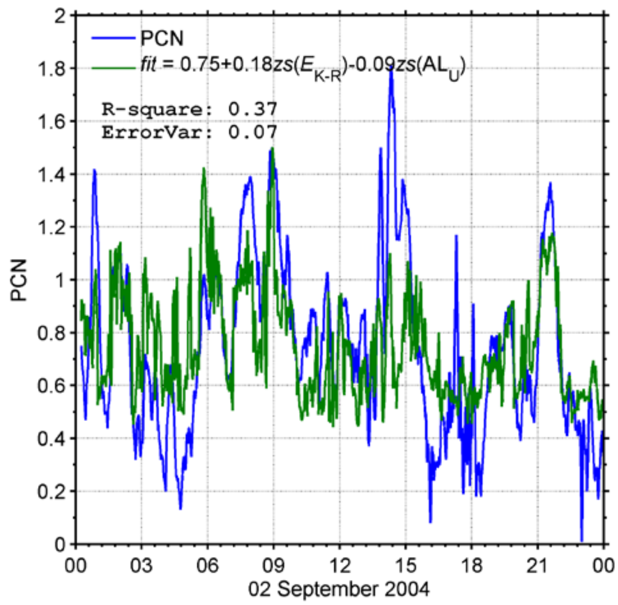

Figure 4.2. Comparison between the PCN index and the predicted PCN index based on solar wind parameters for September 2, 2004. The blue line is the measured PCN index. The green line is the predicted PCN index based on a linear regression from $E_{K\text{-}R}$ and AL_U. Reproduced by permission of American Geophysical Union from *Gao et al.* [2012b].

between the measured PCN index and the predicted PCN index is quantified by R^2 and error variance.

The distribution of R^2 for all the cases from 1 February 1998 to 31 December 2009 is shown in Figure 4.1, which can be summarized as: minimum, 0.01; 1st quartile, 0.42; median, 0.55; 3rd quartile, 0.68; and maximum, 0.94. $R^2 \geq 0.5$ is used as a criterion to select cases for further analysis. 2155 out of 3557 cases are retained. (Owing to missing data, not every day returns a result.) Among those cases with R^2 less than 0.5, some are influenced by unusual activity (Figure 2.20), but most are because the PCN index signal-to-noise ratio is too small to be distinguished from background noise. An example of such a case is shown in Figure 4.2. For this

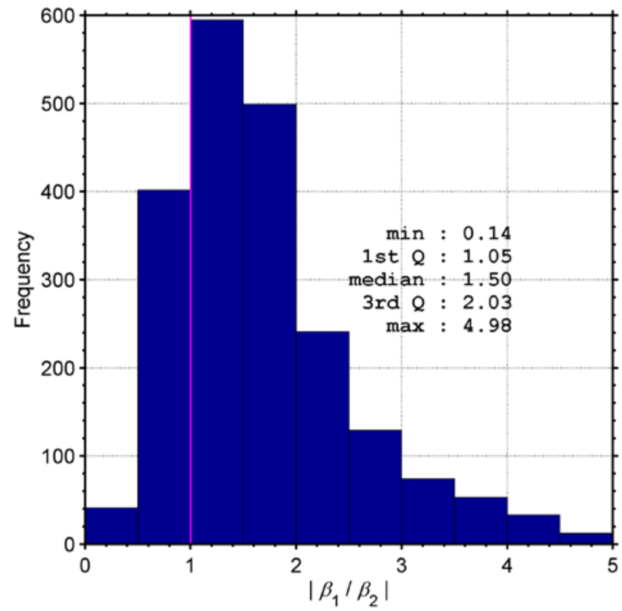

Figure 4.3. Histogram of *DUR* for events with $R^2 \geq 0.5$ between 1 February 1998 and 31 December 2006, which can be summarized as: minimum, 0.14; 1st quartile, 1.05; median, 1.5; 3rd quartile, 2.03; maximum, 4.98. The red vertical line indicates equal contributions from driven and unloading to the PCN index. Reproduced by permission of American Geophysical Union from *Gao et al.* [2012b].

interval, the PCN index was small (PCN < 1.8). The blue line stands for the measured PCN index, while the green line represents the PCN index predicted from equation (4.1). Clearly, they are inconsistent. This is confirmed by the low R^2 (0.37). In contrast, Figure 2.11 (b) shows a case on 20 November 2003. This is an interval when the magnetosphere-ionosphere system was experiencing strong driving from the solar wind. The measured PCN index was roughly an order of magnitude larger than for the case of Figure 4.2, and the measured and predicted PCN indices are highly correlated, with $R^2 = 0.83$.

To describe the relative importance of the driven and unloading effects on the PCN index, I define the driven-to-unloading ratio (*DUR*) as

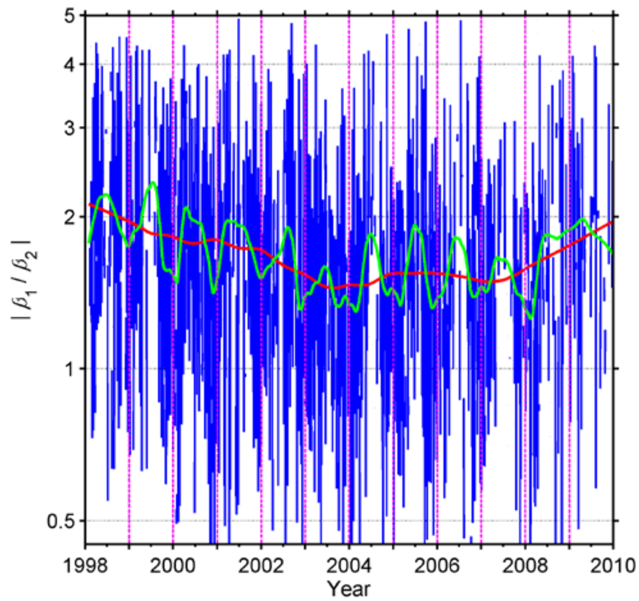

Figure 4.4. The time series with 1-day resolution of *DUR* from 1 February 1998 to 31 December 2009 is plotted in blue. The green line is the LOESS smoothed blue line with k = 60. The red line is the LOESS smoothed blue line with k = 700. The magenta vertical lines separate different years. Notice that the y axis is spaced in a logarithmic scale. Reproduced by permission of American Geophysical Union from *Gao et al.* [2012b].

$$DUR = |\, \beta_1 / \beta_2 \,|, \tag{4.2}$$

where β_1 and β_2 are regression coefficients in equation (4.1). The distribution of *DUR* is shown in Figure 4.3. Probability concentrates between 0.5 and 3 with summary statistics: minimum, 0.14; 1st quartile, 1.05; median, 1.50; 3rd quartile, 2.03; and maximum, 4.98.

4.2.1 Variation in solar cycle 23

The time series of 1-day *DUR* from 1 February 1998 to 31 December 2009 is shown in Figure 4.4. Large variation characterizes the evolution of *DUR* through solar cycle 23. To obtain more useful information, appropriate smoothing needs to be applied to the raw *DUR* time series by using the technique of LOESS [*Cleveland*, 1979]. The raw and LOESS smoothed *DUR*s are

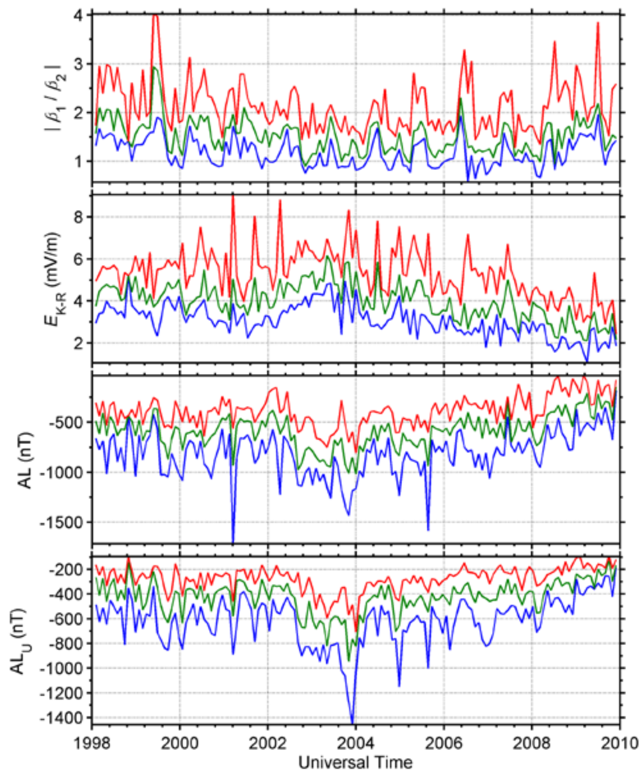

Figure 4.5. Time series of the monthly averaged quantities from top to bottom: *DUR*, $E_{\text{K-R}}$, AL, and AL_{U}. The red, green and blue lines indicate the 3rd quartile, median and 1st quartile respectively. Reproduced by permission of American Geophysical Union from *Gao et al.* [2012b].

shown in Figure 4.4. The green line is the LOESS smoothed *DUR* with k = 60 (~ ±1 month), while the red line has k = 700 (~ ±1 year). The green line reveals the annual variations of the *DUR* which peaks in summer and drops low in winter. This topic is pursued in the next section. The red line removes most of the annual variations and represents the variation of *DUR* within solar cycle 23. It reveals an interesting property. Within solar cycle 23, the *DUR* decreased as solar activity increased and increased as solar activity decreased. It is estimated that the solar cycle effect varies the trend of *DUR* by ±5%.

Quantities related to PCN are plotted in Figure 4.5. From top to bottom, plotted are the monthly averaged *DUR*, $E_{\text{K-R}}$, AL and AL_U. The blue, green and red lines are 1st quartile, median and 3rd quartile respectively. During the transition from solar minimum to solar maximum, the electric field increases as expected. Nevertheless, the magnitude of AL_U increases even more and thus reduces the *DUR*.

I believe that the change of *DUR*, the relative contribution of $E_{\text{K-R}}$ and AL_U to the PCN index, through solar cycle 23 is likely to result from the enhancement of Hall conductance in the auroral zone induced by increased electron precipitation just after solar maximum, concurrent with the peak strength of high-speed streams [*Emery et al*. 2009]. The PCN index depends on the strength of ionospheric Hall currents both in the polar cap [*Takalo and Timonen*, 1990; *Vennerstrøm et al*. 1991] and in the auroral electrojet. The form of the dependence of the polar cap currents on $E_{\text{K-R}}$ is not likely to change much through a solar cycle. The Hall current, contributed by the solar wind driving, is calculated as

$$J_\text{D} = \Sigma_\text{I} E_{\text{K-R}}, \tag{4.3}$$

where J_D represents the Hall current driven by the solar wind electric field, and Σ_I is the Hall conductance that arises from ionization by solar illumination [e.g. *Robinson and Vondrak*, 1984]. The Hall current in the auroral zone is dominated by electron precipitation, implying that the current in the auroral electrojet, J_U, can be expressed as

$$J_\text{U} = \Sigma_{\text{E-P}} E_\text{U}, \tag{4.4}$$

where $\Sigma_{\text{E-P}}$ stands for the Hall conductance in the night hemisphere primarily caused by the electron precipitation (E-P) [e.g. *Spiro et al*. 1982], and E_U is the ionospheric signature of the tail convection electric field. The unloading AL index, AL_U, primarily responds to J_U [*Bargatze et al*. 1985; *McPherron and Baker*, 1993] and can be expressed as

$$\mathrm{AL_U} \propto J_\mathrm{U} = \Sigma_\mathrm{E\text{-}P}\, E_\mathrm{U}, \tag{4.5}$$

Østagaard et al. [2002] related AE and $\Sigma_{E\text{-}P}$ to P_e, the hemispherical energy dissipation by auroral electrons, as

$$\Sigma_\mathrm{E\text{-}P} \propto P_\mathrm{e}^{1/2}. \tag{4.6}$$

Emery et al. [2009] studied the relationship between the hourly-averaged global energy dissipation by auroral electrons ($P_{e,G}$) and three types of solar wind structures: slow speed streams (v < 400km/s), high-speed streams (HSS) (v > 400km/s), and transient structures associated with coronal mass ejections (CME) over three solar cycles. Here $P_{e,G}$ measures the energy dissipation by auroral electrons in both hemispheres. Therefore, apart from seasonal variations, $P_{e,G}$ is approximately $2P_e$, i.e.,

$$P_\mathrm{e,G} \approx 2P_\mathrm{e}. \tag{4.7}$$

Emery et al. [2009] found that $P_{e,G}$, and thus P_e, is most effectively controlled by HSS whose strength peaks at the beginning of the descending phase of a solar cycle.

If I assume that, on the time scale of months, the magnitudes of $E_{K\text{-}R}$ and E_U vary proportionally, i.e.,

$$E_\mathrm{U} \propto E_\mathrm{K\text{-}R}, \tag{4.8}$$

the relative magnitude of direct driving and unloading of the PC index in solar cycle 23 can be understood. An increase of $\Sigma_{E\text{-}P}$ due to the enhancement of P_e results in a decrease in *DUR*. As P_e, and thus $\Sigma_{E\text{-}P}$, peak slightly after the solar maximum, *DUR* reaches its minimum at that phase of the solar cycle. Thereafter, *DUR* starts to increase as P_e and $\Sigma_{E\text{-}P}$ decrease (see Figure 2c in *Emery et al.* [2009] for a detailed description of variation of P_e in solar cycle 23). However, at this stage, the proposed interpretation is speculative. Further studies of the variation with solar cycle of the relative importance of $E_{K\text{-}R}$ and $\mathrm{AL_U}$ in driving the PCN index are needed.

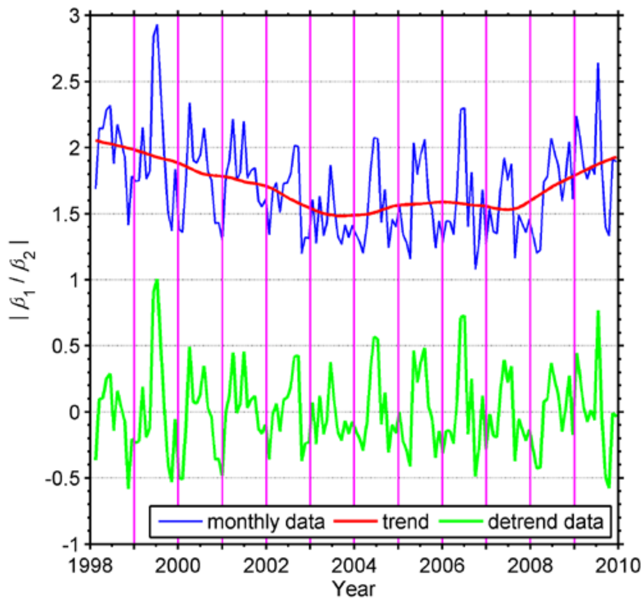

Figure 4.6. Monthly *DUR* in blue and its solar cycle trend in red. The green line is the detrended monthly *DUR*. Reproduced by permission of American Geophysical Union from *Gao et al.* [2012b].

4.2.2 Seasonal variation

The green line in Figure 4.4 shows that superimposed on the solar cycle variation of the *DUR* there is also an annual variation. Considerations related to the sources of conductance at high latitudes can also help explain the seasonal effects in *DUR*, the matter to which I turn in this section. I calculated the monthly *DUR* by using 30 day block averages. As the solar cycle trend is independent of seasonal variations, I remove it as shown in Figure 4.6 by subtracting the trend (red line) from the monthly *DUR*. An autocorrelation function (ACF) [e.g. *Shumway and Stoffer*, 2006] of the detrended monthly *DUR* time series is shown in Figure 4.7. A periodicity of 12 months is identified with peaks at lags of 13, 24, 37, and 48 months in ACF.

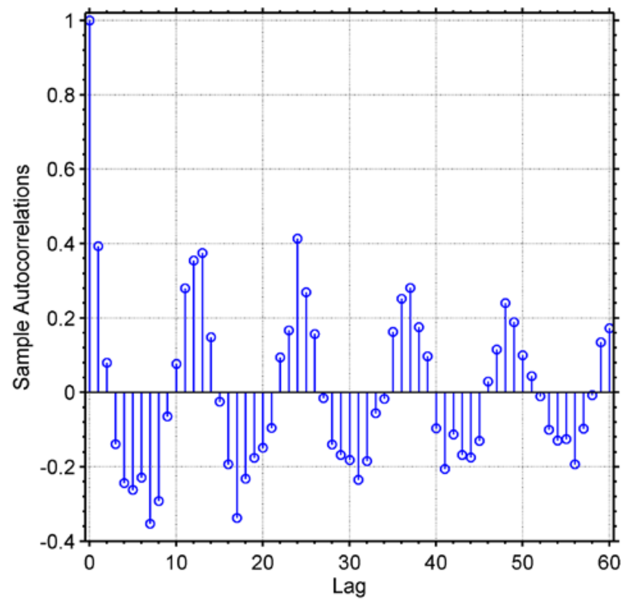

Figure 4.7. Autocorrelation function (ACF) of the detrended monthly *DUR* time series. 1 lag in the *x* axis indicates a month. Thus, with positive peaks at lags 13, 24, 37, 48, this indicates a periodicity of 12 months. Reproduced by permission of American Geophysical Union from *Gao et al.* [2012b].

To better resolve the periodicity, spectral analysis is performed on the monthly detrended *DUR* time series. Figure 4.8 shows the periodogram [e.g. *Shumway and Stoffer*, 2006] of the detrended monthly *DUR* time series. The abscissa is physical frequency with units per month. The ordinate is power per frequency. The strongest power is peaked at 0.08 /month corresponding to a 12 month periodicity. A smaller peak near 0.16 /month corresponds to a semi-annual variation. Other small peaks remain.

A smoother spectral estimation is obtained through the Yule-Walker method [*Walker*, 1931; *Yule*, 1927]. In this method, an autoregressive model of order p (AR(p)) is fitted to the time series, as

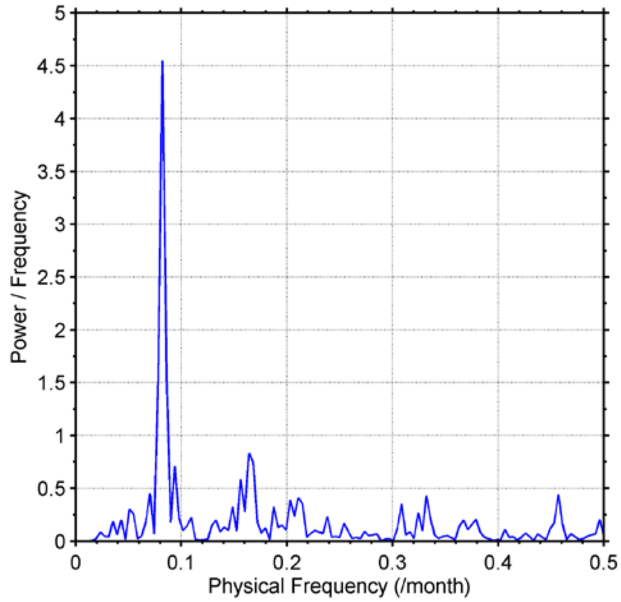

Figure 4.8. Periodogram of the detrended monthly DUR time series. The abscissa is physical frequency with unit per month. The ordinate is power per frequency. Strong power concentrates at 0.08 /month, which corresponds to a 12 month period. Some power lies at 0.16 /month, which maps to the semi-annual variation. Reproduced by permission of American Geophysical Union from *Gao et al.* [2012b].

$$x_t = \varphi_1 x_{t-1} + \varphi_2 x_{t-2} + \ldots + \varphi_p x_{t-p} + \omega_t, \tag{4.9}$$

where x_t is the observation at time t, and φ_1, φ_2, …, φ_p are regression coefficients, and ω_t are assumed to be Gaussian white noise with $E(\omega_t) = 0$ and $\mathrm{var}(\omega_t) = \mathrm{const}$. The spectral estimation is calculated theoretically from φ_1, φ_2, …, φ_p [e.g., *Shumway and Stoffer*, 2006]. The optimal order p is evaluated by Akaike's information criterion (AIC) [*Akaike*, 1973], defined as

$$AIC = \ln \sigma_m^2 + (n + 2p) / n. \tag{4.10}$$

Here

$$\sigma_m^2 = SS_{Res} / n, \tag{4.11}$$

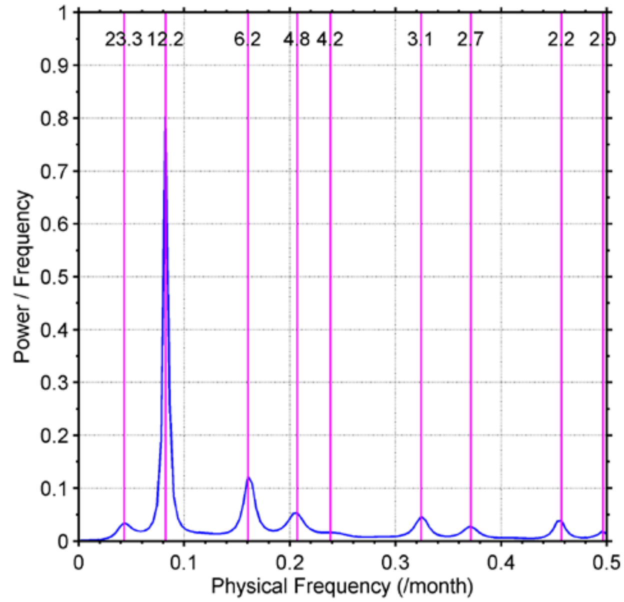

Figure 4.9. Spectrum estimated by using the Yule-Walker method (described in text). The format is the same as Figure 4.8. The vertical magenta lines locate the positions of the local peaks. The numbers are the periods in months corresponding to the peaks. Reproduced by permission of American Geophysical Union from *Gao et al.* [2012b].

where SS_{Res} is the residual sum of squares using autoregression of order p, n is the number of observations. *AIC* balances the goodness of fit, measured by σ_m^2, against the model complexity, quantified by p. An optimal model results in minimum *AIC*. The optimal order in this study is

$$p = 24. \tag{4.12}$$

The corresponding Yule-Walker spectrum is shown in Figure 4.9. The similarity between Figure 4.8 and Figure 4.9 is clear with major peaks aligning at the same physical frequencies. The advantage of the Yule-Walker spectrum is that only important peaks remain, which provides a chance to study them one by one. For the spectrum, two peaks at 12 and 6 months are much more significant than the rest. I interpret the annual variation in terms of seasonal variations of ionospheric conductance. Conductance is enhanced in summer due to the shorter effective light path caused by decreasing the solar zenith angle. For example, *Robinson and Vondrak* [1984] found that

$$\Sigma_I \propto \cos^{1/2}\chi, \tag{4.13}$$

where χ is solar zenith angle. With higher Hall conductance in summer, a higher *DUR* in summer is expected. AL, on the other hand, arises from currents that flow in regions where the conductance is dominated by electron precipitation [e.g. *Spiro et al*. 1982].

Previous studies have demonstrated that conductance caused by electron precipitation varies with season. For example, *Ridley* [2007] proposed that there was 20% more electron precipitation in the winter hemisphere than in the summer hemisphere. *Emery et al.* [2008] found that the power in precipitated electrons was 35% higher in the summer hemisphere under quiet conditions and 40% higher in the winter hemisphere under active conditions. Thus, there is some ambiguity regarding the seasonal variation of precipitation-controlled conductance, and it is beyond the scope of this paper to investigate this matter. My results suggest that the seasonal variations of solar illumination outweigh the effects of electron precipitation in controlling the *DUR* as shown in Figure 4.4. In Figure 4.4, the green line, the LOESS smoothed *DUR* with k = 60, peaks in summer every year, indicating that, in general, the driven component increases more than the unloading component in summer months. The current study is consistent with *Vennerstrøm et al.*, [1991] who showed that the PC index correlates better with the AE, and AL indices in winter (ρ = 0.8-0.9) than in summer (ρ = 0.6-0.8). In winter, smaller conductance resulting from diminished solar illumination results in weaker direct driving (compared with summer) of the PCN index by the solar wind, without greatly affecting the unloading contributions. The consequence is that there will be higher correlations between the PC index and AE, AL indices in winter than in summer.

Regarding the evidence of the semiannual peak, it is possible that some contributions arise because variations containing strong signals at frequency f but with a non-sinusoidal structure will contain power at higher order harmonic components at frequencies $2f$, $3f$, etc [e.g. *Shumway and Stoffer*, 2006]. Thus, the peak at 6 months can be attributed partially to higher order harmonic components of the 12 months peak. However, there may be physically important sources of the contribution at $2f$. It has long been recognized that geomagnetic activity follows a semiannual variation, with higher activity during equinox and weaker during solstice. Three theories have been proposed to explain the physical mechanism, the axial hypothesis [*Bohlin*, 1977; *Cortie*, 1912], the equinoctial hypothesis [*McIntosh*, 1959; *Svalgaard*, 1977], and the Russell-McPherron effect [*Russell and McPherron*, 1973]. It is not the purpose of this thesis to evaluate any of the above theories. A semiannual variation of *DUR* of the PCN index is expected; the contribution is to have identified that the relative importance of the dominant currents that produce the polar cap magnetic signature varies systematically with solar cycle and also on shorter time scales.

In order to quantify the mean amplitude of the annual variation, I use a first order approximation through a regression analysis applied to the daily *DUR* time series with $R^2 \geq 0.5$ with pre-determined frequency corresponding to the highest peak in Figure 4.9,

$$DUR = \text{trend} + A_1 \sin(2\pi t/365) + A_2 \cos(2\pi t/365) + \varepsilon_t, \tag{4.14}$$

where the trend is pre-fixed as the solar cycle trend calculated in section 4.2.1, A_1, A_2 are regression coefficients, and ε_t is residual. The use of equation (4.14) is justified by the strength of the signal at a frequency corresponding to one year in Figure 4.9. The fit to the *DUR* obtained from equation (4.14) is shown in Figure 4.10, superposed on the daily variation from Figure 4.4. The ratio peaks in summer, which is consistent with my previous discussion. The magnitude, i.e.

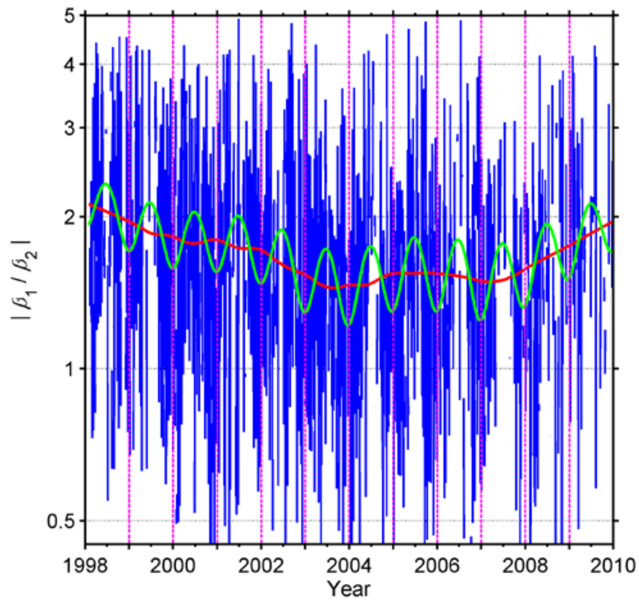

Figure 4.10. As in Figure 4.4 with sinusoidal annual component. Reproduced by permission of American Geophysical Union from *Gao et al.* [2012b].

$A = (A_1^2+A_2^2)^{1/2}$, of the sinusoidal variation is ±0.26. Thus, the summer-winter variation is estimated to be ±15%.

4.3 Discussion and conclusions

In this chapter, I follow the analysis of Chapter 2 which decomposed the PCN index into two primary components, a directly driven component proportional to the electric field of *Kivelson and Ridley* [2008] ($E_{K\text{-}R}$) and an unloading component, linked to the auroral AL index and quantified as AL_U through a linear regression in equation (4.1). I apply the analysis on a daily basis from 1 February 1998 to 31 December 2006 to encompass solar cycle 23. Then I statistically study the variation of driven and unloading contribution to the PCN index by defining the driven-to-unloading ratio (*DUR*) (equation (4.2)) and analyzing its properties on different time scales. I find that the *DUR* varies systematically over solar cycle 23. As solar activity increases, the *DUR* decreases; when solar activity decays, the *DUR* increases.

It is tempting to put forward possible explanations of the results of the statistical analysis. Here I provide suggestions that have not been fully tested but provide explanations of the results that I believe are plausible. I explain the non-intuitive finding regarding the change through the solar cycle of the relative contributions of a driven component and an unloading component in terms of a nonlinear relation between AL_U and $E_{K\text{-}R}$. I relate the latter quantities by the nonlinear form shown in equation (4.5), where both $\Sigma_{E\text{-}P}$ and $E_{K\text{-}R}$ are enhanced in a high-speed stream. If $\Sigma_{E\text{-}P} \propto P_e^{1/2}$ as suggested by *Østgaard et al.* [2002], $\Sigma_{E\text{-}P}$ increases in association with stronger high-speed streams in the solar wind as solar activity approaches maximum and peaks slightly after the solar maximum [*Emery et al.*, 2009], causing a decrease in *DUR*. Then, *DUR* recovers following the decrease of P_e, or equivalently $\Sigma_{E\text{-}P}$.

Strong annual variation of *DUR* is also identified and attributed to the differences in the dominant source of EUV conductance in the polar cap and in the auroral zone. The *DUR* peaks in summer and decreases in winter, because in summer the Hall conductance, Σ_H, caused by solar illumination is expected to increase as the solar zenith angle decreases [e.g. *Robinson and Vondrak,* 1984], and thus, stronger Hall currents are likely to be induced in summer, which results in stronger control of the PCN index by the solar wind. The auroral zone conductance linked to electron precipitation also varies with season, but is likely to be less important in tuning the driven and unloading contributions to the PCN index. Thus, due to higher Hall conductance resulting from enhanced solar illumination, a higher *DUR* in summer than in winter can be understood [*Robinson and Vondrak*, 1984; *Vennerstrøm et al.*, 1991].

The driven, unloading processes are very complicated solar wind-magnetosphere-ionosphere coupling processes that are not likely to be fully described in terms of variations within a solar cycle and annual variations. As seen from Figure 4.4, only part of the variance of *DUR* can be understood as the sum of variations within a solar cycle and annual variations. I have not fully identified all the factors that contribute to *DUR* in controlling polar cap dynamics, but I believe that this statistical study of the polar cap response to solar wind and magnetotail drivers will provide a useful basis for future studies of polar cap dynamics.

CHAPTER 5

Two Cross Polar Cap Potential Saturation Models Compared: Kivelson-Ridley Model versus Siscoe-Hill Model

5.1 Introduction

The cross polar cap potential (Φ_{PC}) measures the rate of magnetic flux transfer from the solar wind to the magnetosphere. It is widely regarded as an important parameter in characterizing the coupling between solar wind and magnetosphere. It is found that the cross polar cap potential increases linearly with the solar wind electric field under nominal solar wind conditions. For example, *Boyle et al.* [1997] empirically obtained a formula which linearly relates Φ_{PC} measured by Defense Meteorological Satellite Program (DMSP) to the solar wind parameters through

$$\Phi_{PC}[\mathrm{kV}] \approx 10^{-7} v[\mathrm{km/s}]^2 + 11.7 B[\mathrm{nT}] \sin^3\theta/2, \tag{5.1}$$

where Φ_{PC} is in kV, v is the solar wind velocity in km/s, and B is the IMF magnitude in nT. *Boyle et al.* [1997] attributed the 1st term to the viscous interaction between the solar wind and the magnetosphere through the low-latitude boundary layer, i.e.,

$$\Phi_{vis}[\mathrm{kV}] \approx 10^{-7} v[\mathrm{km/s}]^2, \tag{5.2}$$

and the 2nd term to the low-latitude magnetic reconnection, i.e.,

$$\Phi_{rec}[\mathrm{kV}] \approx 11.7 B[\mathrm{nT}]\sin^3\theta/2. \tag{5.3}$$

Previous studies found that, under nominal solar wind conditions, Φ_{PC} predicted from equation (5.1) agrees reasonably well with observations [e.g. *Boyle et al.*, 1997]. However, Φ_{PC} asymptotes to a constant value of the order 200 kV for large electric field, or saturates [e.g. *Russell et al.*, 2000], instead of increasing linearly as predicted by equation (5.1). The saturation of Φ_{PC} is consistent with observations [*Nagatsuma*, 2002a; *Shepherd et al.*, 2002; *Hairston et al.*, 2003; *Ober et al.*, 2003] and is found to occur in MHD simulations [*Raeder et al.*, 2001; *Siscoe et al.*, 2002; *Merkine et al.*, 2003]. Several models were proposed to explain the saturation of Φ_{PC} [*Siscoe et al.*, 2002; *Kivelson and Ridley*, 2008; *Borovsky et al.*, 2009]. However, the saturation mechanism is still under debate. *Borovsky et al.* [2009] compared several saturation models and categorized them as reconnection and post-reconnection models. The reconnection models, with details varying, explain the reduced potential as being caused by a reduction of the dayside reconnection rate. In contrast, the post-reconnection model of *Kivelson and Ridley* [2008] explains the reduced potential in terms of processes occurring on the newly reconnected field lines.

The most extensively studied reconnection model is presented by *Siscoe et al.* [2002; 2004], herein referred as the Siscoe-Hill model [*Hill et al.*, 1976; *Siscoe et al.*, 2002; 2004]. The Siscoe-Hill model explains the saturation of Φ_{PC} as a result of the feedback of the Region-1 field-aligned current. Under extreme solar wind driving, the magnetic field generated by the Region-1 current becomes comparable to and opposes the Earth's dipole field at the magnetopause where reconnection occurs. By significantly weakening the field that is reconnecting, the Region-1 current ultimately limits the reconnection rate, resulting in the saturation of Φ_{PC} [*Siscoe et al.*, 2002].

Hill et al. [1976] argued that, for any given solar wind reconnection electric field, the cross polar cap potential is determined by the interplay between an unsaturated trans-magnetospheric potential (Φ_M) and a saturated transpolar potential (Φ_S). Φ_M is the potential drop around the magnetopause that results from magnetic reconnection in the absence of the saturation mechanism. This is an idealized potential in that the model assumes that it increases linearly with the reconnection electric field ($E_{K\text{-}L}$) [*Kan and Lee,* 1979], i.e.,

$$\Phi_M \propto E_{K\text{-}L}, \tag{5.4}$$

even into the saturation domain where, according to the model, the real reconnection potential drop saturates. Φ_S is the transpolar potential that generates Region-1 current strong enough to prevent any further increase in the reconnection rate by creating an opposing magnetic field at the reconnection site. *Hill et al.* [1976] expressed the interplay between Φ_M and Φ_S by combining them as

$$\Phi_{S\text{-}H} = \Phi_M \, \Phi_S \,/\, (\Phi_M + \Phi_S). \tag{5.5}$$

Under nominal solar wind conditions,

$$\Phi_M \ll \Phi_S. \tag{5.6}$$

Thus,

$$\Phi_{S\text{-}H} \approx \Phi_M. \tag{5.7}$$

However, at high levels of geomagnetic activity, Φ_M increases to such an extent that

$$\Phi_M \gg \Phi_S, \tag{5.8}$$

and thus,

$$\Phi_{S\text{-}H} \approx \Phi_S. \tag{5.9}$$

$\Phi_{S\text{-}H}$ saturates for such intervals. *Siscoe et al.* [2002] adopted and extended the results of *Hill et al.* [1976] by relating Φ_M and Φ_S to solar wind and ionospheric parameters. *Siscoe et al.* [2002]

applied the magnetic reconnection theory to the magnetopause and obtained an analytical formula for Φ_M as

$$\Phi_M = 1.82\times10^6 E_{K\text{-}L}\, p^{-1/6}, \tag{5.10}$$

where $E_{K\text{-}L}$ is the reconnection electric field and p is the solar wind pressure in SI units. In the following analysis, the parameters are in SI units. p, in equation (5.10), includes both the dynamic pressure (p_{dyn}) and the magnetic pressure (p_{mag}), i.e.,

$$p = p_{dyn} + p_{mag} = \rho u^2 + B^2/2\mu_0, \tag{5.11}$$

where ρ is the solar wind mass density, B is the IMF magnitude, and μ_0=4π×10^{-7}H/m is the permeability of free space. This is because, although typically $p_{mag} \approx 19$ pPa and $p_{dyn} \approx 2.6$ nPa, i.e.,

$$p_{mag} \ll p_{dyn}, \tag{5.12}$$

p_{mag} can become comparable to p_{dyn} during a storm interval, i.e.,

$$p_{mag} \approx p_{dyn}. \tag{5.13}$$

The analytic formula of Φ_S is derived based on the magnetic field generated by the Region-1 current and is given by

$$\Phi_S = 4.61\times10^9 p^{1/3} / \xi\Sigma_P, \tag{5.14}$$

where Σ_P, fixed at 10 S, is the ionospheric Pedersen conductance, and ξ is a coefficient of the geometry of current flow lines in the ionosphere. An empirical equation given by *Siscoe et al.* [2002] relates ξ to Σ_P through

$$\xi \approx 4.45 - 1.08\log_{10}\Sigma_P. \tag{5.15}$$

From equation (5.15), ξ is between 3 and 4, and is not sensitive to Σ_P. When Σ_P = 10 S, ξ = 3.37, which is the value used in the following analysis. To emphasize,

$$\xi\,|_{\Sigma_P = 10\text{ S}} = 3.37. \tag{5.16}$$

By substituting equation (5.10) and equation (5.14) into equation (5.5), the analytic formula of the Siscoe-Hill model is obtained, i.e.,

$$\Phi_{S\text{-}H} = \Phi_{vis} + 1.82\times10^6 E_{K\text{-}L}\, p^{1/3} / (p^{1/2} + 4\times10^{-4}\xi\Sigma_P E_{K\text{-}L}), \tag{5.17}$$

where a viscous term has been added.

The model of *Kivelson and Ridley* [2008], i.e. Kivelson-Ridley model, is considered as a post-reconnection model because it places no constraints on the reconnection efficiency or the magnetospheric geometry. *Kivelson and Ridley* [2008] argued that when the impedance of the solar wind across polar cap field lines dominates the impedance of the ionosphere, the Alfvén waves incident from the solar wind are partially reflected, reducing the signal in the polar cap. The ratio of the cross polar cap electric field ($E_{K\text{-}R}$) to the reconnection electric field ($E_{K\text{-}L}$) is $2\Sigma_A/(\Sigma_P + \Sigma_A)$, i.e.,

$$E_{K\text{-}R} = E_{K\text{-}L}\, 2\Sigma_A/(\Sigma_P + \Sigma_A), \tag{5.18}$$

where Σ_P is the ionospheric Pederson conductance taken as 10 S, and Σ_A is the Alfvén conductance of the solar wind. Under nominal solar wind conditions, the solar wind Alfvén conductance is $\Sigma_A \approx 16$ S. With $\Sigma_P \approx 10$ S [*Kivelson and Ridley*, 2008], $E_{K\text{-}R}$ is slightly larger than but close to $E_{K\text{-}L}$, i.e.,

$$E_{K\text{-}R} \approx 1.2\, E_{K\text{-}L}. \tag{5.19}$$

Under intense solar wind driving, Σ_A decreases to such an extent that

$$\Sigma_A < \Sigma_P. \tag{5.20}$$

Therefore,

$$E_{K\text{-}R} < E_{K\text{-}L}. \tag{5.21}$$

Then, the cross polar cap potential is calculated from

$$\Phi_{K\text{-}R} = \Phi_{vis} + E_{K\text{-}R} D, \tag{5.22}$$

where D is defined as the distance across the unperturbed solar wind containing field lines that reconnect as they encounter the dayside of the magnetosphere. D is taken to be proportional to the distance to the nose of the magnetopause (R_{mp}),

$$D = 0.1R_{mp}, \tag{5.23}$$

where R_{mp} is calculated from

$$R_{mp} = [(2B_0)^2 / 2\mu_0 p]^{1/6} R_E, \tag{5.24}$$

where $B_0 = 30.4$ μT is the equatorial surface field of the Earth. Thus, the analytic formula given by the Kivelson-Ridley model is

$$\Phi_{K\text{-}R} = \Phi_{vis} + 1.35\times10^6\, E_{K\text{-}L}\, p^{-1/6} \Sigma_A/(\Sigma_A+\Sigma_P), \tag{5.25}$$

where

$$0.2\pi[(2B_0)^2/2\mu_0]^{1/6} R_E = 1.35\times10^6 \tag{5.26}$$

has been substituted.

In this chapter, I explore the similarity and difference between those two models, and compare the model predictions with measurements. In section 5.2, I compare equation (5.17) with equation (5.25) in the saturation limit. It is found that, except for some trivial differences, equation (5.17) is practically the same as equation (5.25) in the saturation limit. In section 5.3, using the same cases as *Gao et al.* [2012c], the model predictions are compared to the measurements of AMIE, DMSP, the PC index, and SuperDARN. Since different measurements give very different values, but the model predictions are close, it is impossible to show that one model is better than the other by comparing the predictions with the measurements.

5.2 A formula of $\Phi_{S\text{-}H}$ similar to $\Phi_{K\text{-}R}$

In this section, I compare equation (5.17) with equation (5.25) under general solar wind conditions. First, notice that by defining

$$F = 2.5\times10^3 p^{1/2} / \xi E_{K\text{-}L}, \tag{5.27}$$

equation (5.17) can be written as

$$\Phi_{S\text{-}H} = \Phi_{vis} + 1.82\times10^6 E_{K\text{-}L}\, p^{-1/6}\, F / (F+\Sigma_P). \tag{5.28}$$

The difference between equation (5.28) and equation (5.25) lies in the difference between F and Σ_A. Let

$$F = 0.74\eta\Sigma_A, \tag{5.29}$$

where $\eta = F / 0.74\Sigma_A$ can be computed from

$$\eta = (1+p_{mag}/p_{dyn})^{1/2}\, (B/B_{YZ}) \sin^{-2}\theta/2. \tag{5.30}$$

Thus, η varies between 1 and ∞, i.e.,

$$\eta \in (1, \infty). \tag{5.31}$$

In equation (5.30), ξ is estimated by substituting Σ_P = 10 S in equation (5.15), i.e., $\xi = 3.37$. In summary,

$$\Phi_{S\text{-}H} = \Phi_{vis} + 1.34\times10^6 E_{K\text{-}L}\, p^{-1/6}\, \eta\Sigma_A / (0.74\eta\Sigma_A + \Sigma_P). \tag{5.32}$$

Thus, the challenge is to distinguish the above equation from

$$\Phi_{K\text{-}R} = \Phi_{vis} + 1.35\times10^6\, E_{K\text{-}L} p^{-1/6}\, \Sigma_A / (\Sigma_A + \Sigma_P). \tag{5.33}$$

The saturation of cross polar cap potential often occurs during a magnetic storm driven by a coronal mass ejection (CME) [e.g. *Kivelson and Ridley*, 2008], during which Σ_A can decrease to such an extent that $\Sigma_A \ll \Sigma_P$. In this limit,

$$\Sigma_A + \Sigma_P \approx \Sigma_P, \text{ and } 0.74\Sigma_A + \Sigma_P \approx \Sigma_P. \tag{5.34}$$

Besides, in a CME-driven magnetic storm, B_Z is negative and usually dominates over both B_X and B_Y, i.e.,

$$|B_Z| \gg |B_Y|, \text{ and } |B_Z| \gg |B_X|. \tag{5.35}$$

Thus,

$$B/B_{YZ} \approx 1, \text{ and } \sin^{-2}\theta/2 \approx 1. \tag{5.36}$$

Besides, if

$$1 + p_{\mathrm{mag}}/p_{\mathrm{dyn}} \approx 1, \text{ or } p \approx p_{\mathrm{dyn}}, \tag{5.37}$$

is assumed (see Figure 5.3), then

$$\eta \approx 1. \tag{5.38}$$

Ignoring the viscous term, $\Phi_{\text{S-H}}$ and $\Phi_{\text{K-R}}$ become

$$\Phi_{\text{S-H}} \approx 1.20\times10^9 p^{1/3}/\Sigma_{\mathrm{P}}, \text{ and } \Phi_{\text{K-R}} \approx 1.20\times10^9 p^{1/3}/\Sigma_{\mathrm{P}}. \tag{5.39}$$

Thus,

$$\Phi_{\text{S-H}} \approx \Phi_{\text{K-R}}. \tag{5.40}$$

In equation (5.39),

$$E_{\text{K-L}}\Sigma_{\mathrm{A}} = (uB_{YZ}\sin^2\theta/2)\,(\rho^{1/2}/B\mu_0^{1/2}) \approx 892p^{1/2} \tag{5.41}$$

has been used. Thus, in most cases the Siscoe-Hill model and the Kivelson-Ridley model predict similar saturated potentials. In order to obtain significantly different predictions from the two models, η needs to be larger than 1, for which either a large B_X or B_Y component must be present, or p_{mag} must be comparable to p_{dyn}.

5.3 Comparing model predictions with measurements

Four techniques are commonly used to measure ionospheric quantities including Φ_{PC}: (1) Assimilative Mapping of Ionospheric Electrodynamics (AMIE) [*Richmond and Kamide*, 1998;

Richmond et al., 1988], (2) Defense Meteorological Satellite Program (DMSP) [*Hairston et al.*, 1998], (3) polar cap index [*Troshichev et al.*, 1988] and (4) Super Dual Auroral Radar Network (SuperDARN) [*Ruohoniemi and Baker*, 1998].

The DMSP instruments measure the cross-track ion drift velocity $\boldsymbol{v}_\perp$ and using that to calculate the electric field along the spacecraft trajectory from

$$\boldsymbol{E}_{/\!/} = -\boldsymbol{v}_\perp \times \boldsymbol{B}, \tag{5.42}$$

where $\boldsymbol{B}$ is the local magnetic field taken as the International Geomagnetic Reference Field (IGRF). The electric potential along the spacecraft trajectory is computed as

$$\Phi(s) = \int_l E_{/\!/}\, ds, \tag{5.43}$$

where l stands for the DMSP trajectory in the polar cap region, and s is a point on the spacecraft trajectory. Φ_{PC} is estimated by the difference between potential extrema, i.e.,

$$\Phi_{PC} \approx \max \Phi(s) - \min \Phi(s). \tag{5.44}$$

The DMSP F-13 satellite used in this study has a trajectory primarily along the dawn-dusk direction, which is desirable for measuring Φ_{PC}. However, this trajectory still rarely passes over the true potential maximum and minimum. Thus, the potential given by DMSP can be systematically smaller than the true value. Besides, it normally takes from 12 to 20 minutes for DMSP to cross the polar cap region, during which the value of Φ_{PC} may change significantly.

The PC index, derived from the surface magnetic field perturbation [*Troshichev et al.*, 1988], responds directly to the solar wind driving [e.g. *Gao et al.*, 2012a; 2012b; 2012c]. *Troshichev et al.* [1996] compared the PC index with Φ_{PC} measured by EXOS-D satellite and found

$$\Phi_{PC}[\mathrm{kV}] \approx 19.35\mathrm{PC} + 8.78. \tag{5.45}$$

Ridley and Kihn [2004] took seasonal variation into account and gave a different formula to convert from the PC index to Φ_{PC} measured by AMIE, i.e.,

$$\Phi_{PC}[\mathrm{kV}] \approx 29.28 - 3.31\sin(T + 1.49) + 17.81\mathrm{PC}, \tag{5.46}$$

where T is the month of the year normalized to 2π, i.e.,

$$T = (\mathrm{month} - 1) \times 2\pi/12. \tag{5.47}$$

For example, January = 0, July = $6 \times 2\pi/12$, December = $11 \times 2\pi/12$ [*Ridley and Kihn*, 2004]. However, since the PC index does not directly measure Φ_{PC}, the two equations above are correct fits to the AMIE potential values. In addition, the PC index can take on a negative value [*Nagatsuma*, 2002b], which may result in a negative prediction of Φ_{PC}. Thus, there are intervals during which equation (5.45) and equation (5.46) fail.

SuperDARN measures line-of-sight ionospheric convection velocities with a ground-based network of radars and then infers functional forms of the electrostatic potential [*Ruohoniemi and Baker*, 1998]. The electrostatic potential, as a function of co-latitude and longitude, is expressed as a truncated expansion of spherical harmonic functions. Then, the expansion coefficients are estimated to give the best consistency between the measured line-of-sight velocity and that predicted from the harmonic expansion. The cross polar cap potential is computed from the difference between the extrema of the electrostatic potential inferred from the expansion. It is believed that the main limitation of using ground-based radars to measure Φ_{PC} lies in the radars' limited field of view. For the large fields present when saturation occurs, the polar cap can expand out of the SuperDARN radars' field of view, which can result in an underestimate of Φ_{PC} [e.g. *Shepherd et al.*, 2002].

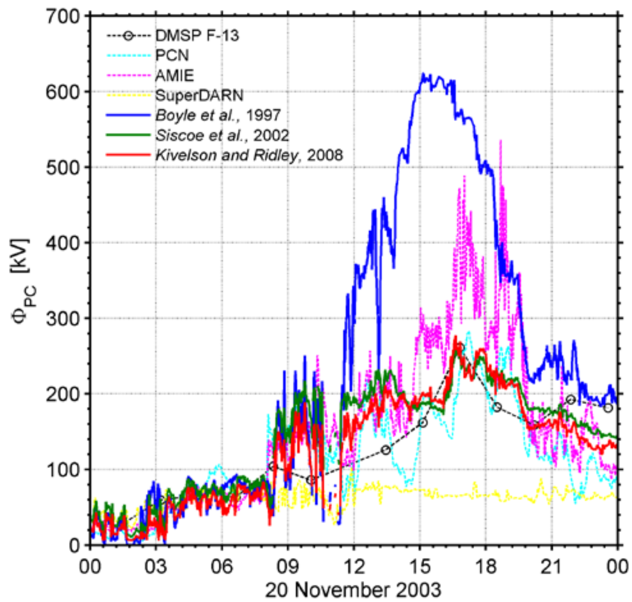

Figure 5.1. The cross polar cap potential (Φ_{PC}) on 20 November 2000. The blue line is Φ_{PC} computed from equation (5.1). The green line is $\Phi_{S\text{-}H}$. The red line is $\Phi_{K\text{-}R}$. The black dashed line with circles is Φ_{PC} measured by DMSP. The cyan line is Φ_{PC} converted from PC index using the formula of *Troshichev et al.* [1996]. The magenta line is Φ_{PC} measured by AMIE. The yellow line is Φ_{PC} measured by SuperDARN.

AMIE assimilates many types of data from both ground-based and space-based instruments and produces estimates of several ionospheric parameters including Φ_{PC}. It is a technique for mapping high-latitude electric fields and currents and their associated magnetic variations from sets of localized observational data including magnetic field data from ground magnetometers and electric field data from radars and satellites [*Ridley and Kihn*, 2004]. The algorithm of AMIE, like that of SuperDARN, also fits a truncated harmonic expansion of electrostatic potential to observations [*Richmond and Kamide*, 1988; *Matsuo et al.*, 2005]. Although the results of this technique are thought to represent flows and perturbation fields well, *a priori* knowledge of the ionospheric Hall conductance (Σ_H) is required when magnetometer

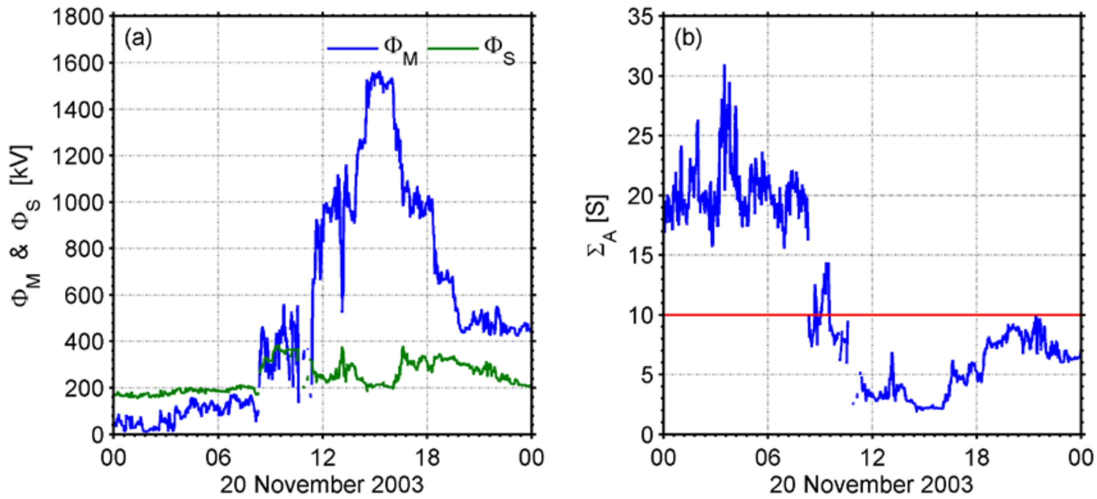

Figure 5.2. The parameters of Siscoe-Hill model and Kivelson-Ridley model on 20 November 2003. (a) The trans-magnetospheric potential Φ_M (equation (5.10)) and the transpolar potential Φ_S (equation (5.14)); (b) the Alfvén conductance of the solar wind, Σ_A. The red line in panel (b) labels 10 S, which is the value of Σ_P used in this thesis.

observations are used. It has been suggested that incorrect Hall conductance estimates during extreme conditions can lead to incorrect predictions of Φ_{PC} with the AMIE technique [*Ridley and Kihn*, 2004]. See *Gao* [2012a] for the difference between the algorithms of AMIE and SuperDARN.

Using the events listed in Table 2.1, I compare the potentials predicted from equation (5.17) and equation (5.25) with the measurements. Figure 5.1 shows the interval on 20 November 2003 that is discussed in Chapter 2. Φ_{PC} predicted from equation (5.1), equation (5.17), and equation (5.25) are displayed in the blue line, the green line and the red line, respectively. Φ_{PC}'s measured by the aforementioned techniques are also plotted. For convenience,

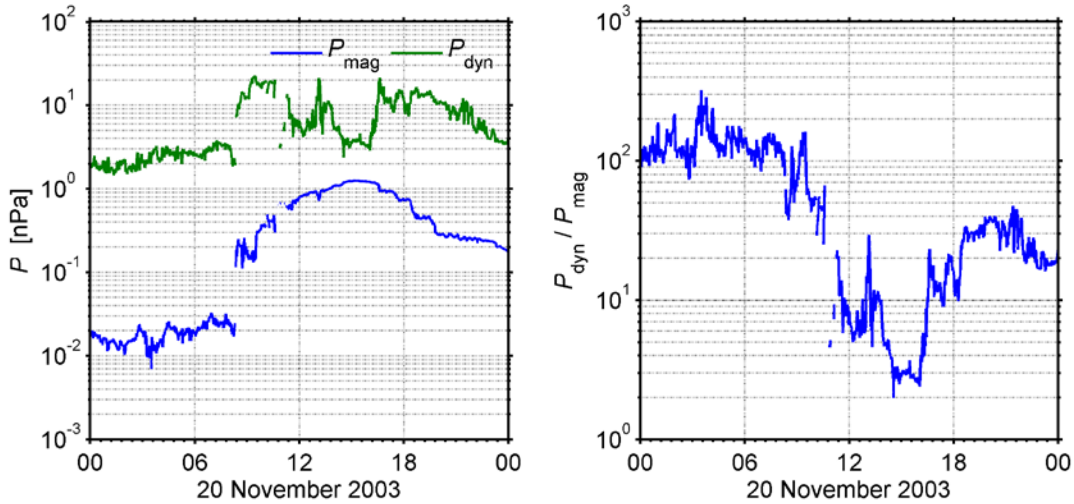

Figure 5.3. The magnetic pressure, p_{mag}, and dynamic pressure, p_{dyn}, on 20 November 2003. (a) p_{mag} and p_{dyn} versus time; (b) the ratio between p_{dyn} and p_{mag} versus time. The *Y* axes are in logarithmic scales.

I define saturation as the time interval during which the formula of *Boyle et al.* [1997] (equation (5.1)) over-predicted Φ_{PC} by at least 100 kV compared to the 2^{nd} largest prediction or measurement, which was between 11:00 UT and 20:00 UT for this case. From Figure 5.1, it is clear that, during the saturation interval, different techniques can give quite different measurements. For example, Φ_{PC} measured by SuperDARN is significantly lower than the values obtained from other techniques. However, the model predictions, $\Phi_{S\text{-}H}$ and $\Phi_{K\text{-}R}$, agree well with each other.

As argued by *Siscoe et al*. [2002], the trans-magnetospheric potential Φ_M dominated the transpolar potential Φ_S during the saturation interval (Figure 5.2 (a)). Thus, in this interval, $\Phi_{S\text{-}H}$ was almost equal to Φ_S. In the meantime, as seen from Figure 5.2 (b), Σ_A decreased to such an

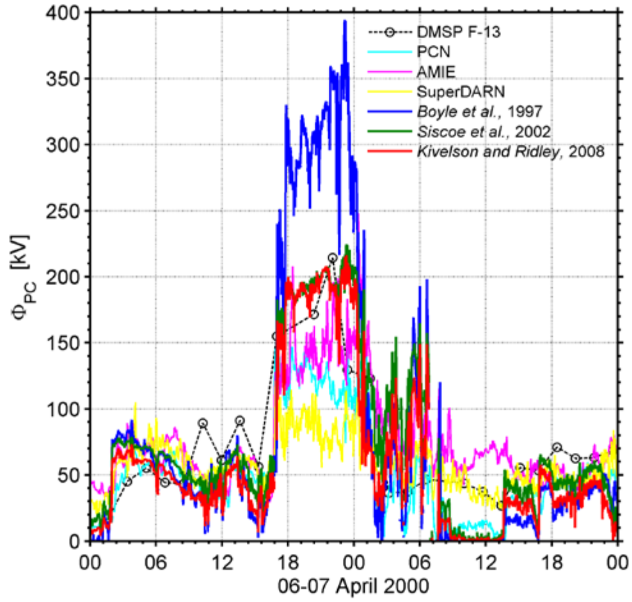

Figure 5.4. As in Figure 5.1 for a different case on 6-7 April 2000.

extent that $\Sigma_A < \Sigma_P$ was satisfied as suggested by *Kivelson and Ridley* [2008]. Therefore, $E_{K\text{-}R}$ became smaller than $E_{K\text{-}L}$.

Figure 5.3 compares the magnetic pressure, p_{mag}, with the dynamic pressure, p_{dyn}, for this case. As seen from Figure 5.3 (a), on 20 November 2003, p_{dyn} was always larger than p_{mag}. The ratio, p_{dyn}/p_{mag}, was close to 100 during the non-saturation interval (00:00 UT to 09:00 UT in Figure 5.3 (b)). Even though, during the saturation interval, the ratio decreased, it remained above 3. Thus, it is legitimate to assume that equation (5.37) is satisfied, and that similar predictions from equations (5.17) and (5.25) can be expected.

Another case on 6-7 April 2000 is shown in Figure 5.4. The formula of *Boyle et al*. [1997] over-predicted Φ_{PC} in the interval between 18:00 UT and 24:00 UT on 6 April 2000. Similar to the previous case, $\Phi_{S\text{-}H}$ was close to $\Phi_{K\text{-}R}$, while discrepancies among observations were found

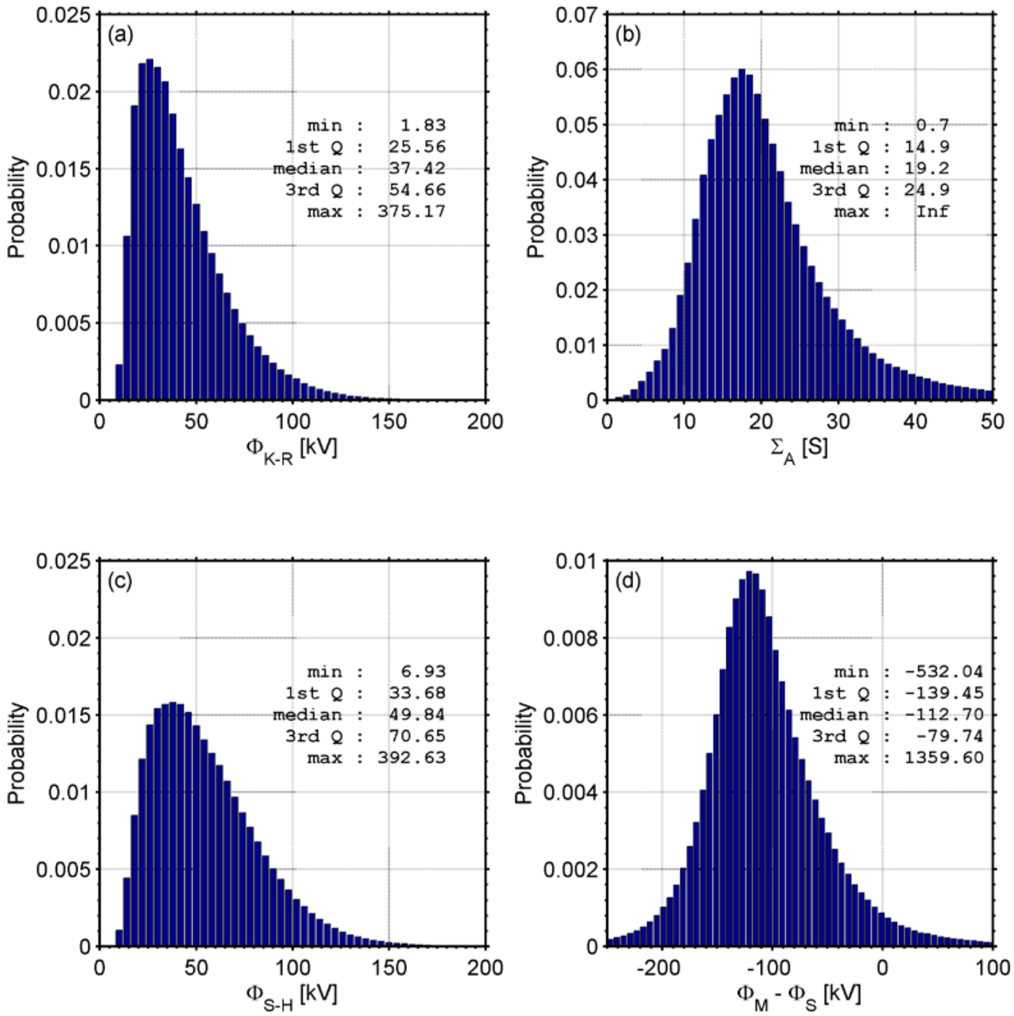

Figure 5.5. Histograms of (a) Φ_{K-R}, (b) Σ_A, (c) Φ_{S-H}, and (d) $\Phi_M - \Phi_S$ for 1 minute solar wind observation from 1999 to 2009. The text in a panel shows the summary statistics of the plotted quantity. For example, in panel (a), Φ_{K-R} is summarized as: minimum, 1.83; 1st quartile, 25.56; median, 37.42; 3rd quartile, 54.66; maximum, 375.17.

during the saturation interval. A detailed examination of the other events of *Gao et al*. [2012c] supports the above argument. As before the SuperDARN measurement appears to underestimate Φ_{PC} in a saturation interval. However, it is plotted for completeness.

Using 1 minute observations from the Advanced Composition Explorer (ACE) to evaluate equation (5.25), the histogram of $\Phi_{K\text{-}R}$ from 1999 to 2009 is shown in Figure 5.5 (a). The probability mass concentrates around 30 kV and predicted values larger than 150 kV rarely occur. *Kivelson and Ridley* [2008] argue that saturation occurs when the impedance of solar wind dominates that of the ionosphere, i.e. equation (5.20). With Σ_P fixed at 10 S, this saturation criterion is met 6% of the time (Figure 5.5 (b)). In Figure 5.5 (c), the histogram of $\Phi_{S\text{-}H}$ is displayed. Compared to Figure 5.5 (a), $\Phi_{S\text{-}H}$ is likely to take on a value larger than $\Phi_{K\text{-}R}$. *Siscoe et al*. [2002] argued that when the trans-magnetospheric potential (Φ_M) dominates the transpolar potential (Φ_S), saturation occurs, which results in the saturation criterion $\Phi_M > \Phi_S$. For the solar wind observation from 1999 to 2009, this criterion is satisfied 4% of the time (Figure 5.5 (d)).

The difference between $\Phi_{K\text{-}R}$ and $\Phi_{S\text{-}H}$ is systematically examined by studying

$$\Delta = \Phi_{K\text{-}R} - \Phi_{S\text{-}H} \tag{5.48}$$

from 1999 to 2009. The histogram of Δ is shown in Figure 5.6 (a). Notice that the distribution of Δ is strongly biased toward the negative end, which means that, in general,

$$\Phi_{K\text{-}R} \leq \Phi_{S\text{-}H}. \tag{5.49}$$

The probability mass of Δ concentrates around 10 kV, i.e.,

$$\Phi_{S\text{-}H} \approx \Phi_{K\text{-}R} + 10 \text{ kV}. \tag{5.50}$$

Given the uncertainties of the measurements, such a difference (10 kV) is not large enough to differentiate the two models. The conditional distribution of Δ under

$$\Phi_M > \Phi_S \tag{5.51}$$

is shown in Figure 5.6 (b). Compared to Figure 5.6 (a), the difference between $\Phi_{K\text{-}R}$ and $\Phi_{S\text{-}H}$ is more likely to take on a large (negative) value. The criterion,

$$\Sigma_A < 10 \text{ S}, \tag{5.52}$$

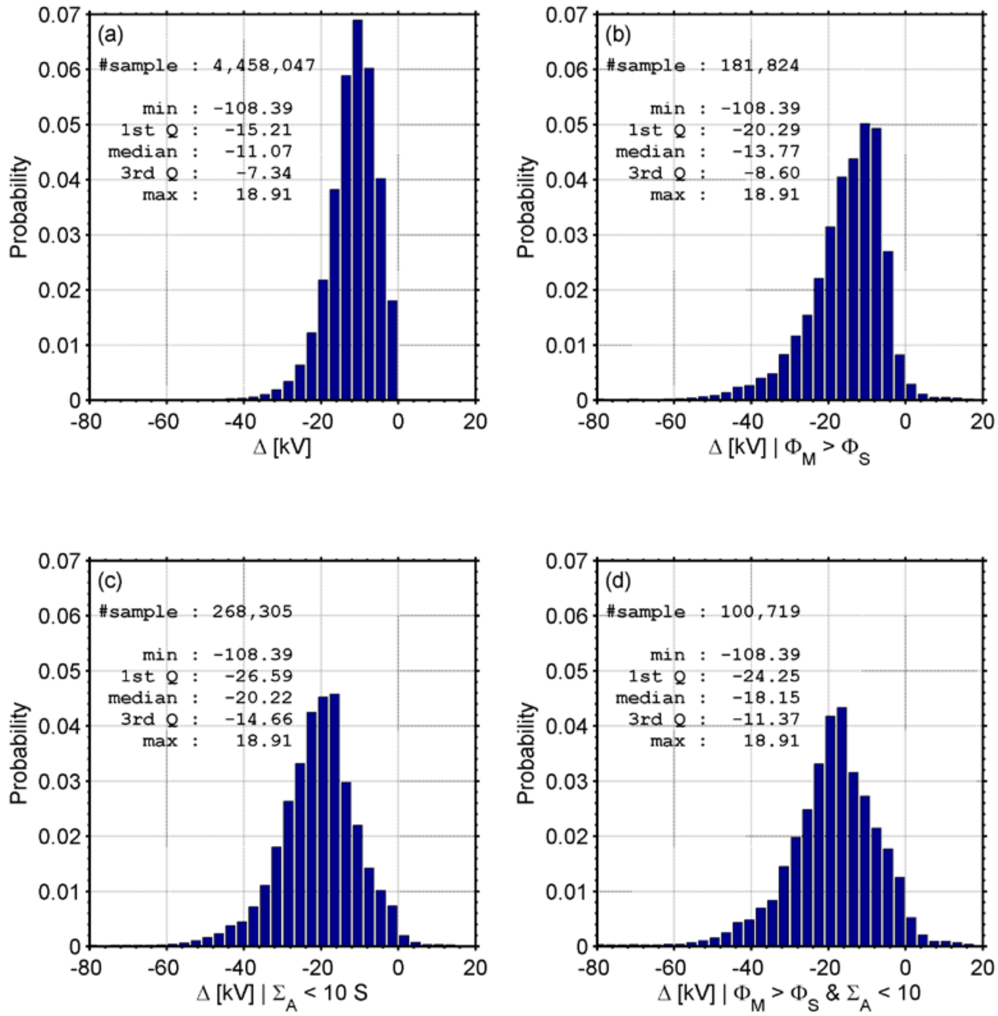

Figure 5.6. Histograms of (a) Δ, (b) a subset of Δ satisfying $\Phi_M > \Phi_S$, (c) a subset of Δ satisfying $\Sigma_A < 10$ S, and (d) a subset of Δ satisfying $\Phi_M > \Phi_S$ and $\Sigma_A < 10$ S for 1 minute solar wind observation from 1999 to 2009. The text in a panel shows the summary statistics of the plotted quantity.

can be used instead, whose result is shown in Figure 5.6 (c). Figure 5.6 (d) shows the distribution of Δ when both criteria are used. With a saturation criterion (Figure 5.6 (b), (c), or (d)), the magnitude of difference is likely to be larger than without one. However, there are still few cases

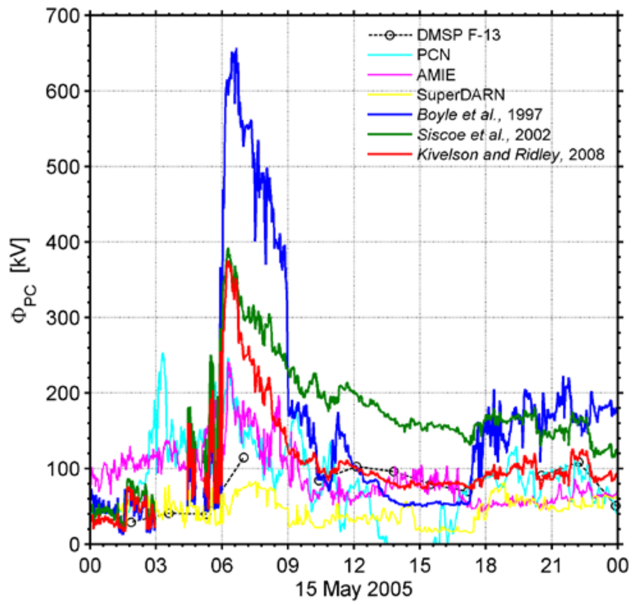

Figure 5.7. As in Figure 5.1 for a different case on 15 May 2005.

for which $\Phi_{K\text{-}R}$ differs from $\Phi_{S\text{-}H}$ considerably. For example, in the decade analyzed, there is only one case, on 15 May 2005, with intervals during which

$$|\,\Delta\,| > 100 \text{ kV}. \tag{5.53}$$

The case of 15 May 2005 is shown in Figure 5.7. After 06:00 UT, the difference between $\Phi_{S\text{-}H}$ and $\Phi_{K\text{-}R}$ remained close to 100 kV. The reason for the difference between $\Phi_{K\text{-}R}$ and $\Phi_{S\text{-}H}$ is shown in Figure 5.8. Corresponding to the big difference between $\Phi_{K\text{-}R}$ and $\Phi_{S\text{-}H}$ during the interval with $\Sigma_A < \Sigma_P$ (Figure 5.8 (a)), η differs substantially from 1 (Figure 5.8 (b)) due to the IMF geometry (Figure 5.8 (c)), for which $B/B_{YZ}\sin^{-2}\theta/2$ became large (Figure 5.8 (d)). Although p_{mag} was close to p_{dyn} at around 10:00 UT, the ratio of p_{mag} to p_{dyn} remained below 1 (Figure 5.8 (e)), and thus, did not contribute to η significantly. Besides, after 06:00 UT, Σ_A was much smaller than Σ_P, i.e., $\Sigma_A \ll \Sigma_P$. Thus, by ignoring the viscous term,

$$\Phi_{K\text{-}R} \approx 1.35\times10^6\, E_{K\text{-}L}\, p^{-1/6}\, \Sigma_A/\Sigma_P, \text{ and, } \Phi_{S\text{-}H} \approx 1.82\times10^6\, E_{K\text{-}L}\, p^{-1/6} = \Phi_M. \tag{5.54}$$

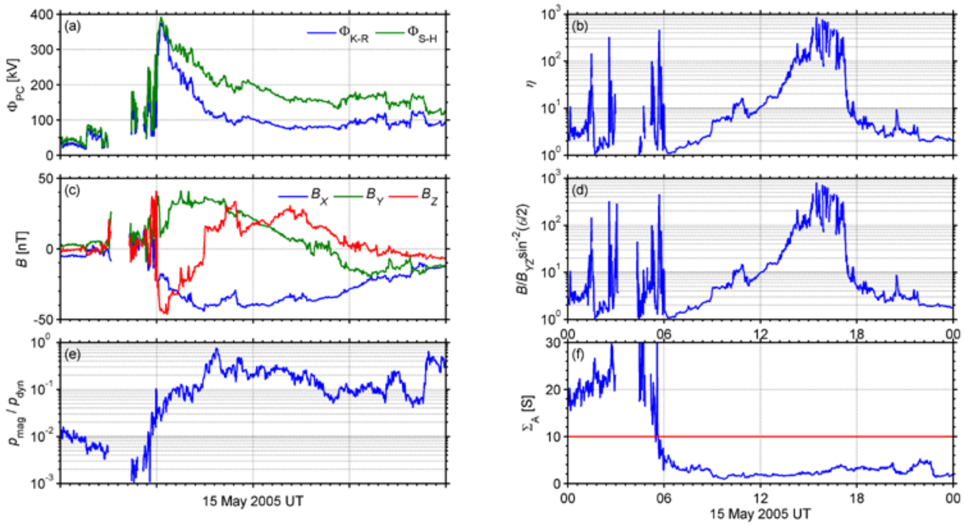

Figure 5.8. The predicted cross polar cap potentials and the relevant parameters on 15 May 2005. Plotted are the time series of (a) $\Phi_{K\text{-}R}$ and $\Phi_{S\text{-}H}$; (b) η (equation(5.30)); (c) IMF in GSM coordinates; (d) $B/B_{YZ}\sin^{-2}\theta/2$; (e) the ratio of p_{mag} to p_{dyn}; (f) the solar wind Alfvén conductance, Σ_A.

In other words, for the interval between 09:00 UT and 18:00 UT when IMF was northward-oriented, the theory of *Kivelson and Ridley* [2008] predicts the saturation of cross polar cap potential, while, according to *Siscoe et al*. [2002; 2004], saturation did not occur. Clearly, after 09:00 UT, the measurements were close to $\Phi_{K\text{-}R}$ in terms of absolute value. However, the measured Φ_{PC} was much smaller than either $\Phi_{S\text{-}H}$ or $\Phi_{K\text{-}R}$ from 06:00 UT to 08:00 UT. One should note that, after 06:00 UT, the time derivative of Φ_{PC} measured by AMIE or PC index was closer to the derivative of $\Phi_{S\text{-}H}$ than the derivative of $\Phi_{K\text{-}R}$ (i.e., $\Phi_{S\text{-}H} - \Phi_{PC} \approx$ const). Thus, even though the two models gave fundamentally different predictions for the case of 15 May 2005, the difference of the predicted values was still not large enough in magnitude to argue that one model is better than the other by directly comparing $\Phi_{S\text{-}H}$ and $\Phi_{K\text{-}R}$ with data.

There are two factors that complicate the comparison between the Siscoe-Hill model and the Kivelson-Ridley model. One is the occurrence of both mechanisms during a given saturation case. The other is the feedback of magnetotail activity. The mechanisms suggested in developing the two models, i.e. feedback of the Region-1 current which reduces the reconnection rate and reflection of the incident electric field which reduces the transmitted electric field, co-occur during a saturation interval. *Siscoe* [2011] argued that the two models probably should be regarded not as different theories but as alternative formulations of the same basic idea. He further argued that the Siscoe-Hill model formulates the basic idea, while the Kivelson-Ridley model gives a specific instance of it. The consistency between the two models during a saturation interval suggests that the process described by *Siscoe et al*. [2002] is likely to be concurrent with that described by *Kivelson and Ridley* [2008]. However, we disagree with *Siscoe* [2011] that the Kivelson-Ridley model gives a specific instance of the Siscoe-Hill model. On 15 May 2005, the Siscoe-Hill model predicts no saturation but the Kivelson-Ridley model predicts saturation after 06:00 UT. In addition, it is difficult to believe that the magnetic field cancellation at the low-latitude magnetopause resulting from the enhanced Region-1 currents is the same as the partial wave reflection on the newly reconnected field line due to the dominance of solar wind impedance over the ionospheric impedance. However, as to the mechanism responsible for the saturation of Φ_{PC}, we believe that one process plays the key role. Unfortunately, the effects of two processes that occur concurrently cannot be identified separately by using existing observations.

Another reason is that neither model predicts the full potential (e.g. Figure 5.1). The cross polar cap potential results from the convective flows in the polar ionosphere. In addition to the convection initiated by the solar wind and IMF, there are other sources of the convective flows that affect the potential. For example, in Chapter 2, I find that the polar cap dynamics also responds to the magnetotail energy unloading, whose contribution is comparable to that of the solar wind driving. Thus, magnetotail activity is expected to contribute significantly to the cross polar cap potential. However, both the Siscoe-Hill model and the Kivelson-Ridley model are driven models, in the sense that they make no attempt to consider the phenomenology of the magnetotail and do not ascribe any particular importance to reconnection in the tail. A direct consequence is that the measured Φ_{PC} is more dynamic than Φ_{PC} predicted by either model (e.g. Figure 5.1), which further complicates the comparison of the two models.

5.4 Discussion and conclusions

It has been noticed in previous studies [e.g. *Lavraud and Borovsky*, 2008*; Siscoe*, 2011] that the cross polar cap potential predicted by *Siscoe et al*. [2002] is similar to that predicted by *Kivelson and Ridley* [2008]. In this chapter, I examine the similarities and differences between the two models mathematically and compare the predictions to the measurements. I find that the mathematical formula of the Kivelson-Ridley model is similar to that of the Siscoe-Hill model. The difference can be summarized in an η factor (equation (5.32) versus equation (5.33)). Using the saturation cases of *Gao et al.* [2012c], I compare the model predictions with the measurements of AMIE, DMSP, PC index and SuperDARN. I find that, as expected, the model predictions are very close to each other, although the measurements from different techniques are quite different. A systematic survey of the difference in model predictions from 1999 to 2009 shows that, on average, $\Phi_{K\text{-}R}$ is smaller than $\Phi_{S\text{-}H}$ by 10 kV. Given the uncertainties of the measurements, such a difference is not large enough to support one model instead of another. There is one exceptional event for which the difference between $\Phi_{S\text{-}H}$ and $\Phi_{K\text{-}R}$ was as large as

100 kV. However, even for this case, it is still not possible to establish that one model is to be preferred over the other by comparing with observations.

Siscoe et al. [2002] propose that it is the feedback of the Region-1 current that reduces the reconnection rate which eventually limits the rate of flux transfer from the solar wind to the magnetotail, resulting in the saturation of Φ_{PC}. However, *Kivelson and Ridley* [2008] argue that the saturation of Φ_{PC} is caused by the reflection of the Alfvén waves incident from the solar wind, when the impedance of the solar wind across the polar cap field lines dominates the impedance of the ionosphere. These two processes co-occur in a saturation interval, and lead to very similar predictions of Φ_{PC}. Thus, it is impossible to tell which is responsible for the saturation of Φ_{PC} from observations.

The contribution from magnetotail activity further complicates the comparison. Besides, polar cap dynamics are significantly influenced by the magnetotail energy unloading, and so is Φ_{PC}. Since both the Siscoe-Hill model and the Kivelson-Ridley model are driven models that do not incorporate magnetotail activity, it is unlikely that either prediction will be fully consistent with measurements. As seen from Figure 5.1, the measured Φ_{PC} is more dynamic than that predicted from the models, an observation that is further confirmed in Figure 5.4 and Figure 5.7.

In summary, since both the processes behind the Siscoe-Hill mechanism and the Kivelson-Ridley mechanism occur during saturation intervals and energy unloading in the magnetotail further complicates a comparison of predictions with data, it is unpromising to directly compare the predictions of the two models with measurements to determine which process is responsible for the saturation of Φ_{PC}.

CHAPTER 6

Conclusions and Future Work

The solar wind-magnetosphere-ionosphere coupling is an important mechanism that governs the earth's ionospheric dynamo. In this thesis, I investigate how polar cap dynamics are coupled to solar wind and magnetotail activity by studying the relation among the PCN index, solar wind-magnetosphere coupling functions and the AL index. I focus on intervals of high geomagnetic activity, during which the data are less influenced by statistical fluctuations and the coupling functions are likely to be different. Four major findings resulted from this thesis include:

1. The electric field of *Kivelson and Ridley* [2008], $E_{\text{K-R}}$, which incorporates a saturation mechanism, generally outperforms other coupling functions in predicting the polar cap magnetic field perturbation at high levels of geomagnetic activity.
2. The magnetotail energy unloading, represented by an unloading AL index, AL_U, makes significant contribution to the polar cap dynamics as represented by the PCN index.
3. The PCN index can be linearly related to its solar wind driver ($E_{\text{K-R}}$) and magnetotail driver (AL_U), i.e., $\text{PCN} \approx \beta_0 + \beta_1 zs(E_{\text{K-R}}) + \beta_2 zs(\text{AL}_\text{U})$, where β_0, β_1 and β_2 are constants over time intervals of a day.

4. Driven contribution relative to the unloading contribution to the PCN index, quantified by driven-to-unloading ratio (*DUR* = $|\beta_1/\beta_2|$), varies with solar cycle and season with enhanced DUR in solar minimum and summer hemisphere.

Chapter 2 presented a study, in which I examined 53 one to two-day intervals that include large PCN-derived cross polar cap potential. It is found that, among 11 candidate coupling functions including the merging electric field of *Kan and Lee* [1979] and universal coupling function of *Newell et al*. [2007], the electric field of *Kivelson and Ridley* [2008] predicts the PCN index through a linear model best. It is also found that the magnetotail energy unloading, as represented by an unloading AL index ($\mathrm{AL_U}$), makes a contribution to the PCN index comparable to that of $E_{\mathrm{K\text{-}R}}$. Besides, the PCN index can be linearly related to $E_{\mathrm{K\text{-}R}}$ and $\mathrm{AL_U}$, i.e., PCN $\approx \beta_0 + \beta_1 zs(E_{\mathrm{K\text{-}R}}) + \beta_2 zs(\mathrm{AL_U})$, where β_0, β_1, and β_2 are constants estimated from regression, and $zs(\cdot)$ is the z-score function. In addition, β_1 is approximately twice as large as β_2, which indicates that the directly driven contribution outweighs the energy unloading contribution by roughly a factor of 2.

Chapter 3 examines the validity of the linear assumption between the PCN index and $E_{\mathrm{K\text{-}R}}$, $\mathrm{AL_U}$. Using the same events as those used in Chapter 2, the results of the linear model are compared to those of the additive model, i.e., PCN $\approx \alpha + f_1(E_{\mathrm{K\text{-}R}}) + f_2(\mathrm{AL_U})$, where α is a constant, and $f_1(\cdot)$, $f_2(\cdot)$ are arbitrary smooth functions. Here, the additive model is more general and non-linear. It is found that the results of the two models are similar to each other, indicating that the linear assumption is generally valid for an interval of a day. However, there are anomalous events during which the auroral oval expanded poleward to the latitude of the PCN station and the index increased because of the auroral zone currents. For such events, the linear model fails.

Chapter 4 applies the linear model to most of the days in solar cycle 23 and studies the relative driven and unloading contribution to the PCN index. A driven-to-unloading ratio (*DUR*) is defined from the linear model, i.e., $DUR = |\beta_1/\beta_2|$, where β_1 and β_2 are regression coefficients of $zs(E_{\text{K-R}})$ and $zs(\text{AL}_\text{U})$. The long-term variations of *DUR* with solar cycle and season were investigated. Near solar maximum, the relative unloading contribution increases because of an enhanced conductance caused by electron precipitation on the nightside. The relative driven contribution increases in summer due to an enhanced Hall conductance resulting from a shorter effective light path.

Chapter 5 compares the saturation model of *Kivelson and Ridley* [2008] with that of *Siscoe et al*. [2002; 2004]. Although $E_{\text{K-R}}$ is successful in explaining the polar cap magnetic disturbance at high levels of geomagnetic activity by taking saturation into account, a competing saturation model of *Siscoe et al*. [2002; 2004] predicts similar results. In Chapter 5, I demonstrate that, in the saturation limit, these two models give almost identical predictions. In addition, the model predictions are compared with measurements (AMIE, DMSP, PC index, and SuperDARN). Unfortunately, given the great uncertainties in measurements, it is impossible to prefer one model over the other.

This thesis provides a useful reference for understanding the coupling among solar wind, magnetosphere and ionosphere. It is also an important first step in exploring the physical mechanism of cross polar cap potential saturation. Since it is not possible to verify a saturation model from measurements, future work will include case studies by using global MHD simulations. One can use real cases used in this thesis and run global MHD simulation on that day. Then, one could examine whether the reconnection rate at the low-latitude magnetopause is lowered by the increased strength of Region-1 currents as suggested by *Siscoe et al.* [2002]. Besides, one can also try to find whether the wave is partially reflected by ionosphere as predicted by *Kivelson and Ridley* [2008]. It is also beneficial to run some ideal cases in which big difference between $\Phi_{\text{K-R}}$ and $\Phi_{\text{S-H}}$ was found. For example, one can set $\eta \gg 1$, and in the meantime, $\eta\Sigma_A \ll \Sigma_P$. In this way, $\Phi_{\text{S-H}} \gg \Phi_{\text{K-R}}$. Then, one can check which model prediction is more consistent with the simulated result.

An interesting prediction of $E_{\text{K-R}}$ is that the solar wind density (n) plays a role in controlling the solar wind-magnetosphere coupling when Σ_A is reasonably small compared to Σ_P. Since if $\Sigma_A \gg \Sigma_P$, $E_{\text{K-R}} \approx 2E_{\text{K-L}}$, which is independent of n. This can be the reason why some coupling functions have density dependence, while others do not. A quick examination would pick intervals of small Alfvén conductance and check the consistency between the PCN index and solar wind density. In contrast, a data set of large Alfvén conductance should also be construct, for which the consistency between the PCN index and n is also examined. If $E_{\text{K-R}}$ is the coupling function that controls the polar cap activity, it is expected to see a good consistency between n and the PCN index for the data set with small Σ_A, but not for the data set with large Σ_A.

Another interesting topic is the annual variation of the PCN index. It is claimed that the PCN index is not influenced by the Hall conductance [*Stauning et al.*, 2008]. If this index responds to $E_{\text{K-R}}$, then it still exhibits annual variation, since $E_{\text{K-R}}$ is generally smaller due to an enhanced Pedersen conductance. In fact, *Lukianova et al.* [2002] found that predominance of large PC index (PC > 12) is seen in winter hemisphere for extremely high levels of magnetic activity. In a future study, one can simply examine the general annual variation of the PCN index to see whether this index is likely to be smaller in summer than in winter.

Bibliography

Akaike, H. (1973), Information theory and an extension of the maximum likelihood principle, paper presented at International Symposium on Information Theory, 2 nd, Tsahkadsor, Armenian SSR.

Akaike, H. (1974), A new look at the statistical model identification, *IEEE Trans. Autom. Control*, *19*(6), 716-723, doi:10.1109/tac.1974.1100705.

Akasofu, S.-I. (1979a), What is a magnetospheric substorm?, in *Dynamics of Magnetosphere*, edited by S.-I. Akasofu, pp. 447-460, D. Reidel, Dordrecht.

Akasofu, S.-I. (1979b), Interplanetary energy flux associated with magnetospheric substorms, *Planet. Space Sci.*, *27*(4), 425-431, doi:10.1016/0032-0633(79)90119-3.

Akasofu, S.-I., S. Chapman, and C.-I. Meng (1965), The polar electrojet, *J. Atmos. Terr. Phys.*, *27*(11–12), 1275-1305, doi:10.1016/0021-9169(65)90087-5.

Ashour-Abdalla, M., R. J. Walker, V. Peroomian, and M. El-Alaoui (2008), On the importance of accurate solar wind measurements for studying magnetospheric dynamics, *J. Geophys. Res.*, *113*(A8), A08204, doi:10.1029/2007ja012785.

Axford, W. I. (1964), Viscous interaction between the solar wind and the earth's magnetosphere, *Planet. Space Sci.*, *12*(1), 45-53, doi:10.1016/0032-0633(64)90067-4.

Bargatze, L. F., D. N. Baker, R. L. McPherron, and E. W. Hones, Jr. (1985), Magnetospheric impulse response for many levels of geomagnetic activity, *J. Geophys. Res.*, *90*(A7), 6387-6394, doi:10.1029/JA090iA07p06387.

Bohlin, J. D. (1977), Extreme-ultraviolet observations of coronal holes, *Sol. Phys.*, *51*(2), 377-398, doi:10.1007/bf00216373.

Borovsky, J. E., B. Lavraud, and M. M. Kuznetsova (2009), Polar cap potential saturation, dayside reconnection, and changes to the magnetosphere, *J. Geophys. Res.*, *114*(A3), A03224, doi:10.1029/2009ja014058.

Boyle, C. B., P. H. Reiff, and M. R. Hairston (1997), Empirical polar cap potentials, *J. Geophys. Res.*, *102*(A1), 111-125, doi:10.1029/96ja01742.

Burnham, K., and D. Anderson (2002), *Model Selection and Multimodel Inference: A Practical Information-Theoretic Approach*, Springer.

Burton, R. K., R. L. McPherron, and C. T. Russell (1975), An empirical relationship between interplanetary conditions and Dst, *J. Geophys. Res.*, *80*(31), 4204-4214, doi:10.1029/JA080i031p04204.

Chapman, S., and V. C. A. Ferraro (1931), A new theory of magentic storms, *Terr. Magn. Atmos. Electr.*, *36*(3), 171-186, doi:10.1029/TE036i003p00171.

Chun, F. K., D. J. Knipp, M. G. McHarg, J. R. Lacey, G. Lu, and B. A. Emery (2002), Joule heating patterns as a function of polar cap index, *J. Geophys. Res.*, *107*(A7), 1119, doi:10.1029/2001ja000246.

Chun, F. K., D. J. Knipp, M. G. McHarg, G. Lu, B. A. Emery, S. Vennerstrøm, and O. A. Troshichev (1999), Polar cap index as a proxy for hemispheric Joule heating, *Geophys. Res. Lett.*, *26*(8), 1101-1104, doi:10.1029/1999gl900196.

Clauer, C. R., and Y. Kamide (1985), DP 1 and DP 2 current systems for the March 22, 1979 substorms, *J. Geophys. Res.*, *90*(A2), 1343-1354, doi:10.1029/JA090iA02p01343.

Clauer, C. R., R. L. McPherron, C. Searls, and M. G. Kivelson (1981), Solar wind control of auroral zone geomagnetic activity, *Geophys. Res. Lett.*, *8*(8), 915-918, doi:10.1029/GL008i008p00915.

Cleveland, W. S. (1979), Robust locally weighted regression and smoothing scatterplots, *JASA*, *74*(368), 829-836, doi:10.2307/2286407.

Cortie, A. L. (1912), Sunspots and terrestrial magnetic phenomena, 1898-1911: The cause of the annual variation in magnetic disturbance, *Mon. Not. R. Astron. Soc.*, *73*, 52-60,

Daughton, W., V. Roytershteyn, H. Karimabadi, L. Yin, B. J. Albright, B. Bergen, and K. J. Bowers (2011), Role of electron physics in the development of turbulent magnetic reconnection in collisionless plasmas, *Nat. Phys.*, *7*(7), 539-542, doi:10.1038/nphys1965.

Davis, T. N., and M. Sugiura (1966), Auroral electrojet activity index AE and its universal time variations, *J. Geophys. Res.*, *71*(3), 785-801, doi:10.1029/JZ071i003p00785.

Dungey, J. W. (1961), Interplanetary magnetic field and the auroral zones, *Phys. Rev. Lett.*, *6*(2), 47-48, doi:10.1103/PhysRevLett.6.47.

Dungey, J. W. (1963), The structure of the exosphere or adventures in velocity space, in *Geophysics, The Earth's Environment*, edited by D. J. Hieblot and A. Lebeau, p. 503, Gordon & Breach, New York.

Emery, B. A., I. G. Richardson, D. S. Evans, and F. J. Rich (2009), Solar wind structure sources and periodicities of auroral electron power over three solar cycles, *J. Atmos. Solar-Terr. Phys.*, *71*(10-11), 1157-1175, doi: 10.1016/j.jastp.2008.08.005.

Emery, B. A., V. Coumans, D. S. Evans, G. A. Germany, M. S. Greer, E. Holeman, K. Kadinsky-Cade, F. J. Rich, and W. Xu (2008), Seasonal, Kp, solar wind, and solar flux variations in long-term single-pass satellite estimates of electron and ion auroral hemispheric power, *J. Geophys. Res.*, *113*(A6), A06311, doi: 10.1029/2007ja012866.

Emslie, A. G., et al. (2004), Energy partition in two solar flare/CME events, *J. Geophys. Res.*, *109*(A10), A10104, doi:10.1029/2004ja010571.

Fiori, R. A. D., A. V. Koustov, D. Boteler, and R. A. Makarevich (2009), PCN magnetic index and average convection velocity in the polar cap inferred from SuperDARN radar measurements, *J. Geophys. Res.*, *114*(A7), A07225, doi:10.1029/2008ja013964.

Gao, Y. (2012a), Comparing the cross polar cap potentials measured by SuperDARN and AMIE during saturation intervals, *J. Geophys. Res.*, *117*(A8), A08325, doi:10.1029/2012ja017690.

Gao, Y. (2012b), On anomalous departures from a linear relation between the polar cap index and its controlling factors in solar wind and magnetotail, *J. Geophys. Res.*, *117*(A6), A06201, doi:10.1029/2012ja017721.

Gao, Y., M. G. Kivelson, and R. J. Walker (2012a), The linear dependence of polar cap index on its controlling factors in solar wind and magnetotail, *J. Geophys. Res.*, *117*(A5), A05213, doi:10.1029/2011ja017229.

Gao, Y., M. G. Kivelson, R. J. Walker, and J. M. Weygand (2012b), Long-term variation of driven and unloading effects on polar cap dynamics, *J. Geophys. Res.*, *117*(A2), A02203, doi:10.1029/2011ja017149.

Gao, Y., M. G. Kivelson, A. J. Ridley, J. M. Weygand, and R. J. Walker (2012c), Utilizing the polar cap index to explore strong driving of polar cap dynamics, *J. Geophys. Res.*, *117*(A7), A07213, doi:10.1029/2011ja017087.

Gosling, J. T., R. M. Skoug, D. J. McComas, and C. W. Smith (2005), Direct evidence for magnetic reconnection in the solar wind near 1 AU, *J. Geophys. Res.*, *110*(A1), A01107, doi:10.1029/2004ja010809.

Hairston, M. R., R. A. Heelis, and F. J. Rich (1998), Analysis of the ionospheric cross polar cap potential drop using DMSP data during the National Space Weather Program study period, *J. Geophys. Res.*, *103*(A11), 26337-26347, doi:10.1029/97ja03241.

Hairston, M. R., T. W. Hill, and R. A. Heelis (2003), Observed saturation of the ionospheric polar cap potential during the 31 March 2001 storm, *Geophys. Res. Lett.*, *30*(6), 1325, doi:10.1029/2002gl015894.

Hastie, T. J., and R. J. Tibshirani (1986), Generalized additive models, *Stat. Sci.*, *1*(3), 297-310, doi: 10.1214/ss/1177013604.

Hastie, T. J., and R. J. Tibshirani (1990), *Generalized Additive Models*, Chapman and Hall/CRC.

Hill, T. W., A. J. Dessler, and R. A. Wolf (1976), Mercury and Mars: The role of ionospheric conductivity in the acceleration of magnetospheric particles, *Geophys. Res. Lett.*, *3*(8), 429-432, doi:10.1029/GL003i008p00429.

Horton, W., J. P. Smith, R. Weigel, C. Crabtree, I. Doxas, B. Goode, and J. Cary (1999), The solar-wind driven magnetosphere-ionosphere as a complex dynamical system, *Phys. Plasmas*, *6*(11), 4178-4184, doi:10.1063/1.873683.

Huang, C.-S. (2005), Variations of polar cap index in response to solar wind changes and magnetospheric substorms, *J. Geophys. Res.*, *110*(A1), A01203, doi:10.1029/2004ja010616.

Hughes, W. J. (1995), The magnetopause, magnetotail, and magnetic reconnection, in *Introduction to Space Physics*, edited by M. G. Kivelson and C. T. Russell, pp. 227-287, Cambridge Univ. Press, New York.

Hundhausen, A. J. (1995), The solar wind, in *Introduction to Space Physics*, edited by M. G. Kivelson and C. T. Russell, pp. 91-128, Cambridge Univ. Press, New York.

Iijima, T., and T. Nagata (1972), Signatures for substorm development of the growth phase and expansion phase, *Planet. Space Sci.*, *20*(7), 1095-1112, doi:10.1016/0032-0633(72)90219-X.

Janzhura, A. S., and O. A. Troshichev (2008), Determination of the running quiet daily geomagnetic variation, *J. Atmos. Sol-Terr. Phy.*, *70*(7), 962-972, doi:10.1016/j.jastp.2007.11.004.

Kan, J. R., and L. C. Lee (1979), Energy coupling function and solar wind-magnetosphere dynamo, *Geophys. Res. Lett., 6*(7), 577-580, doi:10.1029/GL006i007p00577.

King, J. H., and N. E. Papitashvili (2005), Solar wind spatial scales in and comparisons of hourly Wind and ACE plasma and magnetic field data, *J. Geophys. Res.*, *110*(A2), A02104, doi:10.1029/2004ja010649.

Kitamura, N., Y. Ogawa, Y. Nishimura, N. Terada, T. Ono, A. Shinbori, A. Kumamoto, V. Truhlik, and J. Smilauer (2011), Solar zenith angle dependence of plasma density and temperature in the polar cap ionosphere and low-altitude magnetosphere during geomagnetically quiet periods at solar maximum, *J. Geophys. Res.*, *116*(A8), A08227, doi:10.1029/2011ja016631.

Kivelson, M. G. (1995), Physics of space plasmas, in *Introduction to Space Physics*, edited by M. G. Kivelson and C. T. Russell, pp. 27-57, Cambridge Univ. Press, New York.

Kivelson, M. G., and A. J. Ridley (2008), Saturation of the polar cap potential: Inference from Alfvén wing arguments, *J. Geophys. Res.*, *113*(A5), A05214, doi:10.1029/2007ja012302.

Kokubun, S. (1972), Relationship of interplanetary magnetic field structure with development of substorm and storm main phase, *Planet. Space Sci.*, *20*(7), 1033-1049, doi:10.1016/0032-0633(72)90214-0.

Lavraud, B., and J. E. Borovsky (2008), Altered solar wind-magnetosphere interaction at low Mach numbers: Coronal mass ejections, *J. Geophys. Res.*, *113*(A9), A00B08, doi:10.1029/2008ja013192.

Liou, K., J. F. Carbary, P. T. Newell, C. I. Meng, and O. Rasmussen (2003), Correlation of auroral power with the polar cap index, *J. Geophys. Res.*, *108*(A3), 1108, doi:10.1029/2002ja009556.

Lukianova, R., O. Troshichev, and G. Lu (2002), The polar cap magnetic activity indices in the southern (PCS) and northern (PCN) polar caps: Consistency and discrepancy, *Geophys. Res. Lett.*, 29(18), 1879, doi:10.1029/2002GL015179.

Lukianova, R. (2003), Magnetospheric response to sudden changes in solar wind dynamic pressure inferred from polar cap index, *J. Geophys. Res.*, *108*(A12), 1428, doi:10.1029/2002ja009790.

Matsuo, T., A. D. Richmond, and G. Lu (2005), Optimal interpolation analysis of high-latitude ionospheric electrodynamics using empirical orthogonal functions: Estimation of dominant modes of variability and temporal scales of large-scale electric fields, *J. Geophys. Res.*, *110*(A6), A06301, doi:10.1029/2004ja010531.

Mazur, J. E., G. M. Mason, J. R. Dwyer, J. Giacalone, J. R. Jokipii, and E. C. Stone (2000), Interplanetary magnetic field line mixing deduced from impulsive solar flare particles, *Astrophys. J.*, *532*(1), L79, doi:10.1086/312561.

McComas, D. J., S. J. Bame, P. Barker, W. C. Feldman, J. L. Phillips, P. Riley, and J. W. Griffee (1998), Solar Wind Electron Proton Alpha Monitor (SWEPAM) for the Advanced Composition Explorer, *Space Sci. Rev.*, *86*(1), 563-612, doi:10.1023/a:1005040232597.

McIntosh, D. H. (1959), On the annual variation of magnetic disturbance, *Phil. Trans. R. Soc. A*, *251*(1001), 525-552, doi:10.1098/rsta.1959.0010.

McPherron, R. L. (1995), Magnetospheric dynamics, in *Introduction to Space Physics*, edited by M. G. Kivelson and C. T. Russell, pp. 401-458, Cambridge Univ. Press, New York.

McPherron, R. L., and D. N. Baker (1993), Factors influencing the intensity of magnetospheric substorms, *J. Atmos. Terr. Phys.*, *55*(8), 1091-1122, doi:10.1016/0021-9169(93)90040-6.

McPherron, R. L., D. N. Baker, L. F. Bargatze, C. R. Clauer, and R. E. Holzer (1988), IMF control of geomagnetic activity, *Adv. Space Res.*, *8*(9–10), 71-86, doi:10.1016/0273-1177(88)90114-7.

Mende, S. B., et al. (2000), Far ultraviolet imaging from the IMAGE spacecraft. 2. Wideband FUV imaging, *Space Sci. Rev.*, *91*(1), 271-285, doi:10.1023/a:1005227915363.

Merkine, V. G., K. Papadopoulos, G. Milikh, A. S. Sharma, X. Shao, J. Lyon, and C. Goodrich (2003), Effects of the solar wind electric field and ionospheric conductance on the cross polar cap potential: Results of global MHD modeling, *Geophys. Res. Lett.*, *30*(23), 2180, doi:10.1029/2003gl017903.

Myers, R. H. (2000), *Classical and Modern Regression with Applications*, 2nd ed., Duxbury Press.

Nagatsuma, T. (2002a), Saturation of polar cap potential by intense solar wind electric fields, *Geophys. Res. Lett.*, *29*(10), 1422, doi:10.1029/2001gl014202.

Nagatsuma, T. (2002b), Characteristics of negative values of polar cap index as an indicator of reversed convection, *Adv. Polar Upper Atmos. Res.*, *16*, 36.

Newell, P. T., T. Sotirelis, K. Liou, C. I. Meng, and F. J. Rich (2007), A nearly universal solar wind-magnetosphere coupling function inferred from 10 magnetospheric state variables, *J. Geophys. Res.*, *112*(A1), A01206, doi:10.1029/2006ja012015.

Ober, D. M., N. C. Maynard, and W. J. Burke (2003), Testing the Hill model of transpolar potential saturation, *J. Geophys. Res.*, *108*(A12), 1467, doi:10.1029/2003ja010154.

Østgaard, N., R. R. Vondrak, J. W. Gjerloev, and G. Germany (2002), A relation between the energy deposition by electron precipitation and geomagnetic indices during substorms, *J. Geophys. Res.*, *107*(A9), 1246, doi: 10.1029/2001JA002003.

Parker, E. N. (1957), Sweet's mechanism for merging magnetic fields in conducting fluids, *J. Geophys. Res.*, *62*(4), 509-520, doi:10.1029/JZ062i004p00509.

Perreault, P., and S. I. Akasofu (1978), A study of geomagnetic storms, *Geophys. J. Int.*, *54*(3), 547-573, doi:10.1111/j.1365-246X.1978.tb05494.x.

Petschek, H. E. (1964), Magnetic field annihilation, paper presented at The Physics of Solar Flares, Proceedings of the AAS-NASA Symposium, Greenbelt, MD.

Pudovkin, M. I., M. F. Heyn, and V. V. Lebedeva (1982), Magnetosheath's parameters and their dependence on intensity and direction of the solar wind magnetic field, *J. Geophys. Res.*, *87*(A10), 8131-8138, doi:10.1029/JA087iA10p08131.

Raeder, J., Y. L. Wang, T. J. Fuller -Rowell, and H. J. Singer (2001), Global simulation of magnetospheric space weather effects of the Bastille day storm, *Sol. Phys.*, *204*(1-2), 323-337, doi:10.1023/A:1014228230714.

Reiff, P. H., and J. G. Luhmann (1986), Solar wind control of the polar-cap voltage, in *Solar Wind-Magnetosphere Coupling*, edited, pp. 453-476.

Richmond, A. D., and Y. Kamide (1988), Mapping Electrodynamic Features of the High-Latitude Ionosphere from Localized Observations: Technique, *J. Geophys. Res.*, *93*(A6), 5741-5759, doi:10.1029/JA093iA06p05741.

Richmond, A. D., et al. (1988), Mapping Electrodynamic Features of the High-Latitude Ionosphere from Localized Observations: Combined Incoherent-Scatter Radar and Magnetometer Measurements for January 18-19, 1984, *J. Geophys. Res.*, *93*(A6), 5760-5776, doi:10.1029/JA093iA06p05760.

Ridley, A. J. (2000), Estimations of the uncertainty in timing the relationship between magnetospheric and solar wind processes, *J. Atmos. Sol-Terr. Phy.*, *62*(9), 757-771, doi:10.1016/S1364-6826(00)00057-2.

Ridley, A. J. (2007), Effects of seasonal changes in the ionospheric conductances on magnetospheric field-aligned currents, *Geophys. Res. Lett.*, *34*(5), L05101, doi:10.1029/2006gl028444.

Ridley, A. J., and E. A. Kihn (2004b), Polar cap index comparisons with AMIE cross polar cap potential, electric field, and polar cap area, *Geophys. Res. Lett.*, *31*(7), L07801, doi:10.1029/2003gl019113.

Robinson, R. M., and R. R. Vondrak (1984b), Measurements of E Region Ionization and Conductivity Produced By Solar Illumination at High Latitudes, *J. Geophys. Res.*, *89*(A6), 3951-3956, doi:10.1029/JA089iA06p03951.

Ruohoniemi, J. M., and K. B. Baker (1998), Large-scale imaging of high-latitude convection with Super Dual Auroral Radar Network HF radar observations, *J. Geophys. Res.*, *103*(A9), 20797-20811, doi:10.1029/98ja01288.

Russell, C. T. (1995), A brief history of solar-terrestrial physics, in *Introduction to Space Physics*, edited by M. G. Kivelson and C. T. Russell, pp. 1-26, Cambridge Univ. Press, New York.

Russell, C. T., and R. L. McPherron (1973), Semiannual variation of geomagnetic activity, *J. Geophys. Res.*, *78*(92), Russell, C. T., G. Lu, and J. G. Luhmann (2000), Lessons from the ring current injection during the September 24, 25, 1998 storm, *Geophys. Res. Lett.*, *27*(9), 1371-1374, doi:10.1029/1999gl003718.

Scurry, L., and C. T. Russell (1991), Proxy studies of energy transfer to the magnetosphere, *J. Geophys. Res.*, *96*(A6), 9541-9548, doi:10.1029/91ja00569.

Shepherd, S. G., R. A. Greenwald, and J. M. Ruohoniemi (2002), Cross polar cap potentials measured with Super Dual Auroral Radar Network during quasi-steady solar wind and interplanetary magnetic field conditions, *J. Geophys. Res.*, *107*(A7), 1094, doi:10.1029/2001ja000152.

Shumway, R. H., and D. S. Stoffer (2006), *Time Series Analysis and Its Applications: With R Examples*, Springer.

Siscoe, G. L. (2011), Aspects of global coherence of magnetospheric behavior, *J. Atmos. Sol-Terr. Phy.*, *73*(4), 402-419, doi:10.1016/j.jastp.2010.11.005.

Siscoe, G. L., J. Raeder, and A. J. Ridley (2004), Transpolar potential saturation models compared, *J. Geophys. Res.*, *109*(A9), A09203, doi:10.1029/2003ja010318.

Siscoe, G. L., G. M. Erickson, B. U. Ö. Sonnerup, N. C. Maynard, J. A. Schoendorf, K. D. Siebert, D. R. Weimer, W. W. White, and G. R. Wilson (2002), Hill model of transpolar potential saturation: Comparisons with MHD simulations, *J. Geophys. Res.*, *107*(A6), 1075, doi:10.1029/2001ja000109.

Smith, C. W., J. L'Heureux, N. F. Ness, M. H. Acuña, L. F. Burlaga, and J. Scheifele (1998), The ACE Magnetic Fields Experiment, *Space Sci. Rev.*, *86*(1), 613-632, doi:10.1023/a:1005092216668.

Spiro, R. W., P. H. Reiff, and L. J. Maher, Jr. (1982), Precipitating electron energy flux and auroral zone conductances - An empirical model, *J. Geophys. Res.*, *87*(A10), 8215-8227, doi: 10.1029/JA087iA10p08215.

Stauning, P. (2011), Comment on "The PC index: review of methods", by McCreadie and Menvielle (2010), *Ann. Geophys.*, *29*(6), 1137-1146, doi:10.5194/angeo-29-1137-2011.

Stauning, P., and O. A. Troshichev (2008), Polar cap convection and PC index during sudden changes in solar wind dynamic pressure, *J. Geophys. Res.*, *113*(A8), A08227, doi:10.1029/2007ja012783.

Stauning, P., O. A. Troshichev, and A. Janzhura (2008), The Polar Cap (PC) indices: Relations to solar wind parameters and global magnetic activity, *J. Atmos. Sol-Terr. Phy.*, *70*(18), 2246-2261, doi:10.1016/j.jastp.2008.09.028.

Stone, C. J. (1985), Additive regression and other nonparametric models, *Ann. Stat.*, *13*(2), 689-705, doi:10.1214/aos/1176349548.

Stone, E. C., A. M. Frandsen, R. A. Mewaldt, E. R. Christian, D. Margolies, J. F. Ormes, and F. Snow (1998), The Advanced Composition Explorer, *Space Sci. Rev.*, *86*(1), 1-22, doi:10.1023/a:1005082526237.

Svalgaard, L. (1977), Geomagnetic activity: dependence on solar wind parameters, in *Coronal Holes and High Speed Wind Streams*, edited by J. B. Zirker, p. 371, Colorado Assoc. Univ. Press, Boulder, CO.

Sweet, P. A. (1958), The neutral point theory of solar flares, in *International Astronomical Union Symposium no. 6*, edited by B. Lehnert, pp. 123-134, Cambridge Univ. Press,

Takalo, J., and J. Timonen (1998), Comparison of the dynamics of the AU and PC indices, *Geophys. Res. Lett.*, *25*, 2101-2104,

Temerin, M., and X. Li (2006), Dst model for 1995–2002, *J. Geophys. Res.*, *111*(A4), A04221, doi:10.1029/2005ja011257.

Troshichev, O. A., and V. G. Andrezen (1985), The relationship between interplanetary quantities and magnetic activity in the southern polar cap, *Planet. Space Sci.*, *33*(4), 415-419, doi:10.1016/0032-0633(85)90086-8.

Troshichev, O. A., A. Janzhura, and P. Stauning (2006), Unified PCN and PCS indices: Method of calculation, physical sense, and dependence on the IMF azimuthal and northward components, *J. Geophys. Res.*, *111*(A5), A05208, doi:10.1029/2005ja011402.

Troshichev, O. A., A. S. Janzhura, and P. Stauning (2007), Magnetic activity in the polar caps: Relation to sudden changes in the solar wind dynamic pressure, *J. Geophys. Res.*, *112*(A11), A11202, doi:10.1029/2007ja012369.

Troshichev, O. A., V. G. Andrezen, S. Vennerstrøm, and E. Friis-Christensen (1988), Magnetic activity in the polar cap - A new index, *Planet. Space Sci.*, *36*(11), 1095-1102, doi:10.1016/0032-0633(88)90063-3.

Troshichev, O. A., H. Hayakawa, A. Matsuoka, T. Mukai, and K. Tsuruda (1996), Cross polar cap diameter and voltage as a function of PC index and interplanetary quantities, *J. Geophys. Res.*, *101*(A6), 13429-13435, doi:10.1029/95ja03672.

Troshichev, O. A., R. Y. Lukianova, V. O. Papitashvili, F. J. Rich, and O. Rasmussen (2000), Polar cap index (PC) as a proxy for ionospheric electric field in the near-pole region, *Geophys. Res. Lett.*, *27*(23), 3809-3812, doi:10.1029/2000gl003756.

Vasyliunas, V. M. (1975), Theoretical models of magnetic field line merging, *Rev. Geophys.*, *13*(1), 303-336, doi:10.1029/RG013i001p00303.

Vasyliunas, V. M., J. R. Kan, G. L. Siscoe, and S. I. Akasofu (1982), Scaling relations governing magnetospheric energy transfer, *Planet. Space Sci.*, *30*(4), 359-365, doi:10.1016/0032-0633(82)90041-1.

Vennerstrøm, S., E. Friis-Christensen, O. A. Troshichev, and V. G. Andersen (1991), Comparison between the Polar Cap Index, PC, and the Auroral Electrojet Indices AE, AL, and AU, *J. Geophys. Res.*, *96*(A1), 101-113, doi:10.1029/90ja01975.

Walker, G. (1931), On periodicity in series of related terms, *Proceedings of the Royal Society of London. Series A, Containing Papers of a Mathematical and Physical Character*, *131*(818), 518-532, doi:10.1175/1520-0493(1931)59<277:OPISOR>2.0.CO;2.

Walker, R. J., and C. T. Russell (1995), Solar-wind interactions with magnetized planets, in *Introduction to Space Physics*, edited by C. T. Russell and M. G. Kivelson, pp. 164-182, Cambridge Univ. Press, New York.

Weimer, D. R. (1996), A flexible, IMF dependent model of high-latitude electric potentials having "Space Weather" applications, *Geophys. Res. Lett.*, *23*(18), 2549-2552, doi:10.1029/96gl02255.

Weimer, D. R. (2001), An improved model of ionospheric electric potentials including substorm perturbations and application to the Geospace Environment Modeling November 24, 1996, event, *J. Geophys. Res.*, *106*(A1), 407-416, doi:10.1029/2000ja000604.

Weimer, D. R. (2004), Correction to "Predicting interplanetary magnetic field (IMF) propagation delay times using the minimum variance technique", *J. Geophys. Res.*, *109*(A12), A12104, doi:10.1029/2004ja010691.

Weimer, D. R. (2005), Improved ionospheric electrodynamic models and application to calculating Joule heating rates, *J. Geophys. Res.*, *110*(A5), A05306, doi:10.1029/2004ja010884.

Weimer, D. R., D. M. Ober, N. C. Maynard, M. R. Collier, D. J. McComas, N. F. Ness, C. W. Smith, and J. Watermann (2003), Predicting interplanetary magnetic field (IMF) propagation delay times using the minimum variance technique, *J. Geophys. Res.*, *108*(A1), 1026, doi:10.1029/2002ja009405.

Wygant, J. R., R. B. Torbert, and F. S. Mozer (1983), Comparison of S3-3 Polar Cap Potential Drops with the Interplanetary Magnetic Field and Models of Magnetopause Reconnection, *J. Geophys. Res.*, *88*(A7), 5727-5735, doi:10.1029/JA088iA07p05727.

Yule, G. U. (1927), On a method of investigating periodicities in disturbed series, with special reference to Wolfer's sunspot numbers, *Philosophical Transactions of the Royal Society of London. Series A, Containing Papers of a Mathematical or Physical Character*, *226*, 267-298, doi:10.1098/rsta.1927.0007.